# NUMERICAL, ANALYTICAL AND EXPERIMENTAL ANALYSIS OF INDENTATION

A THESIS SUBMITTED TO
THE GRADUATE SCHOOL OF NATURAL AND APPLIED SCIENCES
OF
MIDDLE EAST TECHNICAL UNIVERSITY

BY

NAGİHAN TOPCU

IN PARTIAL FULLFILLMENT OF THE REQUIREMENTS
FOR
THE DEGREE OF MASTER OF SCIENCE
IN
MECHANICAL ENGINEERING

MARCH 2005

Approval of the Graduate School of Natural and Applied Sciences

____________________________

Prof. Dr. Canan Özgen
Director

I certify that this thesis satisfies all the requirements as a thesis for the degree of Master of Science.

____________________________

Prof. Dr. Kemal İder
Head of Department

This is to certify that we have read this thesis and that in our opinion it is fully adequate, in scope and quality, as a thesis for the degree of Master of Science.

____________________________

Prof. Dr. A. Erman Tekkaya
Supervisor

Examining Committee Members

Prof. Dr. Mehmet Çalışkan (METU, ME)____________________________

Prof. Dr. A. Erman Tekkaya (METU, ME)____________________________

Prof. Dr. Yalçın Mengi (METU, ES)____________________________

Asst. Prof. Dr. Merve Erdal (METU, ME)____________________________

Asst. Prof. Dr. Ergin Tönük (METU, ME)____________________________

**I hereby declare that all information in this document has been obtained and presented in accordance with academic rules and ethical conduct. I also declare that, as required by these rules and conduct, I have fully cited and referenced all material and results that are not original to this work.**

**Name, Last name :** Nagihan Topcu

**Signature :**

# ABSTRACT


### NUMERICAL, ANALYTICAL AND EXPERIMENTAL ANALYSIS OF INDENTATION



Topcu, Nagihan
M.S., Department of Mechanical Engineering
Supervisor: Prof. Dr. A. Erman Tekkaya



February 2005, 163 Pages



Indentation is a practical and easy method, therefore, is a preferred method of material characterization. Main aim of this thesis study is to determine anisotropic properties of metals by indentation tests. The basic property of the indenter used in the finite element analyses and experiments is that it is specific to this process. Thesis includes studies on optimization of the indenter geometry, analyses of effects of friction coefficient, multiple indentations, tilting of the indenter and clamping of the specimen on force-displacements curves during indentation by finite element analyses.

This study also includes finite element analyses of compression tests where these experiments have been necessary to prove anisotropic behavior of the specimen material. In addition to compression, tension tests are done to have a reference for indentation tests. On the other hand, the upper bound method which is an analytical solution is applied on the assumption of plane strain indentation.



Keywords: Indentation, Finite Element Method, Upper Bound Method, Indentation Tests

# ÖZ

## ÇUKURİZ BASMA YÖNTEMİNİN NUMERİK, ANALİTİK VE DENEYSEL OLARAK İNCELENMESİ

Topcu, Nagihan
Yüksek Lisans, Makine Mühendisliği Bölümü
Tez Yöneticisi: Prof. Dr. A. Erman Tekkaya
Şubat 2005, 163 Sayfa

Çukuriz basma pratik ve kolay bir yöntem olduğu için malzeme karakterizasyonunda tercih edilen bir metoddur. Bu tez çalışmasının tememl amacı metallerin anizotropik özelliklerinin çukuriz basma testleriyle belirlenmesidir. Sonlu eleman analizlerinde ve çukuriz basma testlerinde kullanılan zımbanın temel özelliği bu işleme özgün olmasıdır. Tez, zımba geometrisinin optimizasyonu, sonlu eleman analiziyle sürtünme katsayısının, çoklu çukuriz basmanın, zımbanın eğilmesinin ve numunenin sıkıştırılmasının çukuriz basmada kuvvet-ilerleme eğrilerine etkisi üzerine çalışmalar içermektedir.

Bu çalışma aynı zamanda malzemenin anizotropik özelliğinin gösterilmesinde gerekli olduğu görülen basma testlerinin sonlu eleman analizlerini içermektedir. Sıkıştırma testlerine ek olarak çekme testleri de çukuriz basma testlerine referans elde etmek amacıyla yapılmıştır. Bir yandan analitik bir çözüm yöntemi olan üst sınır yöntemi düzlemsel genlemeli çukuriz basma varsayımına dayanarak uygulanmıştır.

Anahtar Kelimeler: Çukuriz Basma, Sonlu Eleman Yöntemi, Üst Sınır Yöntemi, Çukuriz Basma Testleri

*To the Memory of My Father*

# ACKNOWLEDGEMENTS

I would like to express my deepest gratitude and appreciation to my supervisor, Prof. Dr. A. Erman Tekkaya who inspired, encouraged and supported me at all levels of this study. I would also like to thank my partner Erge Koray for supporting my work with his and for his cooperation throughout this work.

The support of The Scientific and Technical Research Council of Turkey (TÜBİTAK) and Deutsche Forschungsgemeinshaft (DFG) under contract MISAG-DFG1 is also greatly acknowledged. The partners, colleagues and professors who have shared their experiences, who have taken part in design and production of the set-up, are greatly acknowledged. Thanks to Dipl.-Ing. Michele D'Ottavio, Dr.-Ing. Klaus Eberle, Ing. Gian Francesco Ferraris and Prof. Dr.-Ing. Klaus Pöhlandt from Stuttgart University, Stuttgart, Germany and thanks to Prof. Dr.-Ing. Reiner Kreiβig and Dipl.-Ing. Mario Lindner from Chemnitz University of Technology, Chemnitz, Germany.

I would like to express my appreciations to Prof. Dr. Hoogenboom for his lectures and his ideas for upper bound method solution of indentation. Thanks to Prof. Dr. Ramaekers for his lectures on sheet metal forming processes and what he has added to my knowledge of metal forming.

I would like to thank the technicians of METU Mechanical Engineering Department, especially to Necati Güner, Yusuf Papur, Saim Seloğlu and Mustafa Yalçın for their help in manufacturing of test specimens and applications of tests.

I also wish to acknowledge previous and current Femlab members Mert Aygen, O. Koray Demir, Mete Egemen, Volkan Güley, Alper Güner, Özgür Koçak, Bahadır Koçaker, Ömer Music, Oya Okman, Muhsin Öcal, İ. Erkan Önder and

Muin S. Öztop. I am grateful to my colleague Yavuz S. Kayserilioğlu for his friendship and help at all times. I send my appreciations to Onur Gündoğdu no matter if he is there all the time or not. Thanks to my friend Hande Sönmez who is more than a sister to me.

Special thanks to Canderim Önder for being part of the best memories of my university years. I wish the best for us for the future.

My greatest appreciations go to my parents for their support and encouragement. Thanks father for being a sample to me as a hard-working, idealist, honorable and honest person. Thanks mum for thinking of me before yourself.

# TABLE OF CONTENTS

# CHAPTER 1

# INTRODUCTION

Material characterization is the most important aspect when manufacturing including metal forming, machining, surface treatments and heat treatments, mechanical design or fracture mechanics is considered. These are only some of the topics where properties of materials are strongly needed. For determination of life of a part, selection of material to match service requirements, design of a part under known loading conditions, analysis of strength of a part or for determination of manufacturing steps of a part material properties such as the flow curve, anisotropy, toughness, ductility, hardness, forming limit, etc. are needed.

These properties are determined by standart tests. For example, the most common methods for determination of flow curves are tensile tests, upsetting tests and torsion tests. To determine formability of sheet metal methods such as deep drawing methods, stretch-bend tests, limit dome height tests are applied.

Among these test methods indentation is the basic concern of this thesis. The study also deals with anisotropy of the materials.

In this chapter, the indentation process and anisotropy will be introduced. Then, need for this study and the aim will be explained and the scope of this thesis will be given. The collaborative work with German universities will be introduced where this thesis study constitutes a part of that collaborative work.

## 1.1 Indentation

Indentation is most commonly known as a method to determine hardness which is resistance to deformation. Many properties are predicted from hardness values when combined with additional information such as alloy composition. A list of such properties can be given as: resistance to abrasives or wear, modulus of elasticity, yield strength, ductility, fracture toughness, etc. Some properties such as yield strength have numerical relationships with hardness values, whereas others such as fracture toughness are deduced by observations of cracks surrounding the indentations. Also other relationships have been empirically developed by time like a link between machinability and hardness values [1].

The most commonly used indentation tests are seen in Figure 1.1.

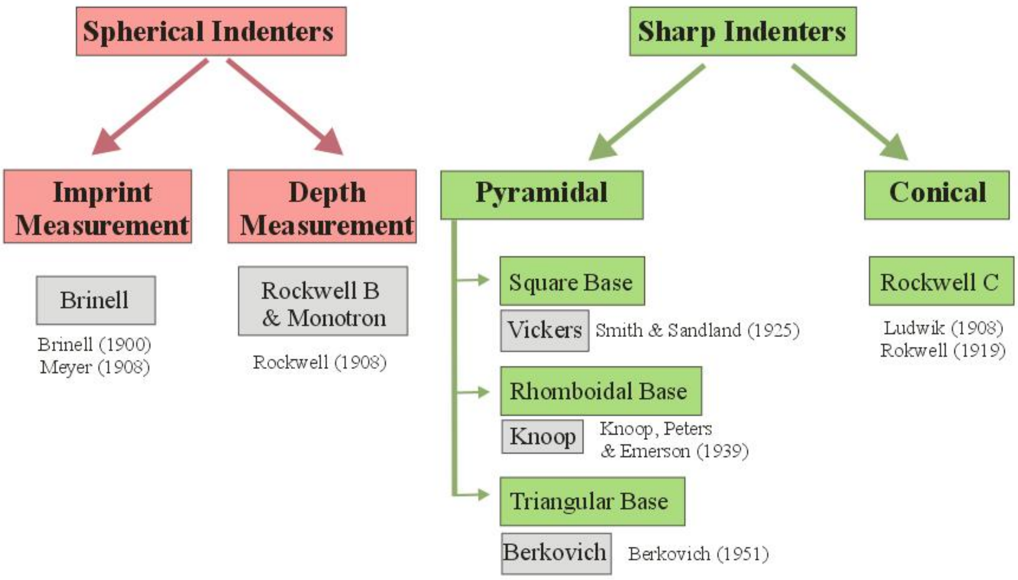


**Figure 1.1** Most common indentation methods

In doing hardness tests, standard indenter geometries are used and generally the hardness number is obtained by a relation between the applied load and a measure of the imprint which is generally the diameter or the mean diameter depending on the indenter shape. The most common indenter shapes are seen in Figure 1.2.

The reasons why indentation test is preferred in many areas are its simplicity, rapidity in application and small size of sample needed for testing.

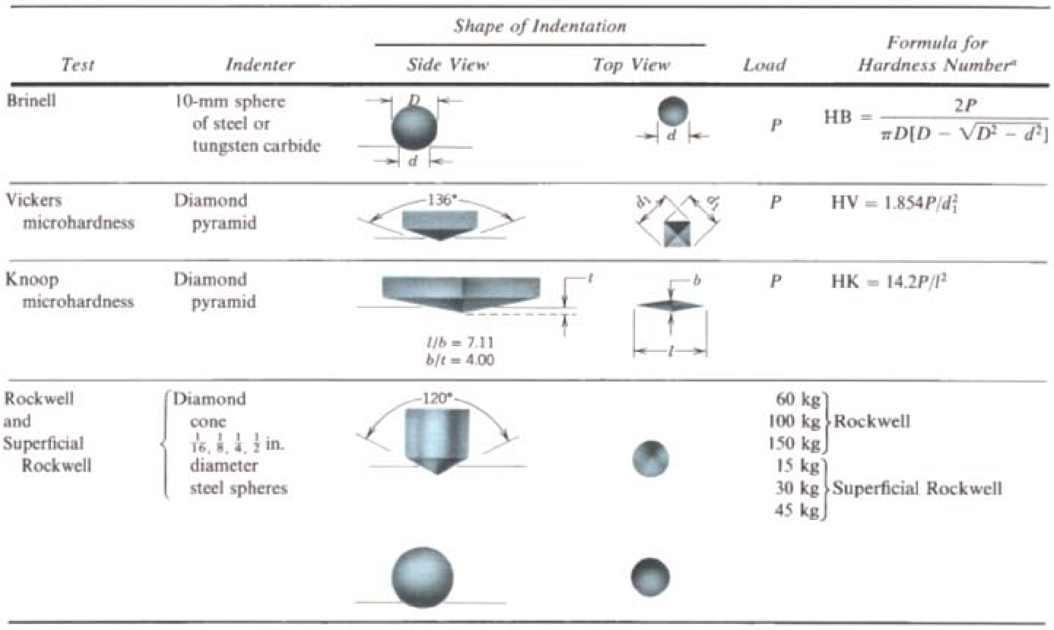

| Test | Indenter | Shape of Indentation: Side View | Shape of Indentation: Top View | Load | Formula for Hardness Number[a] |
|---|---|---|---|---|---|
| Brinell | 10-mm sphere of steel or tungsten carbide | | | $P$ | $HB = \frac{2P}{\pi D[D - \sqrt{D^2 - d^2}]}$ |
| Vickers microhardness | Diamond pyramid | 136° | | $P$ | $HV = 1.854P/d_1^2$ |
| Knoop microhardness | Diamond pyramid | $l/b = 7.11$, $b/t = 4.00$ | | $P$ | $HK = 14.2P/l^2$ |
| Rockwell and Superficial Rockwell | Diamond cone; $\frac{1}{16}, \frac{1}{8}, \frac{1}{4}, \frac{1}{2}$ in. diameter steel spheres | 120° | | 60 kg, 100 kg, 150 kg | Rockwell |
| | | | | 15 kg, 30 kg, 45 kg | Superficial Rockwell |

[a] For the hardness formulas given, $P$ (the applied load) is in kg, while $D$, $d$, $d_1$, and $l$ are all in mm.

**Source:** Adapted from H. W. Hayden, W. G. Moffatt, and J. Wulff, *The Structure and Properties of Materials*, Vol. III, *Mechanical Behavior*. Copyright © 1965 by John Wiley & Sons, New York. Reprinted by permission of John Wiley & Sons, Inc.

**Figure 1.2** Most common indenter shapes [2]

## 1.2 Anisotropy

Anisotropy can be defined as dependence of properties of a material on direction. On a crystallographic basis, the most important reason for anisotropic plastic properties is the crystallographic texture where texture is defined as the preferred orientation of grains. It is generally observed on sheet metals as a result of their crystallographic structure and the rolling process they undergo.

Anisotropy of sheet metals is defined by a quantity called Lankford parameter or anisotropy coefficient which is the ratio of plastic strains in width and thickness directions.

$$r = \frac{\varepsilon_w}{\varepsilon_t} \tag{1.1}$$

The anisotropy coefficient *r* depends on the in-plane direction of a sheet metal. If a tensile test specimen is cut from a sheet where its longitudinal axis is parallel to the rolling direction, then the coefficient $r_0$ is obtained where the subscript denotes the angle between axis of the specimen and rolling direction of the sheet. When this experiment is done in three directions (0˚, 45˚, 90˚) in the plane of sheet metal, then an average of these values which is called *the mean coefficient of normal anisotropy* can be calculated where it is defined as a measure of the deviation of the plastic behavior in the normal direction compared to directions which lie in the plane of sheet [3]. It is given as [3, 4]:

$$\bar{r} = \frac{r_0 + 2 \cdot r_{45} + r_{90}}{4} \tag{1.2}$$

Another quantity *planar anisotropy* gives a measure of the variation of normal anisotropy with the angle to the rolling direction [4].

$$\Delta r = \frac{r_0 - 2 \cdot r_{45} + r_{90}}{2} \tag{1.3}$$

## 1.3 Need for this Study

To obtain material properties before and after production processes is an important requirement in the metal forming industry. It is advantageous to get these properties with reasonable effort and in reasonable time. In addition to traditional formulations and analytical calculations, extensive use of finite element simulations of metal forming processes have revealed increasing need for more precise material data for higher accuracy of results.

On the other hand, there have been lots of studies to determine the relationship between the hardness number and flow stress of the material at a certain representative strain. In this work, it is to be shown that the anisotropy coefficients can also be deduced from the force-displacement curves obtained by special indentation tests. The most prominent reason why indentation is preferred for determination of material peoperties is its ease of performance. In addition, simpler specimens are needed and the process is almost non-destructive.

## 1.4 Aim and Scope

Strong need for material properties in the metal forming industry has lead researchers to investigate new, easy and quick methods to get material characteristics. Being one of those methods which fulfill these requirements, indentation is used for different material characterization tests.

Before material properties can be obtained experimentally, it is quite necessary to have knowledge about process properties and other effects during experiments. The main aim of this study is to investigate indentation process, various effects on force-displacement curves obtained by plane strain indentation process and to obtain force-displacement curves experimentally. This thesis also includes an analytical solution of indentation with upper bound method.

Scope of this thesis is focused on finite element simulations of indentation where simulations are performed using the commercial finite element program MSC. Superform. Effects of friction coefficient, radius of indenter, tilting of indenter, clamping of the specimen or multiple indentations on indentation force-displacement curves are investigated. Upper bound solution of indentation compared with finite element solution is also included. In addition, the thesis covers experimental work and indentation results as well as compression test results.

The thesis text can be divided into mainly seven chapters: Chapter 2 deals with the previous studies in the literature about anisotropy, material characterization by indentation methods and inverse analysis work. In Chapter 3, finite element analysis of indentation and several effects on force-displacement curves again by finite element method are investigated. Chapter 4 will be dedicated to compression test analysis with finite element method where specimen geometries are compared, effect of friction and tilting of the upper punch are analyzed. Chapter 5 will cover upper bound method solution which is an analytical approach to indentation. Chapter 6 will consist of experimental work. It starts with an introduction to the set-up used for the experiments and continues with indentation, compression and tension tests and their results. Finally, main part of this thesis will be closed with discussion and conclusions as Chapter 7. Appendix A is about friction modeling in finite element solution. Appendix B gives material properties used in finite element method and Appendix C gives some mesh topologies used in finite element analyses. Finally, Appendix D presents a table including specimen properties and dimensions used in the experiments.

## 1.5 Collaborative Work

The collaborative project "Determination of Plastic Anisotropy of Metals by Indentation Tests" has been a basis for this thesis. The project is supported by TUBİTAK (The Scientific and Technical Research Council of Turkey) and DFG (German Research Foundation) under the contract name MISAG-DFG-1.

The aim of the project is to determine initial anisotropic yield locus of materials by inverse analysis of the force-displacement curves obtained in special indentation tests. Special indenter geometries are analyzed and produced to get plane strain deformation beneath the indenter. The indenter geometry used in the experiments can be seen in Figure 1.3.

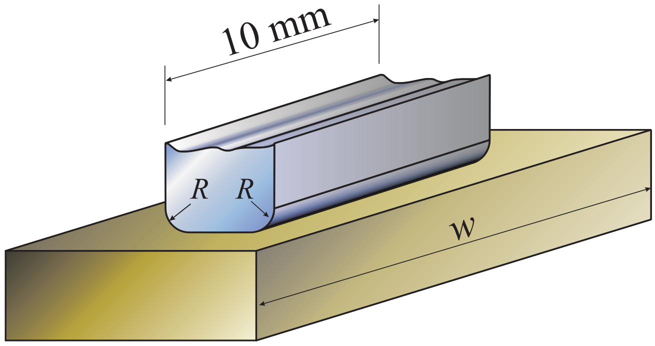


**Figure 1.3** A general picture showing the indenter type used in this study

The basic assumptions to determine anisotropy parameters are as below:

a) *The material is orthotropic*. This assumption is known to be valid for rod or wire type raw material used in bulk forming processes and for sheet type material used in sheet metal forming processes. It must be noticed however, that the orthotropy may be destroyed during the course of deformation.

b) *The plastic flow potential is quadratic*. There is enough evidence to utilize this assumption at least for steel based materials.

c) *Strain-hardening is isotropic*. Although the yield locus is anisotropic, it will be assumed at the beginning that there is no kinematic hardening characteristics of the material. Since only the initial yield locus is to be obtained rather shallow indentations will help to avoid kinematic hardening of the material.

With these assumptions the independent 6 anisotropy parameters characterizing plastic material behavior can be deduced from three measured force-displacement curves during indentation on three mutually orthogonal planes by inverse methods. The inverse methods are based on semi-analytical sensitivity computations by means of forward finite element computations.

The project consists of three subprojects of three universities where the total procedure till parameter identification is shared. The project organization and work share can be seen in Figure 1.4.

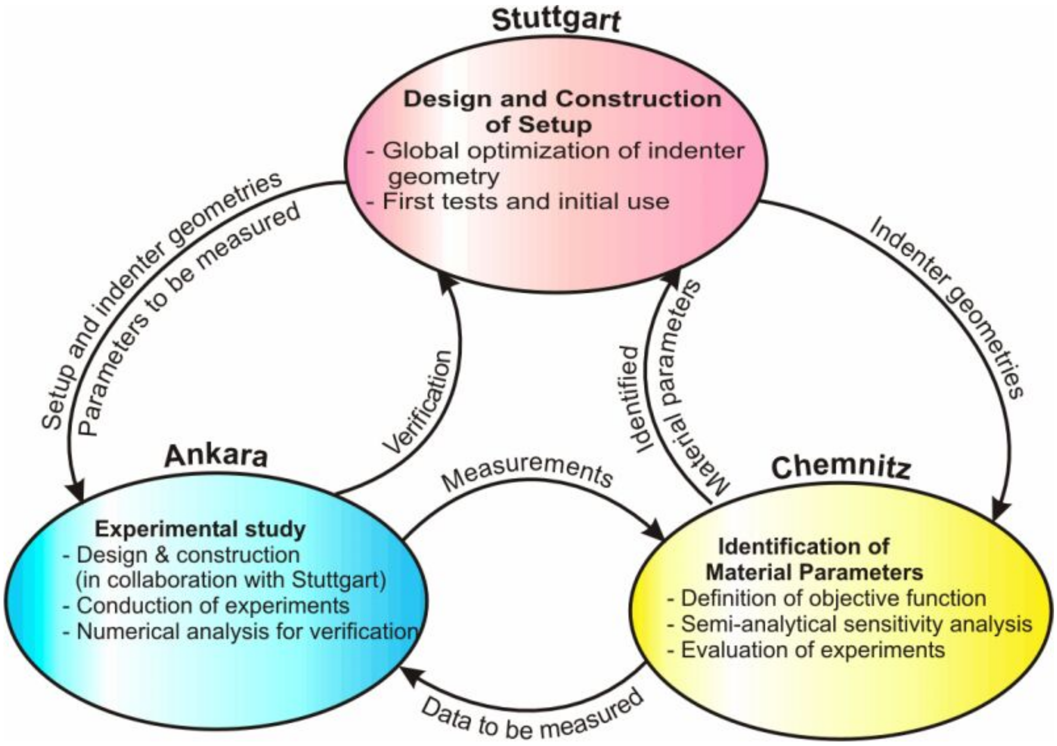


**Figure 1.4** Project Organization

The subproject teams are as below:

**Subproject 1 (SP1):** The aim of this subproject is to design and construct the experimental set-up and to optimize the global geometry of the indenters numerically. Yet, the displacement measurement system used in SP2 is totally designed and produced by SP1 in addition to production of the diamond indenters. This subproject has also supplied SP2 most of the specimens used in experimental part.

**Subproject 2 (SP2):** This subproject aims to verify the experimental set-up numerically and conduct the experiments in addition to finite element analyses.

Finite element analyses cover simulations of indentation processes with different indenter shapes, indenter orientations, friction coefficients, plane strain and three dimensional simulation comparisons in addition to models to determine system elasticity. These simulations are all done to analyze various effects on force-displacement curves.

**Subproject 3 (SP3):** In this subproject it is aimed to identify anisotropy parameters using inverse analysis by semianalytical sensitivities. The inverse analysis program is written so that the inputs are force-displacement curves obtained by SP2 and the outputs are anisotropy coefficients. It works on the plane strain assumption and uses semianalytical methods to determine sensitivities.

# CHAPTER 2

# LITERATURE SURVEY

## 2.1 Introduction

In this chapter literature related to the current study will be discussed. First of all, the yield criteria regarding isotropic and anisotropic materials are named and explained. Then, previous work in the literature on indentation, material characterization by indentation and other work related to parameter identification by inverse analysis methods are presented.

## 2.2 Yield Criteria

If a stressed body returns to its original configuration when all loads are removed then it has been under elastic deformation. For plastic deformation to occur in uniaxial stress state, a particular level of stress must be reached which is defined as the yield strength. Yield criteria are mathematical expressions to define plastification of the material in accordance with experimental observations under multi-axial stress state. Their primary use is to predict when yielding will occur under combined stress states in terms of particular properties of the metal under loading conditions. The most general form is [5]

$$f(\sigma_{11}, \sigma_{22}, \sigma_{33}, \tau_{12}, \tau_{23}, \tau_{13}) = C \tag{2.1}$$

In Eqn. (2.1) normal stress components are denoted by $\sigma$ where the first subscript indicates the normal vector of the surface and the second subscript is the direction of this stress component on this surface. $\tau$ is used for shear stress components and the subscripts have the same meanings.

Eqn. (2.1) can be written in terms of principal stresses as in Eqn. (2.2) where $\sigma_1$, $\sigma_2$ and $\sigma_3$ are the principal stresses in principal directions. Principal stress components are named such that $\sigma_1 \rangle \sigma_2 \rangle \sigma_3$.

$$f(\sigma_1, \sigma_2, \sigma_3) = C \tag{2.2}$$

The yield function may be defined in two different ways. First, by assuming that plastic yielding begins when some physical quantity reaches a critical value, or by approximating experimental data by an analytical function [6].

The yield functions defined by approximating experimental data have the disadvantage of showing poor accuracy since they are not obtained from a calculus based on the crystallographic structure of the material. On the other hand, their advantages are; having simpler mathematical form when compared to criteria based on crystallographic structure, being easier to understand and manipulate like being easily implemented in finite element codes, being easy to be generalized to describe anisotropic behavior of materials. Some may also be adapted easily to describe the behavior of FCC or BCC materials.

### 2.2.1 Yield Criteria for Isotropic Materials

For most isotropic materials whose material properties are said to be independent from direction the following assumptions which have been observed in many instances are invoked:

a) There is no Bauschinger effect which means that the yield strengths in tension and compression are equivalent.
b) Volume is constant.

c) The mean normal stress given by Eqn. (2.3) which is also known to be the hydrostatic pressure does not influence yielding [5].

$$\sigma_m = \frac{\sigma_1 + \sigma_2 + \sigma_3}{3} \tag{2.3}$$

### 2.2.1.1 Tresca Yield Criterion

According to the oldest criterion which was proposed by Tresca in 1864, yielding will occur when the largest shear stress reaches a critical value [4, 5]. If the principal stresses are as $\sigma_1 \rangle \sigma_2 \rangle \sigma_3$, then according to this criterion yielding occurs when

$$\sigma_{\max} - \sigma_{\min} = C \quad \text{or} \quad \sigma_1 - \sigma_3 = C \ \text{if} \quad \sigma_1 \rangle \sigma_2 \rangle \sigma_3 \tag{2.4}$$

In a uniaxial tension test where $\sigma_{\max} = \sigma_1$, $\sigma_2 = \sigma_3 = 0$, yielding occurs when $\sigma_1 = Y$ where *Y* is called the yield strength in uniaxial tension . Thus,

$$\sigma_1 - \sigma_3 = Y = C \tag{2.5}$$

When pure shear is considered where $\sigma_{\max} = \sigma_1$, $\sigma_{\min} = \sigma_3 = -\sigma_1$ and $\sigma_2 = 0$, yielding occurs when the maximum shear stress is equal to the yield strength in pure shear, *k*. Then, $\sigma_1 = k$, so

$$\sigma_1 - \sigma_3 = 2\sigma_1 = 2k = C \tag{2.6}$$

and the Tresca criterion is

$$\sigma_1 - \sigma_3 = Y = 2k \tag{2.7}$$

Hence;

$$Y = 2k \tag{2.8}$$

### 2.2.1.2 Von Mises Yield Criterion

According to this criterion material passes from elastic to plastic state when the elastic energy of distortion reaches a critical value that is independent of the type of the stress state. It was proposed in 1904 by Huber and in 1913 by von Mises and further developed by Hencky. Basis of the criterion is the observation that hydrostatic pressure cannot cause plastic yielding of the material. And the conclusion is that only elastic energy of distortion affects transition from elastic to plastic state.

The criterion is expressed as:

$$(\sigma_1 - \sigma_2)^2 + (\sigma_2 - \sigma_3)^2 + (\sigma_3 - \sigma_1)^2 = 2Y^2 = 6k^2 \qquad (2.9)$$

or, in a more general form, it can be written as:

$$(\sigma_{11} - \sigma_{22})^2 + (\sigma_{22} - \sigma_{23})^2 + (\sigma_{33} - \sigma_{11})^2 + 6(\tau_{12}^2 + \tau_{23}^2 + \tau_{31}^2) = 2Y^2 = 6k^2 \qquad (2.10)$$

Figure 2.1 shows graphical representation of these criteria in the plane of principal stresses for plane strain condition where $\sigma_2 = 0$.

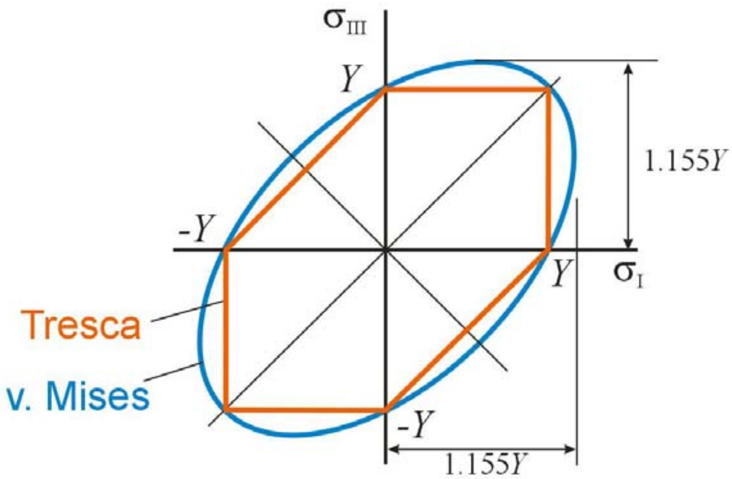


**Figure 2.1** Graphical representation of Tresca and von Mises yield criteria

### 2.2.2 Yield Criteria for Anisotropic Materials

#### 2.2.2.1 Quadratic Yield Criteria

The first yield criterion describing the behavior of materials was proposed by von Mises in the form of a quadratic function which contains products implying both normal and shear stresses [7]. Later, Olszak introduced a generalization of this function for nonhomogeneous anisotropic materials [8]. It can be reduced to a quadratic function of six terms and coefficients of anisotropy for an orthotropic material. Then it becomes the same as the function proposed by Hill in 1948 [4].

*Hill 1948 Yield Criterion*

In 1948 Hill proposed a yield criterion which is a generalization of von Mises criterion for the special case of orthotropy. The yield function is expressed by a quadratic function of the form:

$$F(\sigma_{22}-\sigma_{33})^2+G(\sigma_{33}-\sigma_{11})^2+H(\sigma_{11}-\sigma_{22})^2+2L\tau_{23}^2+2M\tau_{31}^2+2N\tau_{12}^2=1 \tag{2.11}$$

provided that no Bauschinger effect is encountered and the axes of orthotropy are parallel to the reference axes. F, G, H, L, M and N are constants specific to the anisotropy state of the material. For sheet metal generally direction 1 is parallel to the rolling direction, 2 is in the transverse and 3 is in the perpendicular direction.

If the tensile yield stresses in the orthotropy directions are assumed to be $\sigma_{11F}$, $\sigma_{22F}$ and $\sigma_{33F}$ it can be shown that [4, 9]

$$\frac{1}{\sigma_{11F}^2}=G+H \qquad\qquad 2F=\frac{1}{\sigma_{22F}^2}+\frac{1}{\sigma_{33F}^2}-\frac{1}{\sigma_{11F}^2}$$

$$\frac{1}{\sigma_{22F}^2} = H + F \qquad 2G = \frac{1}{\sigma_{33F}^2} + \frac{1}{\sigma_{11F}^2} - \frac{1}{\sigma_{22F}^2} \tag{2.12}$$

$$\frac{1}{\sigma_{33F}^2} = F + G \qquad 2H = \frac{1}{\sigma_{112F}^2} + \frac{1}{\sigma_{22F}^2} - \frac{1}{\sigma_{33F}^2}$$

For the shear yield stresses, analogous relations are obtained as [4, 9]:

$$2L = \frac{1}{\sigma_{23F}^2}, \qquad 2M = \frac{1}{\sigma_{13F}^2}, \qquad 2N = \frac{1}{\sigma_{12F}^2} \tag{2.13}$$

In order to give a complete description of the anisotropy of the material six independent yield stresses ($\sigma_{11F}, \sigma_{22F}, \sigma_{33F}, \sigma_{12F}, \sigma_{13F}, \sigma_{23F}$) have to be known in addition to the orientation of the principal anisotropy axes.

If the flow rule

$$\dot{\varepsilon}^p = \dot{\lambda} \frac{\partial f(\sigma)}{\partial \sigma} \tag{2.14}$$

is applied to Hill's yield condition given by Eqn. (2.10), the following relations are obtained:

$$\dot{\varepsilon}_{11}^p = \dot{\lambda}\left[H(\sigma_{11} - \sigma_{22}) + G(\sigma_{11} - \sigma_{33})\right] \tag{2.15}$$

$$\dot{\varepsilon}_{22}^p = \dot{\lambda}\left[F(\sigma_{22} - \sigma_{33}) + H(\sigma_{22} - \sigma_{11})\right] \tag{2.16}$$

$$\dot{\varepsilon}_{33}^p = \dot{\lambda}\left[G(\sigma_{33} - \sigma_{11}) + F(\sigma_{33} - \sigma_{22})\right] \tag{2.17}$$

$$\dot{\varepsilon}_{23}^p = 2\dot{\lambda} L \sigma_{23} \tag{2.18}$$

$$\dot{\varepsilon}_{13}^p = 2\dot{\lambda} M \sigma_{13} \tag{2.19}$$

$$\dot{\varepsilon}_{12}^p = 2\dot{\lambda} N \sigma_{12} \tag{2.20}$$

In case of plane strain deformation, deformation is not seen in one of the three possible directions. Therefore, for plane strain case in three orthogonal directions which can be noted as $\dot{\varepsilon}_{11}^{p}=0$, $\dot{\varepsilon}_{22}^{p}=0$ and $\dot{\varepsilon}_{33}^{p}=0$ the following are obtained. For $\dot{\varepsilon}_{11}^{p}=0$ case, from Eqn. (2.15) the following is obtained:

$$\sigma_{11}=\frac{H\sigma_{22}+G\sigma_{33}}{H+G} \tag{2.21}$$

Taking into account that $\dot{\varepsilon}_{12}^{p}=\dot{\varepsilon}_{13}^{p}=0$ it follows from (2.19) and (2.20) that $\sigma_{12}=\sigma_{13}=0$. Considering Eqn. (2.21) and Eqn. (2.11) leads to the yield condition related to the case $\dot{\varepsilon}_{11}^{p}=0$:

$$\left(\frac{FG+GH+HF}{H+G}\right)(\sigma_{22}-\sigma_{33})^{2}+2L\sigma_{23}^{2}=1 \tag{2.22}$$

And for the two remaining cases, analogous yield conditions are obtained as:

$$\left(\frac{FG+GH+HF}{F+H}\right)(\sigma_{33}-\sigma_{11})^{2}+2M\sigma_{13}^{2}=1 \tag{2.23}$$

$$\left(\frac{FG+GH+HF}{F+G}\right)(\sigma_{11}-\sigma_{22})^{2}+2N\sigma_{12}^{2}=1 \tag{2.24}$$

In the Eqn.s (2.22), (2.23) and (2.24) it can be seen that in the 2-3,1-3 and 1-2 planes respectively, isotropy is obtained. Inverting the directions in these planes does not change the value of the yield condition in these particular cases. This effect is called transversal anisotropy [9].

For sheet metal forming processes, if the anisotropy coefficients are denoted by $r_0, r_{45}$, and $r_{90}$ and the yield stresses in the directions of the principal anisotropy axes are $\sigma_{11F} = \sigma_0$, $\sigma_{22F} = \sigma_{90}$ then the relations between the coefficients in Hill 1948 yield criterion and the anisotropy coefficient are obtained as:

$$r_0 = \frac{H}{G}, \qquad r_{90} = \frac{H}{F}, \qquad r_{45} = \frac{H}{F+G} - \frac{1}{2} \tag{2.25}$$

It can be shown that the following relation holds between yield stresses and anisotropy coefficients.

$$\frac{\sigma_0}{\sigma_{90}} = \sqrt{\frac{r_0(1+r_{90})}{r_{90}(1+r_0)}} \tag{2.26}$$

For the plane strain case and the case that principal directions of the stress tensor are coincident with the anisotropy axes, Hill 1948 yield criterion takes the following form by substitution of Eqn. (2.25) and Eqn. (2.26) in Eqn. (2.11) after some steps [6].

$$\sigma_1^2 - \frac{2r_0}{1+r_0}\sigma_1\sigma_3 + \frac{r_0(1+r_{90})}{r_{90}(1+r_0)}\sigma_3^2 = \frac{r_0(1+r_{90})}{r_{90}(1+r_0)}\sigma_{90}^2 \tag{2.27}$$

Referring to Eqn. (2.27) it can be deduced that three mechanical parameters are needed to define yielding under plane stress condition, the coefficients $r_0$ and $r_{90}$ and one of the uniaxial yield stresses $\sigma_0$ and $\sigma_{90}$. Eqn. (2.27) represents families of ellipses depending on parameters $r_0$ and $r_{90}$ where the dependence of yield loci on these parameters is seen in Figure 2.2.

In case where materials have only normal anisotropy i.e. $r_0 = r_{90} = r$ from Eqn. (2.26), $\sigma_0 = \sigma_{90}$ and Eqn. (2.27) takes the form given by Eqn. (2.28).

$$\sigma_1^2 - \frac{2r}{1+r}\sigma_1\sigma_3 + \sigma_3^2 = \sigma_u^2 \tag{2.28}$$

where $\sigma_u$ is the uniaxial yield stress.

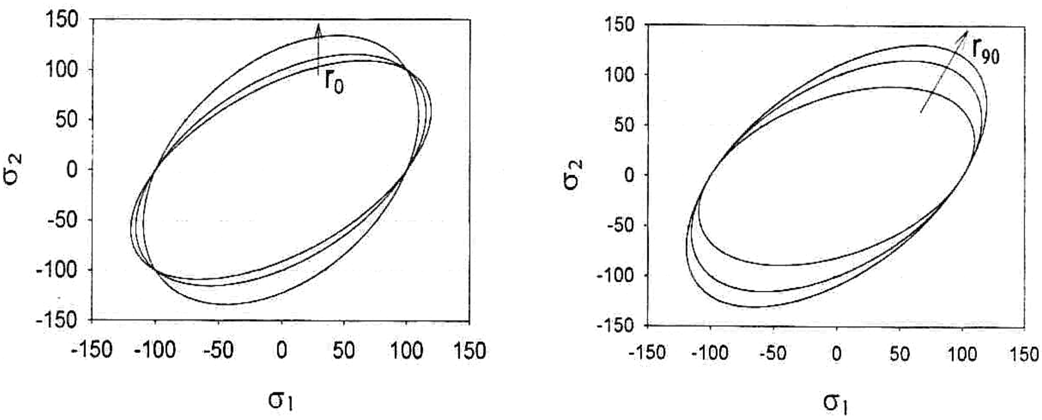


**Figure 2.2** Effects of anisotropy coefficients $r_0$ and $r_{90}$ on the shape of yield locus defined by Hill 1948 [4].

For $r < 1$ the yield locus predicted by Hill 1948 criterion is located inside yield locus by von Mises and for $r > 1$ it is outside yield locus by von Mises. Woodthrope and Pearce [10, 11] have seen that some materials, in particular aluminum alloys, have their yield locus outside the von Mises surface even though their r-coefficient was less than unity.

This behavior cannot be explained by Hill 1948 yield criterion and materials of this kind are called “anomalous” [6].

The Hill 1948 yield criterion can be used for simple approximations where the use for materials exhibiting anomalous behavior should be avoided. It is one of the most frequently used yield criteria by the commercial programmes because of its simplicity.

### 2.2.2.2 Non-Quadratic Yield Criteria

Hill's 1979 yield criterion was proposed to describe the anomalous behavior which includes a variable exponent [12, 13]. Eqn. (2.29) gives the yield criterion as:

$$f\left|\sigma_2-\sigma_3\right|^m+g\left|\sigma_3-\sigma_1\right|^m+h\left|\sigma_1-\sigma_2\right|^m+a\left|2\sigma_1-\sigma_2-\sigma_3\right|^m$$
$$+b\left|2\sigma_2-\sigma_3-\sigma_1\right|^m+c\left|2\sigma_3-\sigma_1-\sigma_2\right|^m=\sigma_{eq}^m \qquad (2.29)$$

Later, Hosford has proposed a special case of Hill's 1979 yield criterion which is valid for fcc and bcc materials where exponent *m* is 6 for bcc and it is 8 for fcc in Eqn. (2.30) [12].

$$\left|\sigma_1-\sigma_2\right|^m+\left|\sigma_2-\sigma_3\right|^m+\left|\sigma_3-\sigma_1\right|^m=2\sigma_{eq}^m \qquad (2.30)$$

Hosford has comments on anisotropic yield criteria as well as suggestions for modification of one of them in [14].

A more general form of Hosford's yield criterion for isotropic materials where the x, y, z coordinate system is not necessarily coincident with principal axes was later proposed by Barlat [15, 16].

In 1990, Hill proposed a generalized form of his 1979 criterion which was also valid when the orthotropic axes are coincident with the directions of principal stresses [6]. And later in 1993, the criterion is improved by Hill in [17] which covers not only the anomalous behavior but also the anomalous behavior of the second order. Anomalous behavior of second order is used for aluminum alloys and brass to explain having almost equal yield stresses but different anisotropy coefficients in rolling and transverse directions.

In 1991 Barlat has proposed a general six-component yield criterion that could be adopted with no restrictions to any stress state, and in [18] Barlat *et al*. proposed a more general expression of his 1991 yield criterion.

In addition Gotoh, Zhou, Montheillet, Banabic-Balan, Budiansky, Ferron and others have had studies on yield criteria [4]. These criteria can be extended up to today such as the works of Hu in [19].

*Conclusions*

Among all these yield criteria Hill's 1948 yield criterion is explained and investigated deeply. Although it is not directly related with this thesis topic, the determination of plastic anisotropy of metals part covers this yield criterion. This criterion is strongly recommended for use to obtain simple approximations of the anisotropic behavior of materials. It has a simpler definition, it is easier to handle and different from the other criteria that it does not necessitate determination of the equibiaxial yield stress.

## 2.3 Previous Work on Multiple Indentations

Meguid *et al*. in [20] have analyzed simultaneous indentations of a surface with two punches sufficiently close to each other such that there could be interference between the two associated deformation zones. They have tried to find answers to the questions:

- *How far apart do the two punches have to be before they act completely independently, so that the deformation and loads for each punch is the same as for a single punch?*

- *How deep does the strip have to be before the deformation is localized at the surface instead of being spread through the thickness of the strip?*

This study is closely related with fields where the interactions between the plastic zones play an important role in development of compressively stressed layers. Some examples may be the friction and wear, shot-peening, ball and roller bearing technology, the theory of ploughing of asperities or of abrasive grains and surface finish studies as well as material hardness testing by indentation.

In this work, co-indentation is analyzed by the slip-line and upper bound theories. They have had etching experiments with flat plane and spherical headed rigid punches. It is worth to have a detailed look at their experimental results for co-indentation which will be referred to in the following chapters not only for the behavior of the force-displacement curves but also for comparison with finite element results for multiple indentations and simultaneous indentations. The experimental results of co-indentation published in [20] for different spacing of the two indenters are given in Figure 2.3 for flat plane and in Figure 2.4 for spherical headed punches.

In this thesis, the effect of depth of the workpiece on force-displacement curves or on interactions between the two punches are not analyzed. So, the important conclusion of this work of Meguid *et al*. [20] is that "the separation was found to have negligible effect on the force-indentation curve when $c/a \geq 3$, but for smaller separations the force required to produce a given displacement decreased with decreasing values of $c/a$".

As an extension of the analysis of co-indentation experimentally using etching techniques and theoretically using the upper bound theorem in [20], Meguid *et al*. have analyzed the effect of interference ratio, the height and the strain-hardening characteristics of the bounded solid upon the plastic zone development, the indentation pressure-punch displacement relationships and the unloading residual stresses using the finite element method in [21].

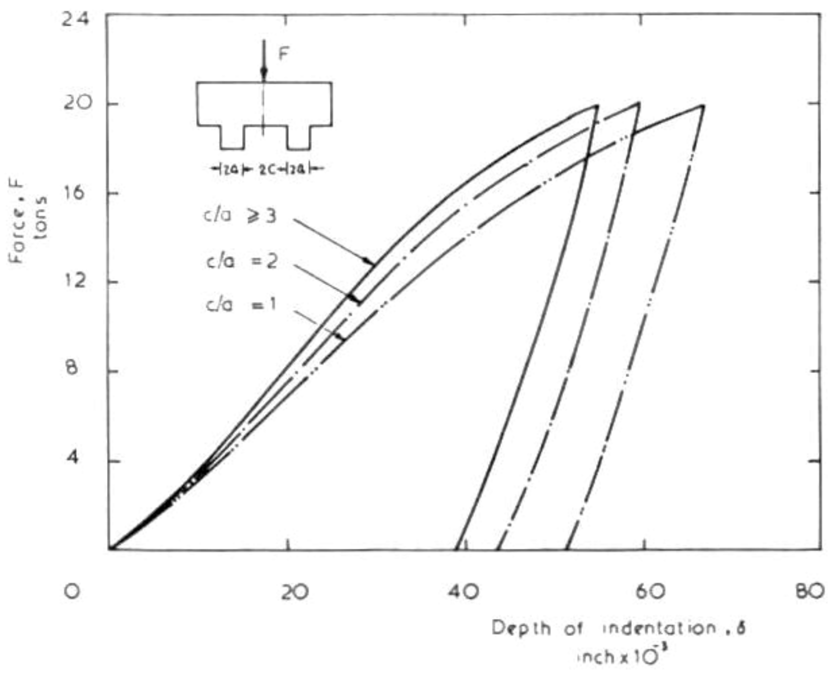


**Figure 2.3** Experimental results of co-indentation for flat plane punches.

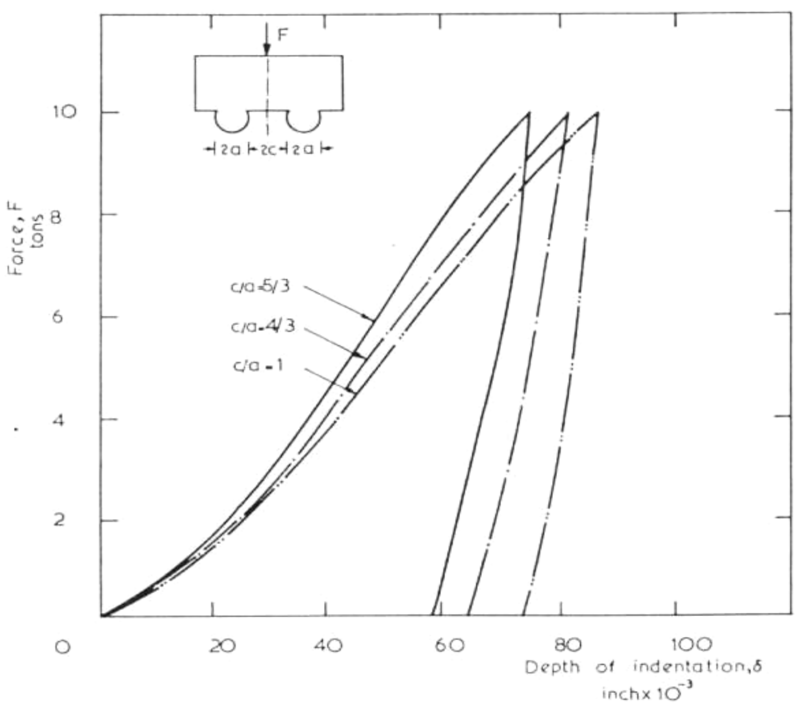


**Figure 2.4** Experimental results of co-indentation for spherical headed punches.

Meguid *et al*. have realized an appreciable discrepancy between the finite element approach in [21] and the upper bound solution in [20]. The upper bound solution in the previous work can be considered less than adequate. In [22], almost the same case is investigated but this time for a special case like shot-peening. The effect of separation distance between two shots and unloading residual stresses are investigated. In addition the effect of strain hardening rate of the target upon the development and spread of the plastic zone is analyzed.

## 2.4 Previous Work on Indentation and Parameter Identification by Inverse Analysis

Analytical relationships between hardness and yield stress are rooting back to the works of Bishop, Hill and Mott [23], and Hill, Lee and Tupper [24]. In 1948, Tabor [25] proposed a method to determine the stress-strain curve using the results of spherical indentation experiments. Since then several methods have been proposed to extract the basic mechanical properties of materials such as modulus of elasticity, yield strength and strain hardening exponent from load-displacement curves.

Sharp indenters are selfsimilar, so that they allow the determination of a singular flow stress independent of the depth of indentation. Furthermore, because of their geometry they produce higher strain gradients and hence have a higher resolution. Spherical indenters, on the other hand, supply a large amount of information about the material behavior since they pass through different strain and stress states during indentation. But for the present study non-selfsimilar indenters are to be used because of the larger amount of information required in the inverse analysis procedure.

In [26], Grunzweig, Longman and Tupper have applied slip-line field solutions to plane strain indentation. Axisymmetric problems have been analyzed firstly by Lockett [27] utilizing the slip-line field method. Johnson [28] suggested a relationship between the hardness and yield stress for a wedge type of indentation using a cavity with internal pressure model. Another model of axisymmetric cone indentation based on an upper bound theory has been given by Bay and Wanheim [29].

The relationship between hardness measurements and yield stress in cold worked materials has been investigated in depth by Dannenmann *et al*. [30] and Wilhelm [31]. In their experimental study they conducted impact extrusion tests with various steel types and then measured the Vickers hardness at different locations of the specimens. By determining semi-analytically the local plastic equivalent strains by the visio-plasticity method they obtained some correlations. Another interesting study has been performed by Ramaekers [32]. Ramaekers analyzed the simple tension test and the shearing process in regard to Vickers hardness measurements. He obtained flow curves by hardness measurements during shear tests, which lie by about 15 to 25 % above the standard flow curves.

Tekkaya [33] has repeated Tabor's experiments numerically by means of the finite element method. During virtual experiments material behavior is taken as elasto-plastic type. Although after cold forming it is known that materials show more or less anisotropic behavior, isotropic hardening mode is assumed. Considering low tool velocity during indentation, it is assumed that deformation is temperature and velocity independent. No frictional effect is put on the indentation process, and common three-dimensional Vickers indentation process is replaced by a cone indentation process, so that virtual experiments have become axisymmetric. Equivalent cone angle is selected such that the displaced volume of material for the same depth of penetration is the same for pyramidal and conical indenter.

For the analysis, mesh shown in Figure 2.5 is used and test is conducted with commercial software MSC/Marc. This mesh has been a good example and very similar meshes are used for two-dimensional plane strain indentation finite element models in this thesis.

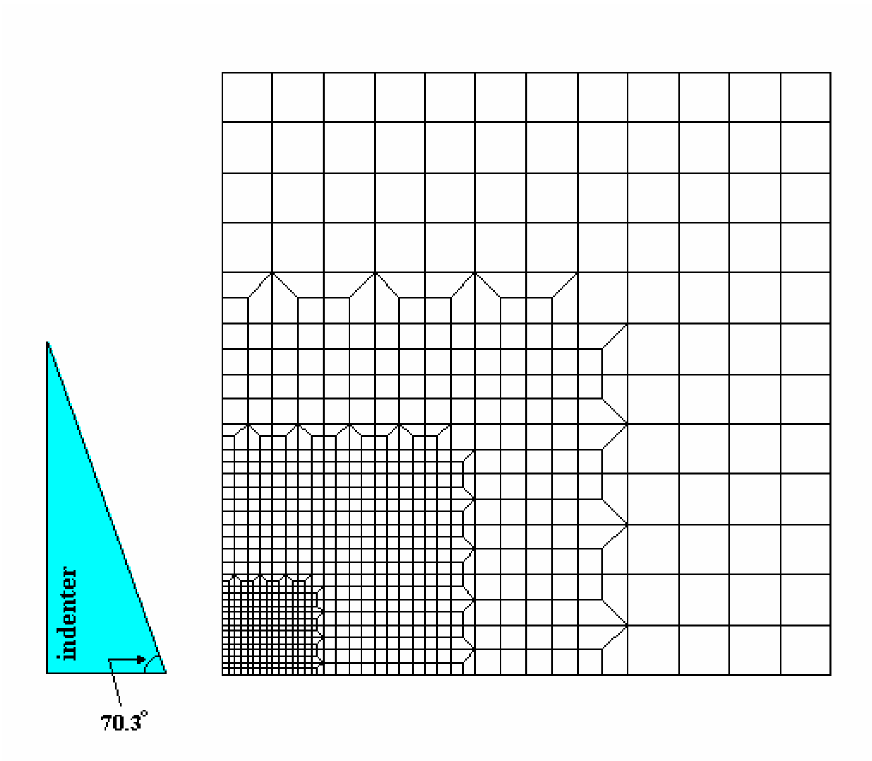


**Figure 2.5** Mesh used for virtual hardness measurement test

Another recent study in this field was a study to identify the extent to which the elasto-plastic properties of ductile materials could be determined from instrumented sharp indentation by Dao *et al*. in [34]. In this work forward and reverse analysis algorithms were developed. Unique indentation response for a given set of elasto-plastic properties can be calculated by forward algorithms whereas reverse analysis algorithms enable extraction of elasto-plastic properties from a given set of indentation data. Figure 2.6 is an example of experimental and computational responses taken from [34] in sharp indentation case.

Later Bucaille *et al*. [35] have extended Dao's approach and investigated the effect of included angle of conical indenters and the friction coefficient on the force-penetration curves.

Attaf [36] has investigated the loading curve of indentation. He has analyzed the formulas such as Kick's law, Bernhardt formula, Bückle's empirical equation, Meyer's power law and their modified or corrected forms. These formulae are valid for sharp indentations and include a load-independent geometrical factor. In this work, Attaf has shown that all these formulas are various truncated forms of an integer power series of the load in terms of penetration depth.

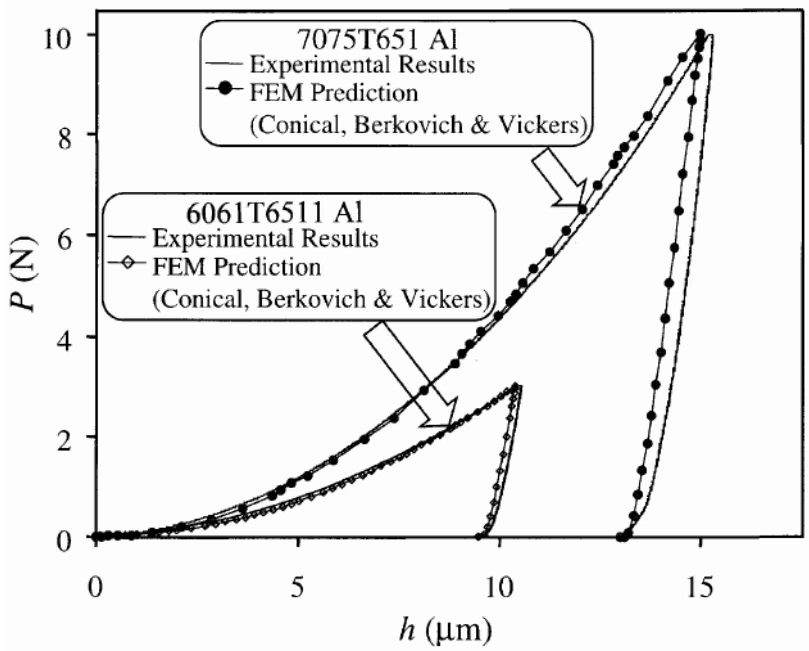


**Figure 2.6** Experimental vs. computational indentation responses of both the 7075-T651 aluminum and 6061-T6511 aluminum specimens [34]

Nakamura *et al*. [37] have used instrumented indentation to determine properties of functionally graded materials (FGM's). They have utilized an inverse analysis technique to extract information from force-displacement data beyond usual parameters such as modulus of elasticity.

The Kalman filter technique is used to estimate through-thickness compositional variation and a rule-of-mixtures parameter that defines effective properties of FGM's. Nakamura *et al*. [38] have also presented a new indentation method for characterization of homogeneous elastic-plastic materials. In addition, the load-displacement curves given in Figure 2.7 (b) are similar to the work in this thesis where different radii are compared experimentally and by finite element analysis.

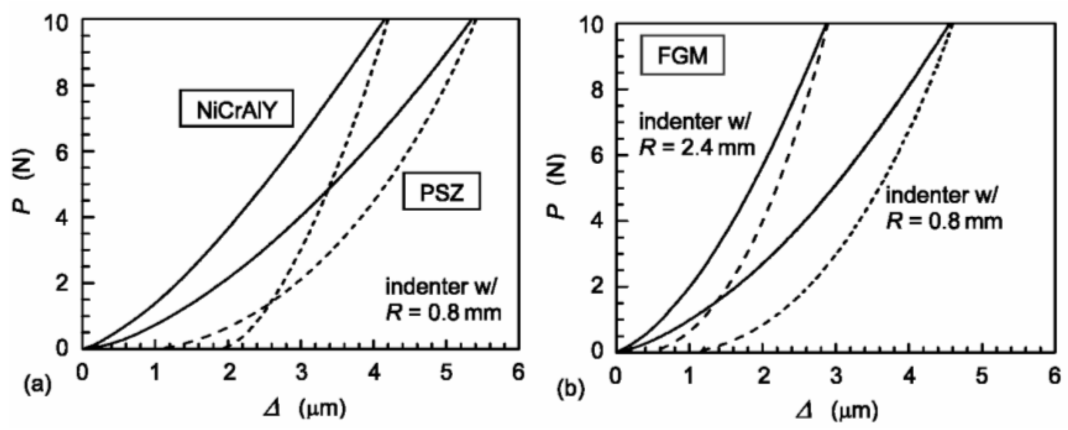


**Figure 2.7** Experimentally measured load-displacement records from micro-indentation by spherical indenters: (a) PSZ and NiCrAlY with indenter $R$ = 0.8 mm. (b) FGM with indenters $R$ = 0.8 and $R$ = 2.4 mm. Each curve represents average of about 10 indentations [38].

Bolzon *et al*. [39] have worked on identification of elastic-plastic material parameters by means of indentation tests. They have considered finite element analysis of indentation also. The inverse analysis is carried out by a deterministic approach using conventional algorithms. In addition, friction between indenter and specimen is investigated. Cho and Ngaile have used finite element based inverse analysis techniques to determine flow stress and friction at the tool and workpiece interface [40]. The inverse analysis works by minimizing the error between experimental data and finite element analysis results as aimed at the end of the present work.

Capehart *et al*. [41] have also studied the problem of determining the elastic modulus, yield stress and strain hardening exponent to define the isotropic stain-hardening model from a single force-displacement curve with a sharp conical tip. The sensitivity of the parameter confidence intervals was determined using grids which were formed by triple combinations of material parameters $E$, $Y$ and $n$.

## 2.5 Conclusions

Anisotropic properties of materials have been investigated and yield criteria for such materials have been developed starting from the mid 1900's. Anisotropy is a very important aspect when metal forming is considered. Not only in bulk metal forming but also in sheet metal forming the effects of anisotropic properties of the material are considerable. Especially forming limit diagrams are affected by anisotropy of the metal.

Being a simple and rapid method, indentation is used to determine various properties of materials. Although it is very common to use indentation as a method of hardness measurement, it is seen that indentation is consulted to determine other properties like resistance to abrasives or wear, ductility, modulus of elasticity, yield strength or fracture toughness.

Determination of the yield strength and elastic modulus of materials is a widely investigated method. In these methods, self similar indenters can be used. After sufficient experience with the indentation process, forward and inverse analysis methods have been developed for material characterization combined with instrumented indentation.

# CHAPTER 3

# FEM ANALYSES OF INDENTATION

## 3.1 Introduction

In this chapter, finite element analysis results of indentation will be given. The indenter cross-section used in the analyses is as given in Figure 3.1. It has a flat base and fillets at the corners.

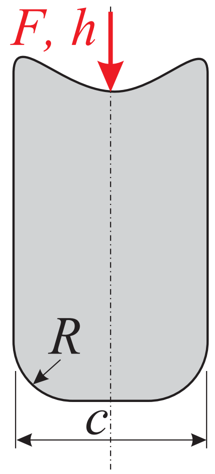


**Figure 3.1** Indenter cross-section

Two-dimensional plane strain models have generally been used and three-dimensional models have been built where necessary. Finite element analyses start with a convergence study of the mesh used and also convergence check for the relative force tolerance is performed.

This chapter includes two and three dimensional analyses of indentation with several material properties. First, plane strain analyses are done to investigate effect of radius, effect of friction, effect of tilting of indenter in transverse direction, effect of relative sliding velocity. Three dimensional analyses are performed to investigate effect of relative sliding velocity and effect of tilting in the longitudinal direction. Finally experimental results are investigated. These are again modeled in two-dimensions with plane strain assumption. The triple indentation case is investigated first. The results have shown the reason of unexpected force-displacement behavior observed during experiments. This case is analyzed with a full model without symmetry plane. Then, the half-symmetric model is constructed to model effect of distance change between the three indentations. As final part of multiple indentations a half-symmetric model is constructed in order to investigate the findings of Meguid *et al.* [20,21] where there are two indenters penetrating into the material simultaneously.

The flow curves and elastic properties of materials used in these analyses are given in Appendix B.

## 3.2 Two-dimensional (Plane Strain) Analyses

The two dimensional models start with analyses of the indenter type given in Figure 3.1. Indentation is modeled as in Figure 3.2. Since the process is symmetric, only half of the indenter and workpiece are modeled. A horizontal line is chosen to be the symmetry axis and the workpiece rests on a base die.

The workpiece is modeled as a deformable body whereas the indenter and the base die are rigid bodies. Being a deformable body, the workpiece is divided into 6319 four-node quadrilateral elements with minimum edge length of 0.03125 mm. These parameters are decided after analysis of effect of mesh topology on convergence (see Section 3.2.1).

Table 3.1 gives basic assumptions and properties of the plane strain finite element model.

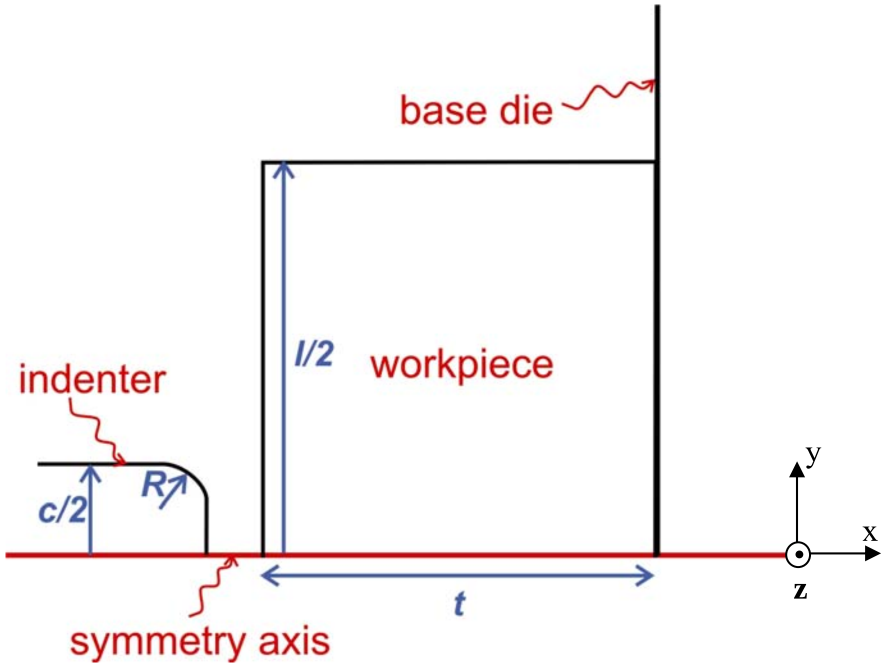


**Figure 3.2** Plane strain model of indentation

**Table 3.1** Basic assumptions and properties of plane strain FEM model

| | | | | | |
|---|---|---|---|---|---|
| **Problem Types Analyzed:** | 2-D Plane Strain | | | | |
| **Material Law:** | Elastic-plastic (isotropic) | | | | |
| **Dies and Indenters:** | Rigid | | | | |
| **Friction Model:** | Nodal Stress based Coulomb | | | | |
| **Indenter Speed:** | 0.5 mm/s | | | | |
| **Finite Element Class:** | Quad 4 (bi-linear) | | | | |
| **Remeshing:** | None | | | | |
| | R=c/2 | R=c/3 | R=c/4 | R=c/6 | R=c/8 |
| **Displacement of the indenter (mm):** | 0.2 | 0.15 | 0.1 | 0.075 | 0.075 |
| **Number of Increments:** | 320 | 280 | 240 | 220 | 220 |
| **Total Loadcase Time (s):** | 0.8 | 0.7 | 0.6 | 0.55 | 0.55 |

### 3.2.1 Effect of Mesh Size and Topology

For the two-dimensional analysis case an appropriate mesh was to be created. It was necessary to have finer mesh in the region where deformation occurs and a coarse mesh where no deformation is observed. The main aim of this study was to get smoother force-displacement curves. If elements with constant edge length throughout the workpiece were used, either unnecessarily more calculation time and memory would be spent for the case of fine mesh or the deformation would not be able to be observed correctly for the coarse mesh case. The workpiece is modeled with dimensions $l$ = 20 mm and $t$ = 10 mm where the width is taken as 10 mm.

For this purpose the first mesh topology used was the one given in Figure 3.3. Later, mesh topologies with four and five transition regions were also developed. The mesh with five transition regions seen in Figure 3.5 has shown to have best convergence for this study.

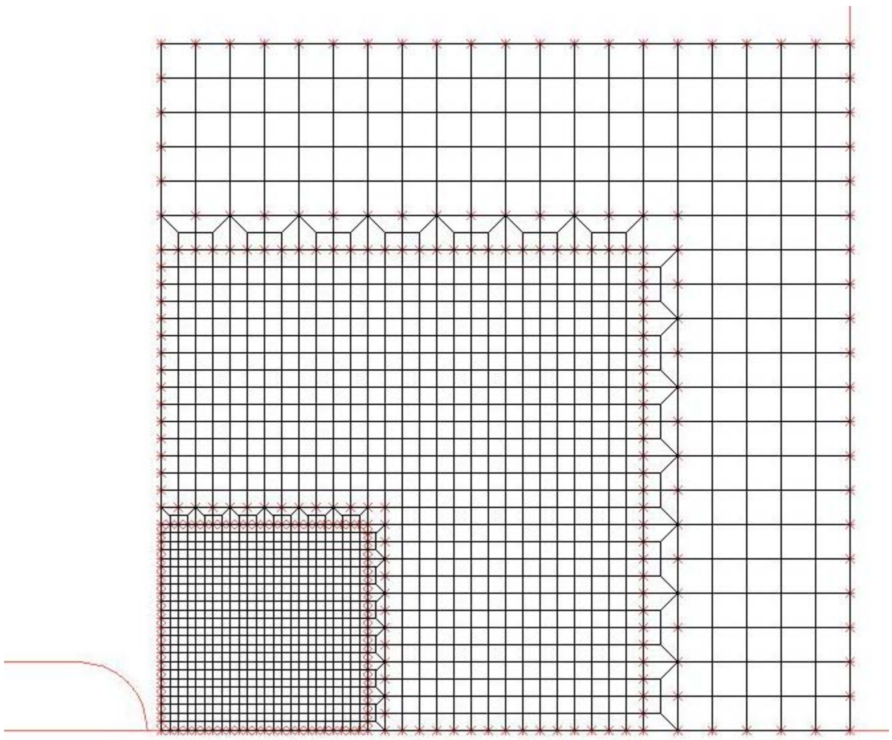

**Figure 3.3** Mesh 1: 1524 elements

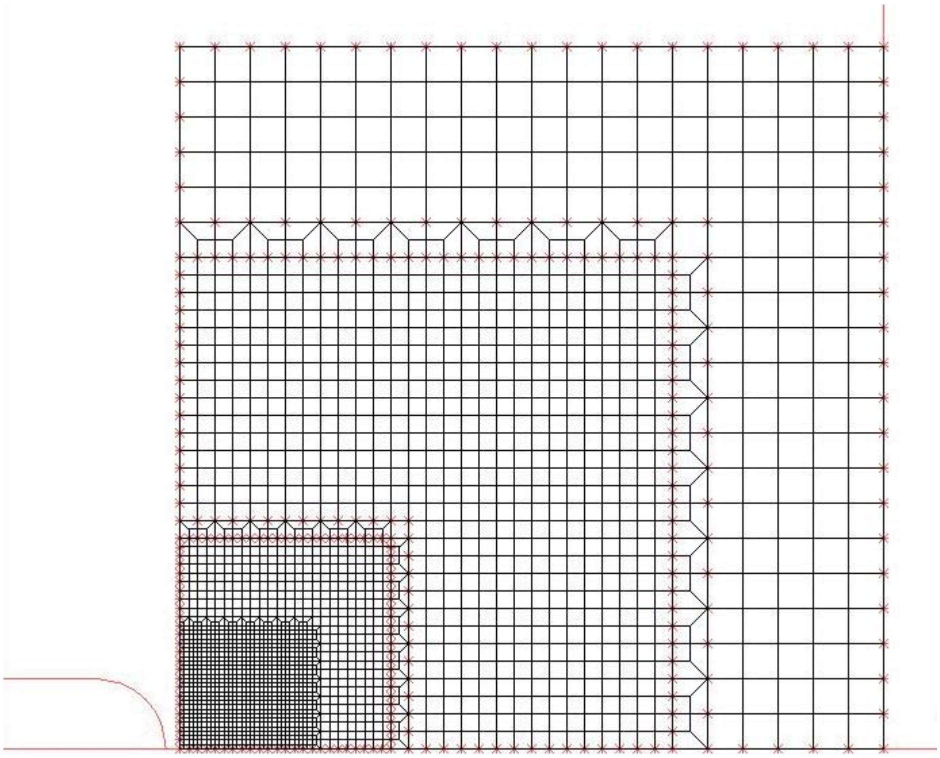

**Figure 3.4** Mesh 2: 1792 elements

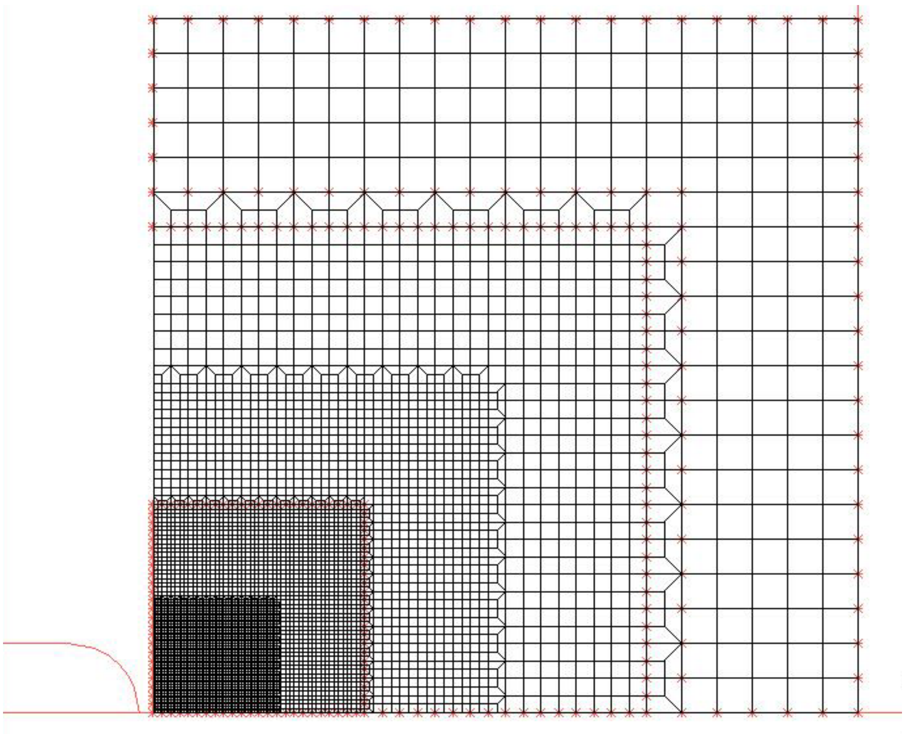

**Figure 3.5** Mesh 3: 6319 elements

The effect of element size and mesh topology on force-displacement curves is seen in Figure 3.6. The mesh with five transition regions results in smoother force-displacement curves. Therefore, it is decided to use the third mesh given in Figure 3.5 throughout the analyses.

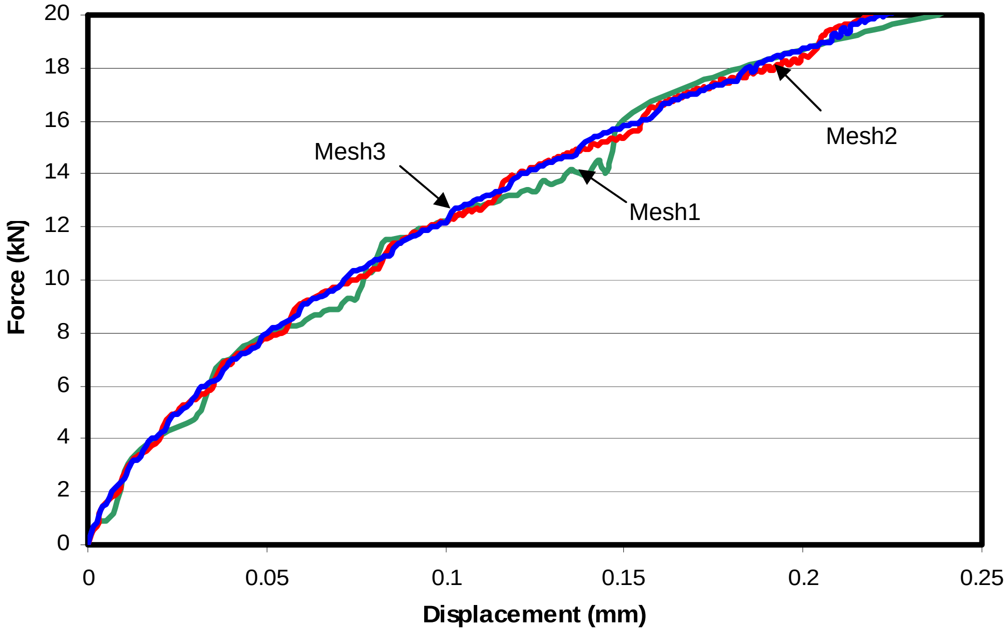


**Figure 3.6** Effect of mesh topology on force-displacement curves (Material: C15, $R = c/2 = 1$ mm, $\mu = 0.1$)

### 3.2.2 Effect of Relative Force Tolerance

For selection of relative force tolerance to be used throughout the analyses some simulations with different relative force tolerances have been done. Relative force tolerance ($\delta$) is the ratio of the residuals to reactions in terms of norms.

$$\delta = |\text{Residual force}| \,/\, |\text{Reaction force}| \tag{3.1}$$

For example, for $R = 0.33$ mm case simulation is run two times for $\delta = 0.03$ and $\delta = 0.02$, where $\delta$ is the relative force tolerance.

And, it is seen that for smaller relative force tolerance values smoother curves are obtained as in Figure 3.7.

The effect of relative force tolerance is much more dominant in Figure 3.8 where the force-displacement curves for indenter with $R = c/8$ and Coulomb coefficient of friction $\mu = 0.05$ are seen.

Even though decreasing the relative force tolerance value is advantageous to get smoother curves, smaller relative force tolerance values prevent to reach convergence of the solution for some cases. For this reason, relative force tolerance is taken to be 0.01 for the simulations and when convergence cannot be reached it is assigned as 0.02.

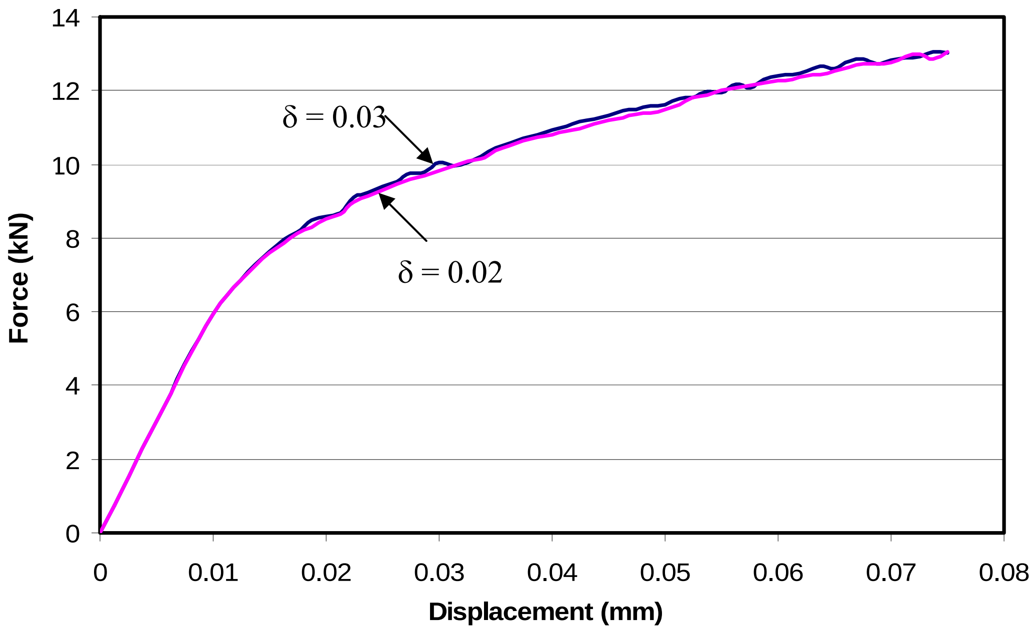


**Figure 3.7** Force-displacement curves for two different δ

(Material: CuZn30, $R = c/6 = 0.33$ mm, $\mu = 0.15$)

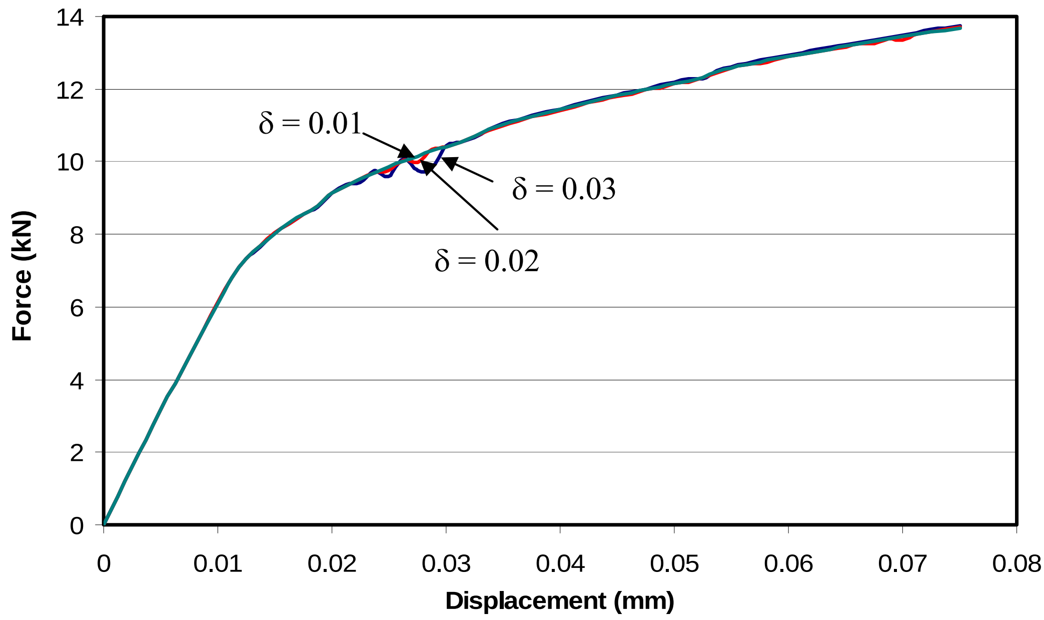


**Figure 3.8** Force-displacement curves for two different δ

(Material: CuZn30, $R = c/8 = 0.25$ mm, $\mu = 0.05$)

### 3.2.3 Effect of Indenter Radius

Radius effect analysis has been done to see the force-displacement relationships and how the curves are affected by change of radius. In order to analyze the effect of change of radius the ratio $R/c$, where $R$ and $c$ can be seen in Figure 3.1, is varied between 0.5 and 0.125. For this purpose, $c$ is kept constant at 2 mm and $R$ is given values as 1 mm, 0.66 mm, 0.5 mm, 0.33 mm and 0.25 mm. For comparison of simulation results for different indenter radii, it is assumed that there is no friction for all simulations.

Figure 3.9 shows the force-displacement curves obtained by finite element method calculations. Since $c$ is kept constant, increasing $R$ results in less force to penetrate into the material. In other words the indenter with longer flat part at the base needs higher forces and indenter with smaller flat portion needs smaller forces for same amount of penetration into the material. This is simply explained by the fact that with higher $R$ the cross-sectional area of the indenter in contact with the workpiece material is lower for the same amount of displacement, so less force is needed for plastification of the material.

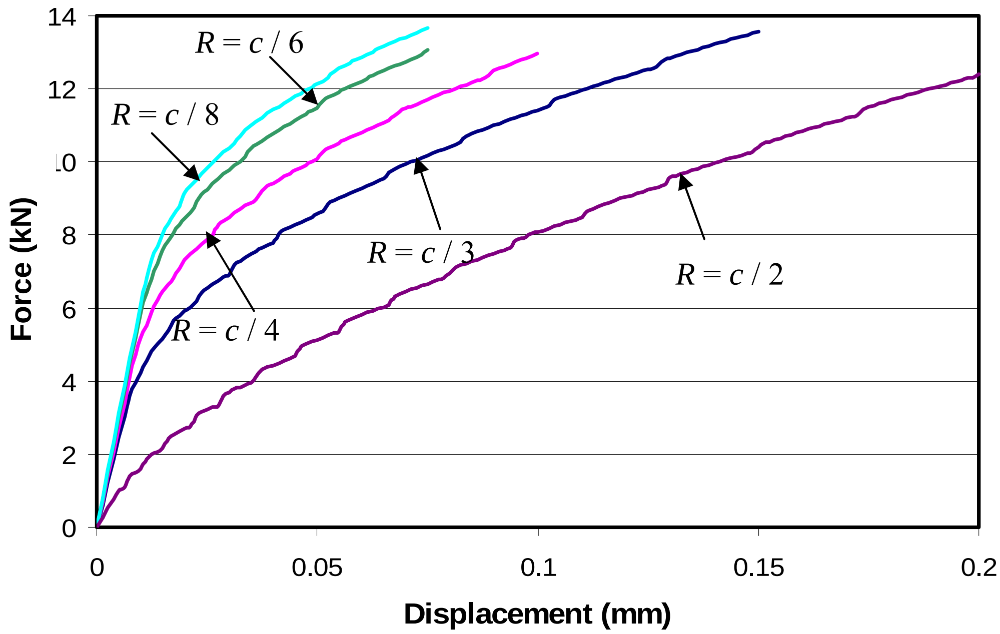


**Figure 3.9** Effect of radius (Material: CuZn30, $\mu = 0$, $c = 2$ mm)

According to the graph given in Figure 3.9 the indenter with $R = c / 3$ gives compromising values among the other indenters. Using this type of indenter a broader range of indentation depth can be obtained. Experiments with very little penetrations into the material can be done and still the same behavior as others can be observed. On the other hand higher indentation depths can be obtained for the maximum capacity, 2 tons, of the press.

$R / c = 0.33$ is chosen for production of the indenter. The indenter used in the experiments has radius $R = 0.68$ mm and width $c = 1.56$ mm, so the analyses after production of the indenter continued with the true dimensions of the indenter.

### 3.2.4 Effect of Friction

The effect of friction on force-displacement curves are analyzed by assigning different values to Coulomb coefficient of friction such as 0, 0.05, 0.1 and 0.15. Force-displacement curves obtained for different Coulomb friction coefficients for $R$ = 1 mm are seen in Figure 3.10. It is observed that, for all radii the effect of changing friction coefficient is negligible.

This analysis is also necessary to have an idea how the friction between the indenter and the workpiece surface will affect the force-displacement curves when experiments are considered.

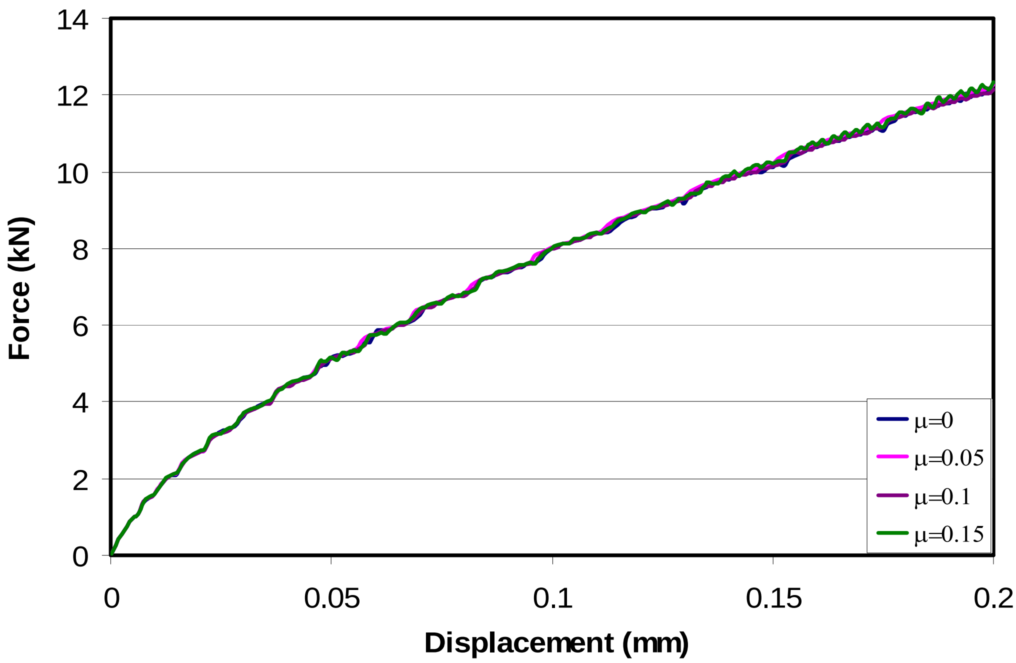


**Figure 3.10** Effect of friction (Material: CuZn30, $R = c/2 = 1$ mm, $\delta = 0.02$)

### 3.2.5 Effect of Relative Sliding Velocity

Relative sliding velocity is a parameter which affects the effectiveness of the friction coefficient. For smaller relative sliding velocity parameter values the effectiveness of the friction coefficient increases. The relative sliding velocity parameter and its default value used by the program is explained in Appendix A.

For this purpose, different from the default relative sliding velocity value, smaller values are used to check if the friction effects using the default value can be improved or not. When no value is specified for relative sliding velocity, it appears as 0 and the values used are as in Appendix A. For three different computations, the default value, $10^{-7}$ and $10^{-10}$ are used as relative sliding velocity, the force-displacement curves are as seen in Figure 3.11 where C denotes the relative sliding velocity parameter.

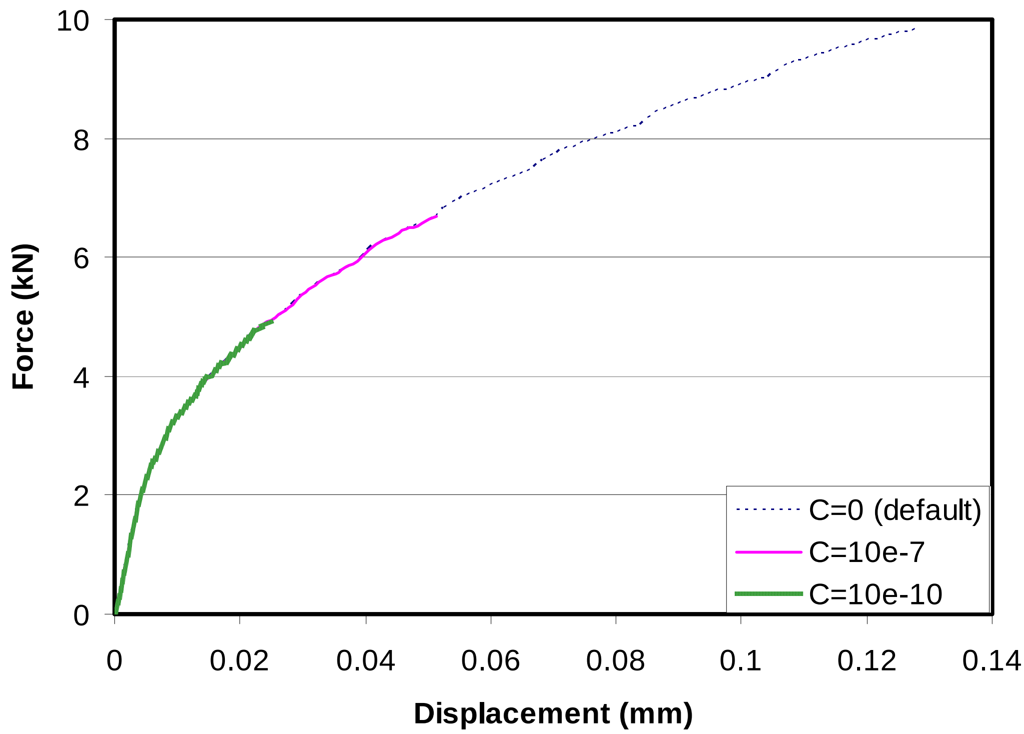


**Figure 3.11** Effect of relative sliding velocity

(Material: C15, $R = 0.68$ mm, $c = 1.56$ mm, $\mu = 0.1$)

Decreasing the relative sliding velocity hindered reaching convergence till the end of process. But from Figure 3.11 it is obvious that up to the displacement of the indenter where convergence is obtained, relative sliding values do not affect force-displacement curves. This also shows that the friction effect analyses with the default values of relative sliding velocity are sufficient for the purpose of this thesis.

### 3.2.6 Effect of Material

The same finite element model is used to model the process for two different materials, CuZn30 and C15 whose material data can be seen in Appendix B**.**

Comparison of force-displacement curves for these materials is seen in Figure 3.12. As expected, indenter needs higher forces to penetrate into C15 than CuZn30, since the yield stresses are higher for C15 when compared with CuZn30.

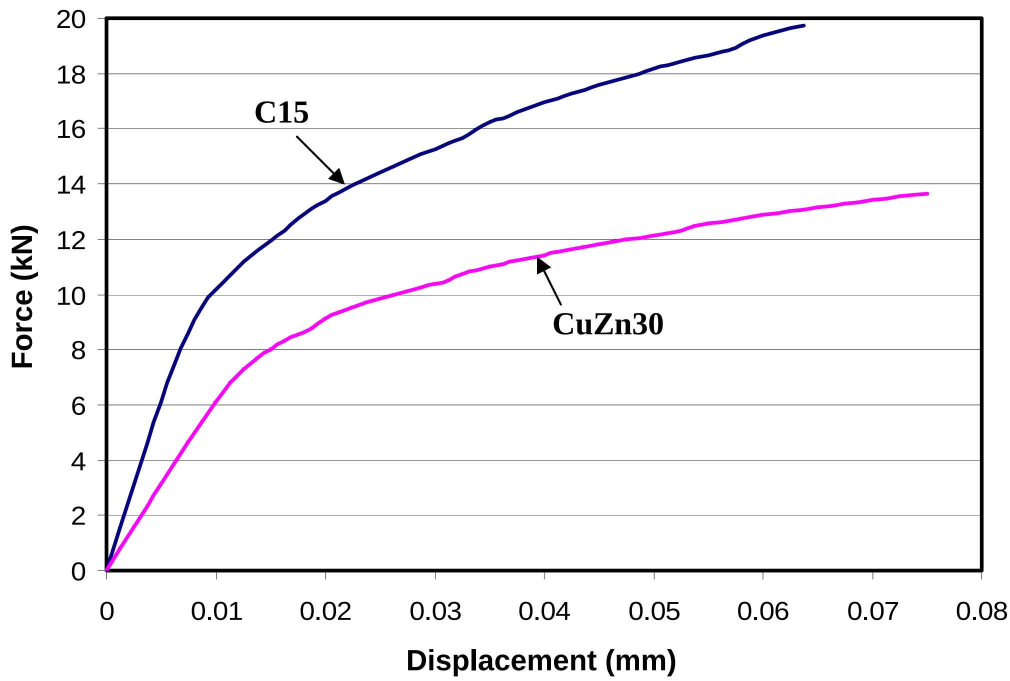


**Figure 3.12** Effect of material ($R = c/8$, $\mu = 0$)

### 3.2.7 Effect of Tilting of Indenter in Transverse Direction

Considering the possibility that the indenter may tilt during experiments, it was a question how and how much it would affect the experiment results. The tilting mentioned here could occur in two planes, in longitudinal or in transverse directions. It is possible to perform the analysis of tilting of indenter in transverse direction with two-dimensional model, but without symmetry. Tilting in longitudinal direction is analyzed by a three dimensional model which is given in Section 3.3.2.

The model for analysis of the tilting problem is different from the model in Figure 3.5 in that the workpiece and the indenter are not symmetrically modeled but mirrored with respect to the symmetry line. When the angle between the flat surface of the indenter and the specimen surface is called β as seen in Figure 3.13, β is assigned 0.5°, 1° and 2° in addition to the 0° angle which is the ideal case. The effects of change of this angle can be seen in Figure 3.14.

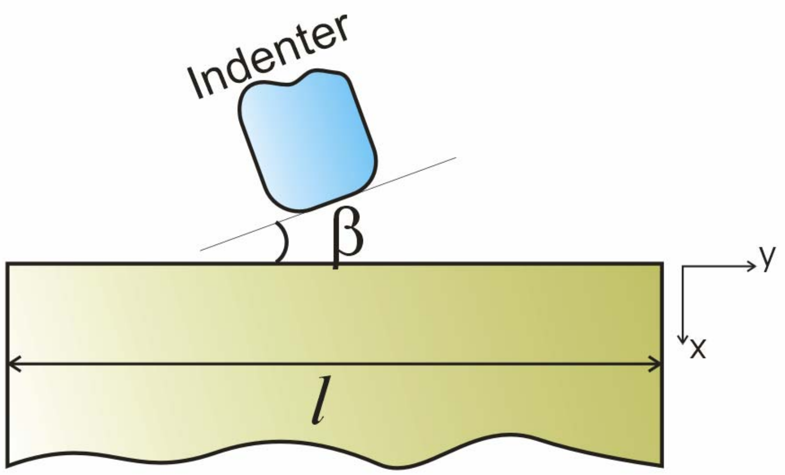


**Figure 3.13** β angle of indenter

The finite element results show that tilting with respect to z-axis causes differences in force-displacement curves. The effect is more obvious especially at the beginning of indentation. This can be explained by the fact that with increasing tilt angle, the cross-sectional area penetrated into the specimen is smaller and therefore, the forces are smaller.

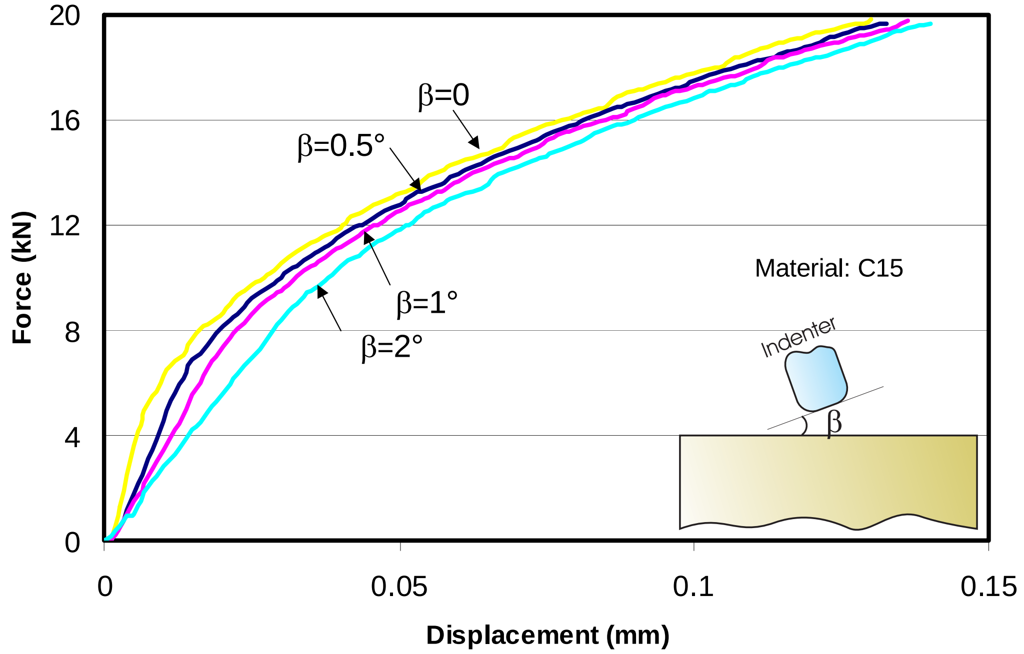


**Figure 3.14** Effect of β angle on force-displacement curve

(Material: C15, $R = 0.68$ mm, $c = 1.56$ mm, $\mu = 0$)

## 3.3 Three-dimensional Analyses

Three-dimensional finite element analyses have been conducted mainly to investigate plane strain deformation conditions. The model used is seen in Figure 3.15.

In addition, for calculations where it is not possible to use plane strain analysis, a three-dimensional finite element model is used. Construction of the model, convergence analyses, plane strain and three-dimensional comparisons and some other studies with three dimensional model can be found in [42]. The parameters for this model are given in Table 3.2.

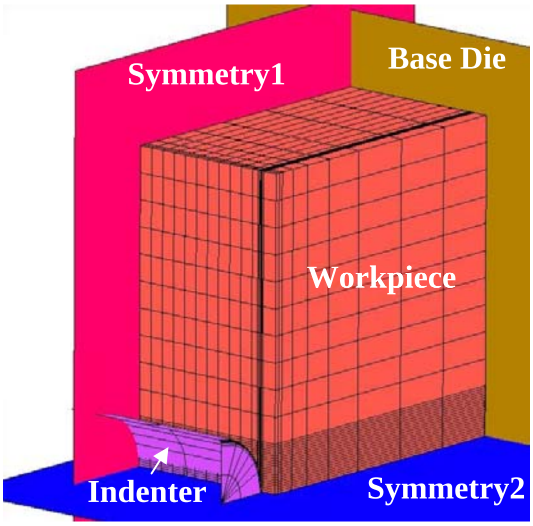


**Figure 3.15** 3D finite element model of indentation

**Table 3.2** 3D finite element model of indentation

| | |
|---|---|
| Analyzed problem types | 3-D |
| Material law | Elasto-plastic (isotropic) |
| Dies and indenters | Rigid |
| Friction model | Nodal Stress based Coulomb law |
| Indenter speed | 0.5 mm/s |
| Finite element class | |
| Remeshing | None |
| Number of elements | 4743 |
| Minimum edge length | 0.05625 mm |
| Number of increments | 500 fixed time steps |
| Total loadcase time | 1.5 sec. |
| Termination | Maximum force (4905 N) |

### 3.3.1 Effect of Relative Sliding Velocity

In order to have a complete analysis of the effect of relative sliding velocity and to check if it is right to use the default values also for the three-dimensional model, it was necessary to do the analysis again with the three-dimensional model. Because referring to increasing friction results the plane strain and three-dimensional results are compared and it is deduced that increasing the coefficient of friction does not help to get plane strain conditions. Details of this analysis are in [42, Chapter 4].

Figure 3.16 gives force-displacement curves obtained by changing the relative sliding velocity parameter in the simulation by model given in Figure 3.15.

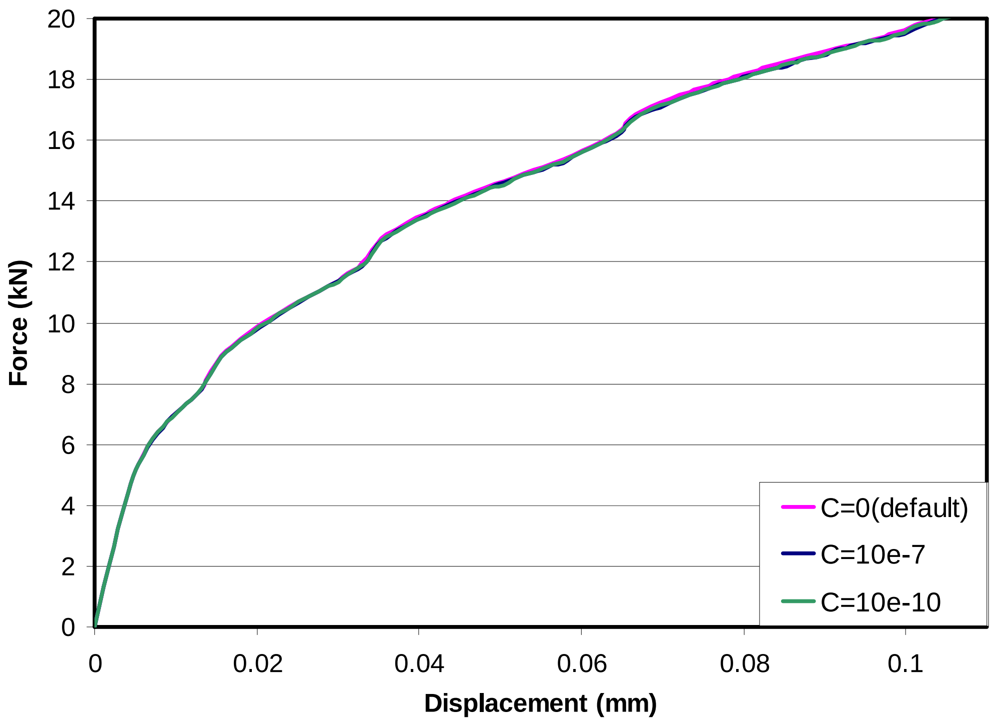


**Figure 3.16** Effect of relative sliding velocity

(Material: C15, $R = 0.68$ mm, $c = 1.56$ mm, $\mu = 0.1$)

### 3.3.2 Effect of Tilting of Indenter in Longitudinal Direction

In order to have a complete analysis of tilting, tilting of the indenter in longitudinal direction needed to be analyzed in addition to the analysis of tilting in transverse direction. Longitudinal tilting of the indenter is named as $\alpha$ in this text and this angle can be seen in Figure 3.17.

These angles can occur not only because of the tilting of the indenter but also because of the non-parallel surface of the specimens to the plane of indenter. The reasons may be the manufacturing steps of the specimens or the specimen may not be resting on a smooth surface.

A three dimensional model is used to see the effect of angle $\alpha$ whereas the previously used two dimensional plane strain model is enough to see effect of angle $\beta$. The symmetry plane *symmetry 1* in Figure 3.15 is removed and half of the process is modeled instead of a quarter. The specimen has a width of 25 mm and a length of 20 mm where the thickness is 10 mm. The indenter is the same as the indenter used in experiments which is 10 mm long, $c$ = 1.56 mm and $R$ = 0.68 mm.

Figure 3.18 shows the effect of angle $\alpha$ on force-displacement curves. In this figure it is seen that with increasing $\alpha$ the beginning of the curves show a different curvature. And, with increasing tilt angle the forces decrease up to the point where the whole length of the indenter is embedded in the specimen.

The main difference in the two tilting cases, Figure 3.13 and Figure 3.17, is related with the surface area of the indenter in contact with the specimen. From Figure 3.18 it can be seen that for smaller $\alpha$ which is about one tenth of $\beta$, the effect is still prominent and even more than that observed in Figure 3.14.

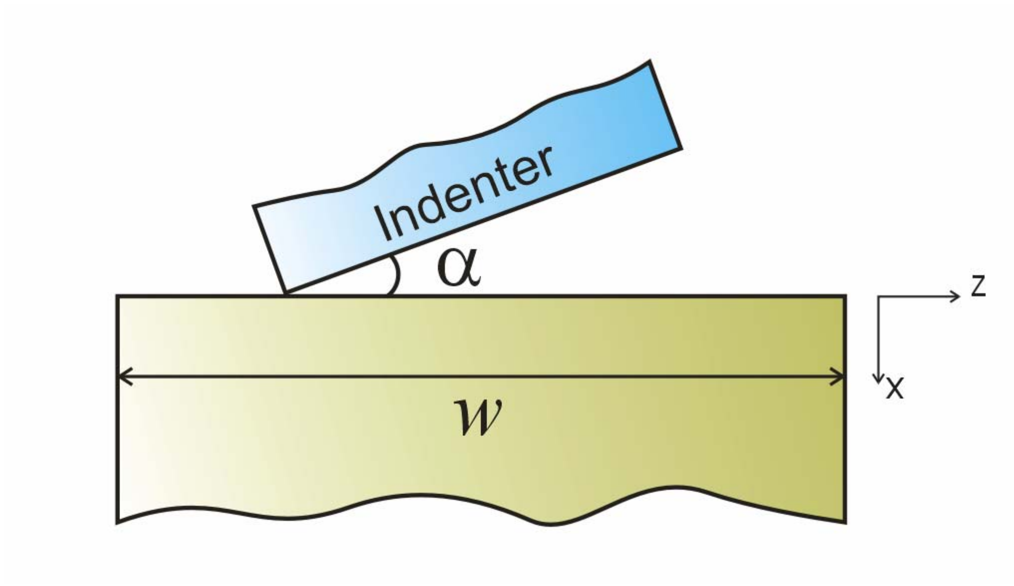


**Figure 3.17** Definition of α angle of indenter

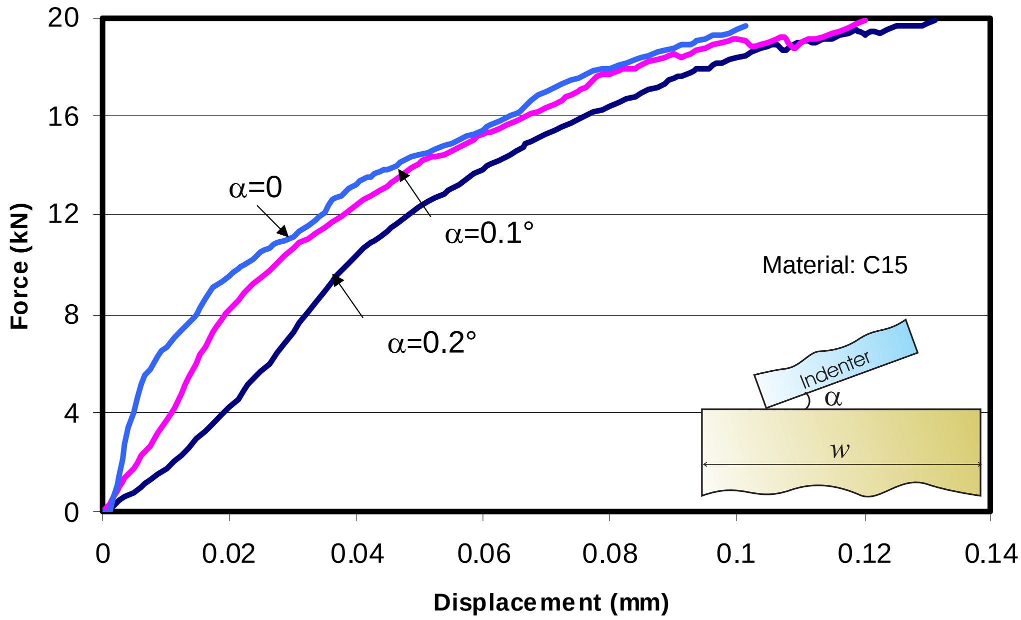


**Figure 3.18** Effect of α angle on force-displacement curve

(Material: C15, $R = 0.68$ mm, $c = 1.56$ mm, $\mu = 0.1$)

## 3.4 Analyses of Experimental Results

Different from the preliminary analyses, which have been dedicated to parameter studies, in this section the experiment results have been analyzed. The triple indentation case and the effect of clamping of the specimen were necessary to analyze in order to understand the experimental findings. In all the analyses in this section, the parameters $c$ = 1.56 mm and $R$ = 0.68 mm for the indenter have been used.

### 3.4.1 Analysis of Multiple Indentations

In this part, answers to two questions which have aroused during experiments are looked for: When there is more than one indentation applied on one specimen how the force-displacement curves respond and what the minimum distance between the two indentations should be.

#### 3.4.1.1 Multiple-Sequential Indentation

In one set of experiments, one specimen is used to determine three force-displacement curves. With three different specimens, nine experiments have been performed. The idea was to reduce the effort and time to replace the specimen with a new one as well as to reduce the number of specimens.

In Figure 3.19, the order of indentation on the specimen can be seen. The first two indentations were applied at the sides whereas the third was applied in the middle. This order was so selected to have equal distances between the imprints. First the specimen is placed to the limit where the other edge remains still under the reference table, then second indentation is done on the other side where same precaution is taken for the previous edge. Finally, the specimen is placed such that the third imprint is in the middle of the previous two.

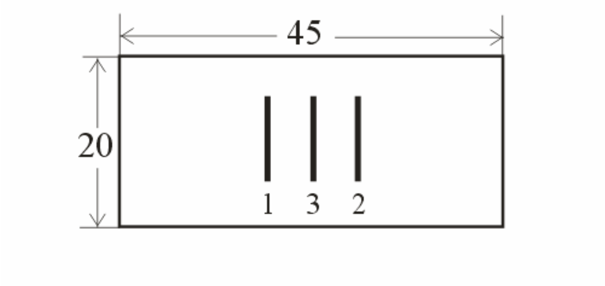


**Figure 3.19** Order and placements of indentations on one specimen

These experiment results for the indentation applied in the middle of the other two revealed force-displacement curves different from what is expected. For each three specimen the force-displacement curve for the third indentation was above those of the other two. Experiment results for this set of indentations can be seen in Section 6.4.3.2. Since this situation is the same for all three specimens, this is not an experimental error.

A possible reason for the difference between the force-displacement curves was thought to be the effect of strain hardening. Because the two indentations on both sides were performed previously and could have been causing plastic deformation also in the middle portion of the specimen.

Another reason was the effect of residual stresses. Some stress distribution in the material could be causing a different stress state from the others at the beginning of third indentation. Referring to finite element simulations, the real reason for this abnormal behavior could have been found. To see the reason of higher forces for the third indentation finite element simulations are done.

In the experiment, the ratio $d/c$, where $d$ is the distance between two indentations and $c$ is the width of the indenter, was taken to be 3 (Figure 3.20). The representation in Figure 3.20 is used to model the case faced in experiments. First of all this case is analyzed, and later the minimum distance for such a case where the force-displacement curves of the indentation in the middle is not affected is to be found.

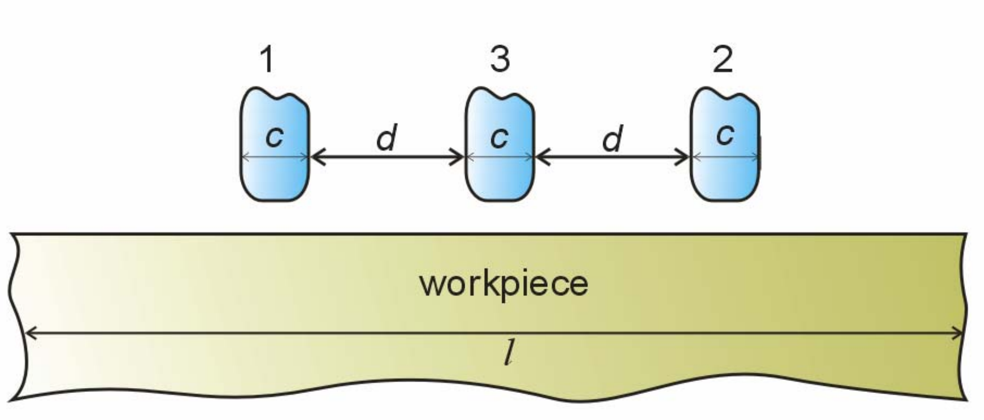


**Figure 3.20** Triple indentations

For the analyses to find the minimum distance $d$, a symmetry line is used such that the first and second indentations are modeled to be applied at the same time. Since the spacing between indentations 1 and 2 is enough for them not to affect each other as shown in the forthcoming sections, such an assumption is acceptable and advantageous in that the number of elements decreases to a half, number of loadcases reduce to two from three. These reduce the calculation time considerably.

The model to find the minimum distance between indentations can be seen in Figure 3.21.

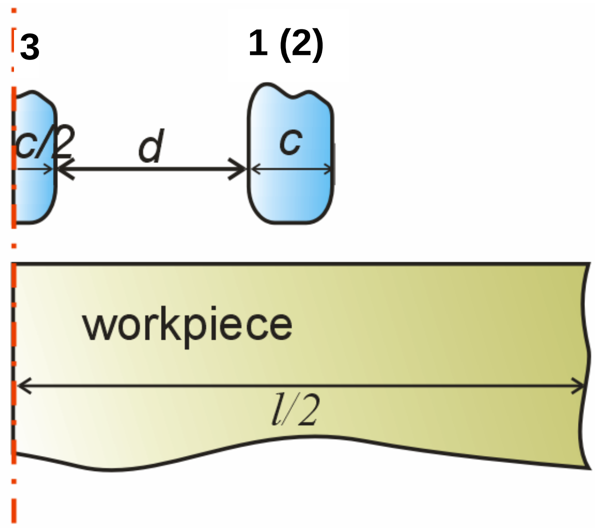


**Figure 3.21** Model to find minimum distance between indentations

### 3.4.1.1.1 Modeling Conditions and Assumptions

In this two-dimensional analysis of triple indentations the mesh is developed from the mesh seen in Figure 3.5. In the finite element model, specimen dimensions are the same as the real case. The length of the specimen is taken as 45 mm and the thickness is 16 mm, in addition the width of the specimen is assigned as 10 mm. The model consists of 39210 elements. The model is as seen in Figure 3.22.

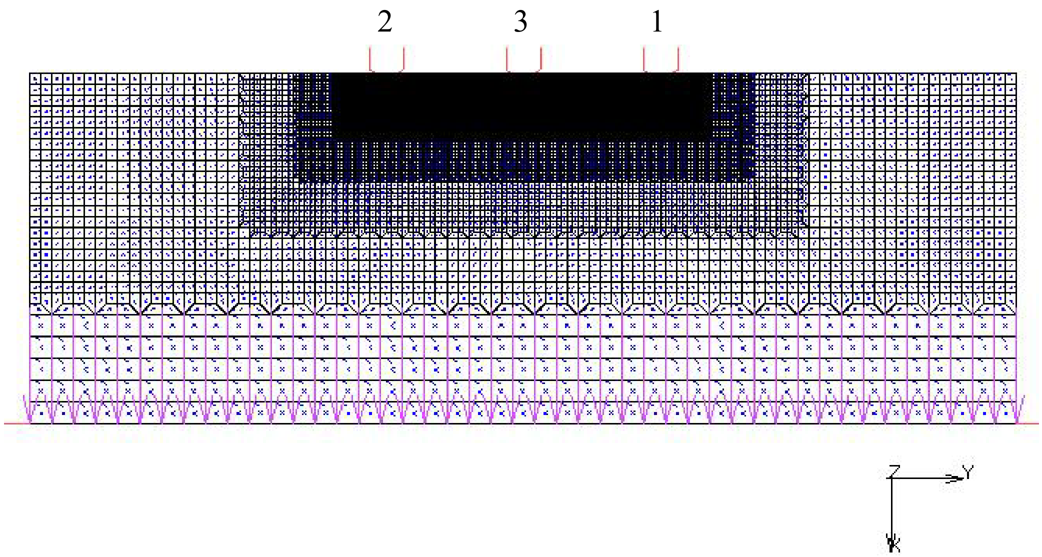


**Figure 3.22** Mesh used to model triple indentation

As boundary conditions, x displacement of the nodes at the bottom of specimen where it rests are set to 0, so that they do not move in x direction which is also the direction of motion of the indenter.

For material properties, since flow curve of Al2014, which is the material used in the experiments, is not available at room temperature, a different flow data for AlMgSi1 is used. Ludwik's formula for flow curve is applied and data are supplied to the commercial finite element program MSC.SuperForm by a piecewise linear curve. Ludwik's expression for cold flow curves has the form $\sigma_f = C\bar{\varepsilon}^n$ where detailed material properties can be found in Appendix B.

Three sequential loadcases are used and the process is modeled as if there were three indenters indenting the specimen one after another.

### 3.4.1.1.2 Simulation Results

The simulation results revealed the same behavior of force-displacement curves for this indentation as in the experiments. The experimental force-displacement curves are given in Section 6.4.3.2 , Figure 6.21. Figure 3.23 gives force-displacement curves obtained numerically by finite element method.

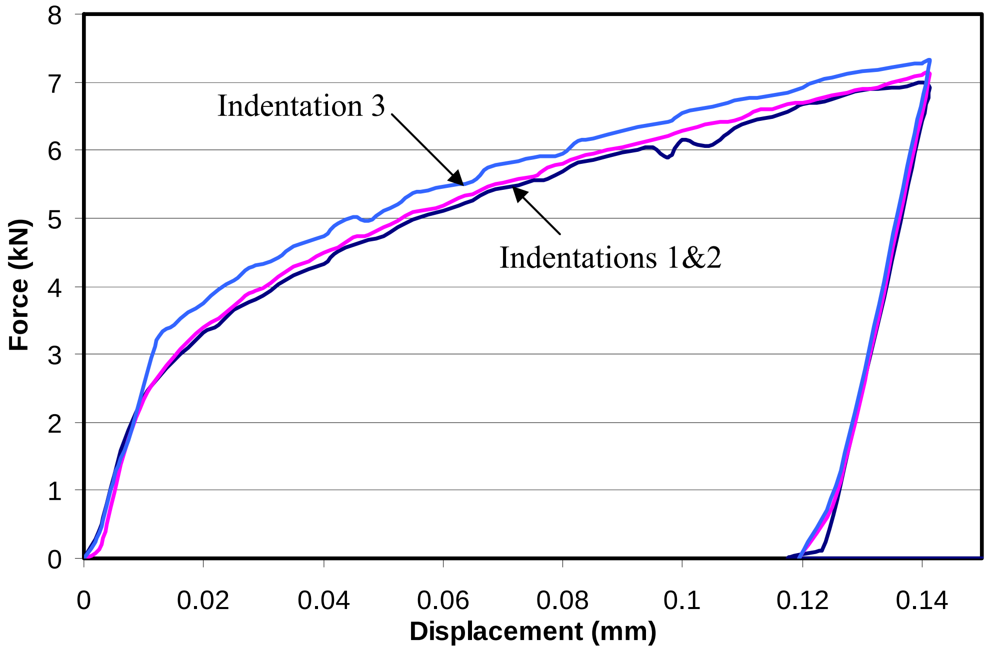


**Figure 3.23** Force-displacement curves by simulation (*d*/*c*=3)

One reason of higher forces for the third indentation could be the strain-hardening of the material just below the indenter at third position caused by the previous two deformations. Figure 3.24 shows plastic strain distributions, the left figure shows plastic strain distributions after first two indentations loading and unloading of both are complete. The right figure shows plastic strain distribution when the third indentation is at the maximum depth of indentation just before unloading starts.

Referring to the left figure of Figure 3.24 it is seen that even for a very small plastic strain range, the color bands do not extend to the third indentation part. From the right figure it is seen that plastic deformation zones have very little contact and it is at the end of the third indentation. This proves that strain hardening of the material is not the reason of higher forces.

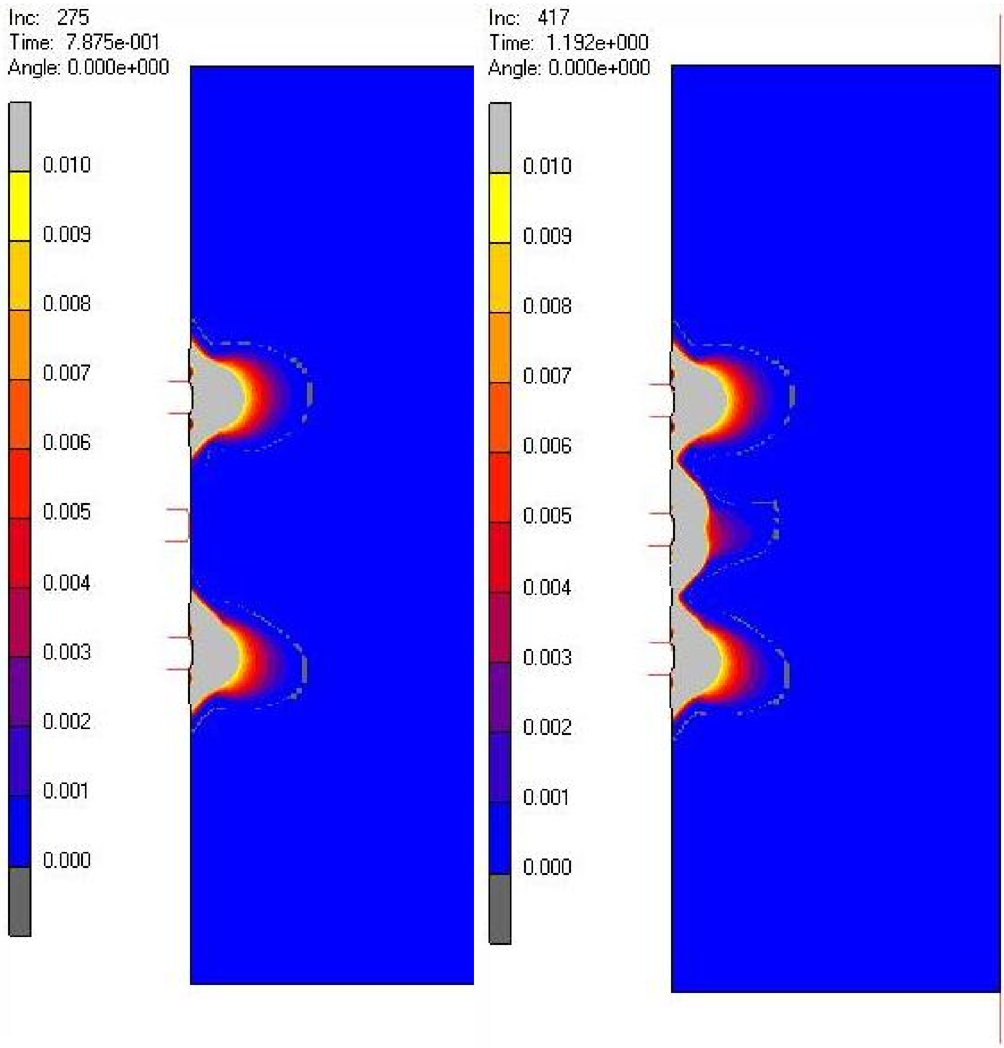


**Figure 3.24** Equivalent plastic strain distributions ($d/c$=3)

The equivalent stresses at the end of each indentation period covering loading and unloading are seen in Figure 3.25. When unloading of first indentation is completed, the equivalent residual stress distribution in the material is as seen in left figure of Figure 3.25. The stresses are in the range up to 120-140 MPa. Since the next indentation is the second indentation, lower stresses do not affect the force-displacement curve of the second indentation as much as the third one.

The middle figure of Figure 3.25 shows the equivalent residual stress state after the unloading of the second indentation is completed. In this case, the stresses remaining at the region of last indentation are considerably high, such that they affect the forces to start yielding. This causes the force-displacement curve for the third indentation to be different from the other two.

The effect of residual stresses will be cleared and explained analytically in Section 3.4.1.1.3.

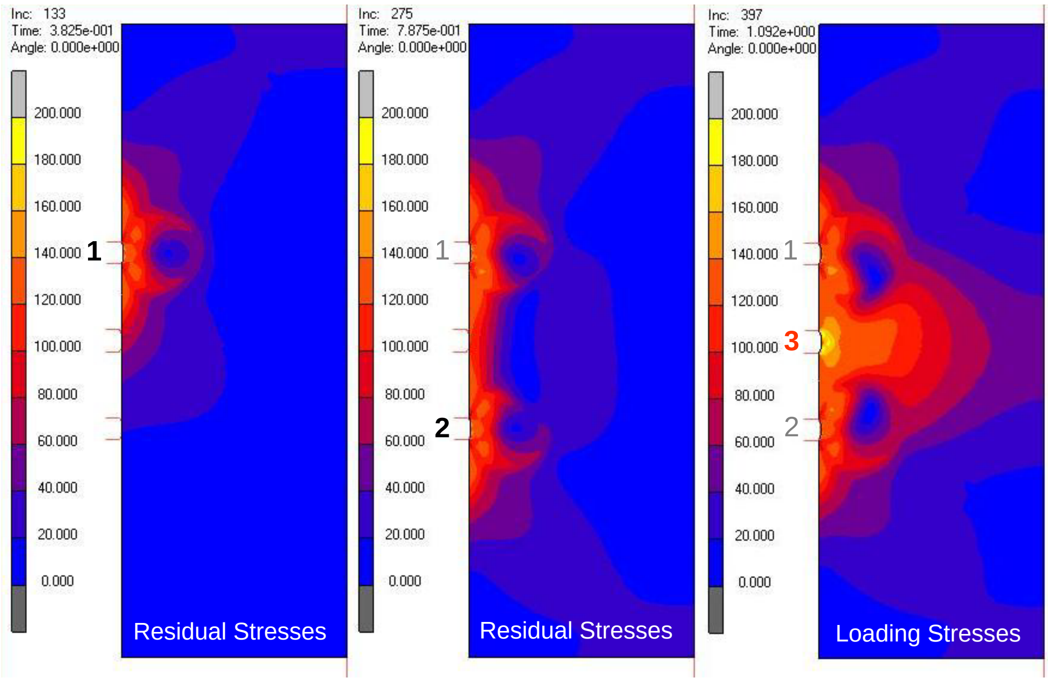


**Figure 3.25** Equivalent stress distributions after each indentation

The finite element analyses of multiple sequential indentations continued with studies of changing distances between indentations. The problem is modeled as in Figure 3.21 and finite element analysis models and mesh topologies can be seen in Appendix C.

At the end of analyses to determine the minimum distance between indenters in such an application, Figure 3.26 is obtained which shows force-displacement curves of indentations 1-2 and 3. As explained before, referring to results of triple indentation study with *d*/*c* = 3, the first two indentations could be simulated simultaneously since the first two have negligible effect on force-displacement curves of each other.

The pink colored force-displacement curves are the force-displacement curves of the first two indentations and they are very close to each other for all distances between indenters. On the other hand, force-displacement curves with other colors belong to the third indentation for different spacing between indenters. Among those curves, the red one, which is for *d*/*c* = 7, is very close to the curves of indentations 1 and 2. Looking at the force-displacement curves, it can be deduced that the minimum distance for each indentation to act independently is more than 7 times the width of the indenter. In other words, *d*/*c* > 7 is the requirement to get independent force-displacement curves as a result of triple indentations performed sequentially.

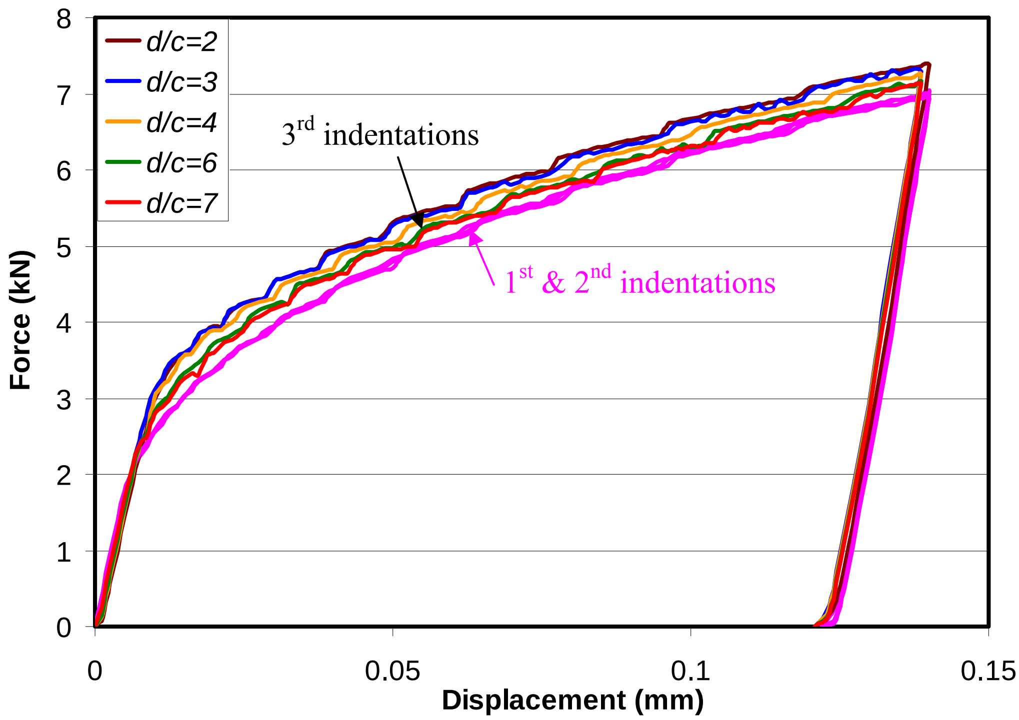


**Figure 3.26** Force-displacement curves for various *d*/*c*

A closer look to first and second indentations for all different distance indentations are given in Figure 3.27. In a larger scale as in Figure 3.26 they look to be coincident but the difference between the curves can be observed in a smaller scale as in Figure 3.27. The displacement range is 0.032-0.038 mm in this graph.

The forces are slightly higher for smaller distance between indentations and smaller for larger distances. The only exception is the curve of 1st & 2nd indentations for *d*/*c* = 7. The reason is not investigated, but the indenters get closer to the edge as the distance increases. It may be the reason of this unexpected behavior.

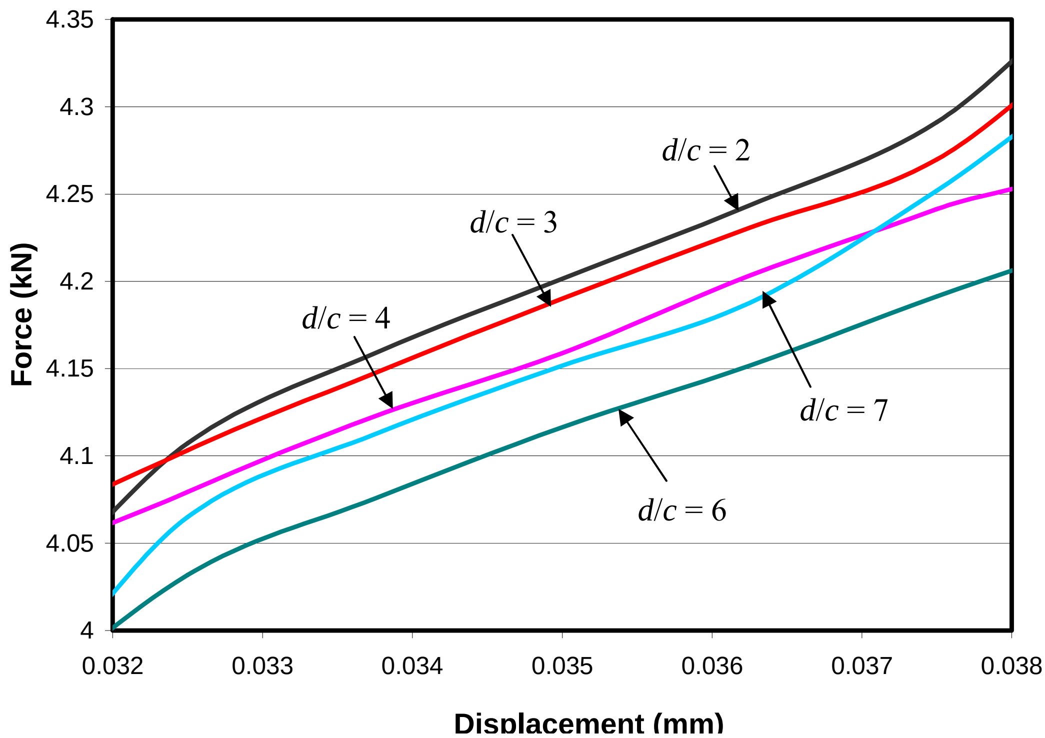


**Figure 3.27** Force-displacement curves of 1st & 2nd indentations

### 3.4.1.1.3 Analytical Identification of the Problem

In the previous section, from finite element analysis results it is seen that there is a stress distribution beneath the indenter just before third indentation starts. In this section, it is aimed to find an explanation to how the residual stresses affect the forces.

*Residual Stresses*

Such stresses as in this case occurring in a body when it is free from external forces are called residual stresses [43]. The reason for residual stresses is found to be inhomogeneous plastic deformation [44].

Residual stresses are defined as elastic stresses whose maximum value can reach the yield stress of the material. They also have to be in static equilibrium, that is the total force and total moment of forces on any plane must be zero.

*Determining the Stress State*

First of all, the residual stress state beneath the third indenter is recorded. The loading stress state can be obtained from the first indentation when there is no residual stress state around. These stresses are recorded at three points a, b and c. Figure 3.28 gives the total equivalent plastic strain distribution beneath the indenter after loading and unloading of the first indentation are completed. In this figure, locations of the points a, b and c are seen. The residual stresses are recorded before third indentation in undeformed state and the loading stresses are recorded at $2.6 \cdot 10^{-2}$ mm displacement of indenter during loading of first indenter. The stress component corresponding to an element is calculated by taking the arithmetic mean of the stresses at its four nodes. Tables 3.3, 3.4 and 3.5 show these values at locations a, b and c, respectively.

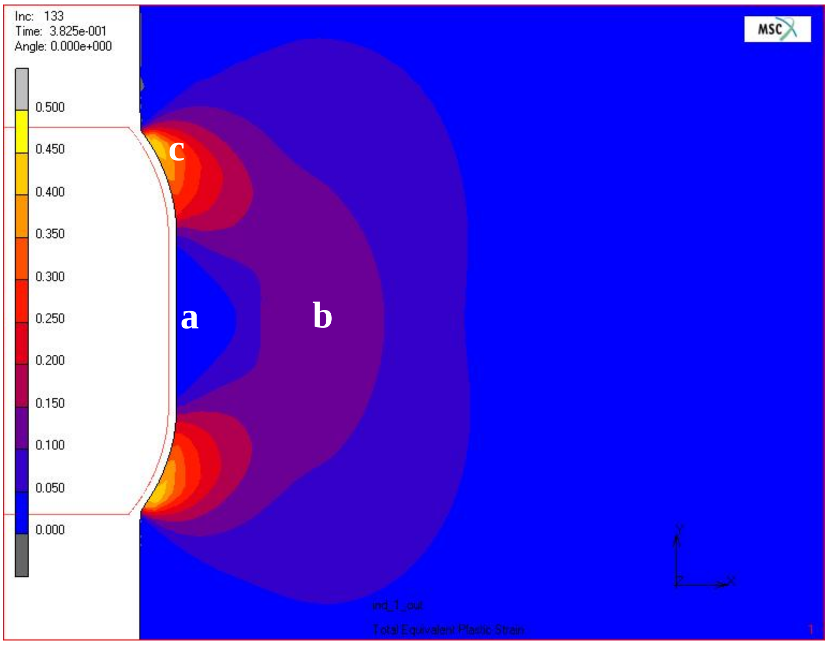


**Figure 3.28** Total equivalent plastic strain after first indentation

**Table 3.3** Stress state at location a

Loading stresses below indenter 1:

| node ID's | | $\sigma_{11}$ | $\sigma_{22}$ | $\sigma_{33}$ | $\sigma_{12}$ | $\sigma_{23}$ | $\sigma_{31}$ |
|---|---|---|---|---|---|---|---|
| 2244 | Node 1 | -362.83 | -241.64 | -225.19 | 3.10 | 0 | 0 |
| 2245 | Node 2 | -362.72 | -240.48 | -225.81 | 3.01 | 0 | 0 |
| 2242 | Node 3 | -363.69 | -241.96 | -226.76 | 5.25 | 0 | 0 |
| 2241 | Node 4 | -362.54 | -237.99 | -227.68 | 5.77 | 0 | 0 |
| | average: | **-362.95** | **-240.52** | **-226.36** | **4.28** | **0** | **0** |

Residual stresses below indenter 3:

| node ID's | | $\sigma_{11}$ | $\sigma_{22}$ | $\sigma_{33}$ | $\sigma_{12}$ | $\sigma_{23}$ | $\sigma_{31}$ |
|---|---|---|---|---|---|---|---|
| 19309 | Node 1 | 0.15 | -137.59 | -41.23 | 0.076 | 0 | 0 |
| 19310 | Node 2 | -0.006 | -136.99 | -41.10 | 0.14 | 0 | 0 |
| 11648 | Node 3 | -0.006 | -137.10 | -41.13 | 0.15 | 0 | 0 |
| 11642 | Node 4 | 0.15 | -137.71 | -41.27 | 0.08 | 0 | 0 |
| | average: | **0.074** | **-137.35** | **-41.18** | **0.11** | **0** | **0** |

| | | | | | | |
|---|---|---|---|---|---|---|
| Sum of stresses: | -362.87 | -377.86 | -267.54 | 4.40 | 0 | 0 |

Equivalent Von Mises Stress: $\boxed{\mathbf{103.92}}$ MPa

**Table 3.4** Stress state at location b

Loading stresses below indenter 1:

| node ID's | | $\sigma_{11}$ | $\sigma_{22}$ | $\sigma_{33}$ | $\sigma_{12}$ | $\sigma_{23}$ | $\sigma_{31}$ |
|---|---|---|---|---|---|---|---|
| 2324 | Node 1 | -328.31 | -169.40 | -246.43 | -2.93 | 0 | 0 |
| 2335 | Node 2 | -321.37 | -162.79 | -239.56 | -3.05 | 0 | 0 |
| 2333 | Node 3 | -320.00 | -162.67 | -238.85 | -10.25 | 0 | 0 |
| 2322 | Node 4 | -326.90 | -169.20 | -245.66 | -10.07 | 0 | 0 |
| | average: | **-324.15** | **-166.01** | **-242.62** | **-6.57** | **0** | **0** |

Residual stresses below indenter 3:

| node ID's | | $\sigma_{11}$ | $\sigma_{22}$ | $\sigma_{33}$ | $\sigma_{12}$ | $\sigma_{23}$ | $\sigma_{31}$ |
|---|---|---|---|---|---|---|---|
| 19329 | Node 1 | -1.30 | -117.79 | -35.73 | 2.04 | 0 | 0 |
| 19330 | Node 2 | -1.42 | -116.68 | -35.43 | 2.14 | 0 | 0 |
| 12113 | Node 3 | -1.40 | -116.77 | -35.45 | 2.26 | 0 | 0 |
| 12049 | Node 4 | -1.29 | -117.88 | -35.75 | 2.16 | 0 | 0 |
| | average: | **-1.36** | **-117.28** | **-35.59** | **2.15** | **0** | **0** |

| | | | | | | |
|---|---|---|---|---|---|---|
| Sum of stresses: | -325.50 | -283.30 | -278.22 | -4.42 | 0 | 0 |

Equivalent Von Mises Stress: **45.61** MPa

**Table 3.5** Stress state at location c

Loading stresses below indenter 1:

| node ID's | | $\sigma_{11}$ | $\sigma_{22}$ | $\sigma_{33}$ | $\sigma_{12}$ | $\sigma_{23}$ | $\sigma_{31}$ |
|---|---|---|---|---|---|---|---|
| 1567 | Node 1 | -402.94 | -200.33 | -299.27 | 23.42 | 0 | 0 |
| 1568 | Node 2 | -401.95 | -209.06 | -303.29 | 7.02 | 0 | 0 |
| 1561 | Node 3 | -374.24 | -189.31 | -280.75 | -16.85 | 0 | 0 |
| 1560 | Node 4 | -396.26 | -202.85 | -298.03 | 30.96 | 0 | 0 |
| | average: | **-393.85** | **-200.39** | **-295.34** | **11.14** | **0** | **0** |

Residual stresses below indenter 3:

| node ID's | | $\sigma_{11}$ | $\sigma_{22}$ | $\sigma_{33}$ | $\sigma_{12}$ | $\sigma_{23}$ | $\sigma_{31}$ |
|---|---|---|---|---|---|---|---|
| 7538 | Node 1 | 0.16 | -139.71 | -41.86 | 0.13 | 0 | 0 |
| 7544 | Node 2 | -0.005 | -139.07 | -41.72 | 0.25 | 0 | 0 |
| 7502 | Node 3 | -0.005 | -139.28 | -41.79 | 0.26 | 0 | 0 |
| 7496 | Node 4 | 0.16 | -139.92 | -41.93 | 0.14 | 0 | 0 |
| | average: | **0.08** | **-139.50** | **-41.82** | **0.19** | **0** | **0** |

| | | | | | | |
|---|---|---|---|---|---|---|
| Sum of stresses: | -393.77 | -339.88 | -337.16 | 11.33 | 0 | 0 |

Equivalent Von Mises Stress: **58.68** MPa

Equivalent von Mises stress is calculated as given by Eqn. (3.1) [45].

$$\bar{\sigma}_{vM} = \sqrt{\frac{1}{2}\left[(\sigma_{11}-\sigma_{22})^2+(\sigma_{22}-\sigma_{33})^2+(\sigma_{33}-\sigma_{11})^2+6\left(\tau_{12}^2+\tau_{23}^2+\tau_{13}^2\right)\right]} \qquad (3.1)$$

The equivalent von Mises stresses of the residual stress state at locations a, b and c are calculated from Eqn. (3.1) referring to the tables. The results are given by Eqn. (3.2).

$$\begin{aligned}(\sigma_{vM}^{R})_a &= 122 \text{ MPa}\\ (\sigma_{vM}^{R})_b &= 103 \text{ MPa}\\ (\sigma_{vM}^{R})_c &= 124 \text{ MPa}\end{aligned} \qquad (3.2)$$

where $\sigma_{vM}^{R}$ denotes equivalent von Mises residual stresses.

The stress state at these points is calculated by taking the average of the four nodes of an element and then treating them as the stress components at those locations. The above values also show that the residual stresses are less than the yield stress. The initial yield stress is 130 MPa for this material and there is no plastic deformation yet.

On the other hand, the loading equivalent von Mises stresses at $2.6 \cdot 10^{-2}$ mm displacement of indenter for the first indentation are calculated as in Eqn. (3.3).

$$\begin{aligned}(\sigma_{vM}^{L})_a &= 130 \text{ MPa}\\ (\sigma_{vM}^{L})_b &= 137 \text{ MPa}\\ (\sigma_{vM}^{L})_c &= 168 \text{ MPa}\end{aligned} \qquad (3.3)$$

where $\sigma_{vM}^{L}$ denotes equivalent von Mises loading stresses. Then, the theoretical stress state during loading at third indentation region is calculated by adding the loading stress state to the residual stress state as given in Eqn. (3.4).

$$\begin{bmatrix} \sigma_{11} & \sigma_{12} & \sigma_{13} \\ \sigma_{21} & \sigma_{22} & \sigma_{23} \\ \sigma_{31} & \sigma_{32} & \sigma_{33} \end{bmatrix}^{L+R} = \begin{bmatrix} \sigma_{11} & \sigma_{12} & \sigma_{13} \\ \sigma_{21} & \sigma_{22} & \sigma_{23} \\ \sigma_{31} & \sigma_{32} & \sigma_{33} \end{bmatrix}^{L} + \begin{bmatrix} \sigma_{11} & \sigma_{12} & \sigma_{13} \\ \sigma_{21} & \sigma_{22} & \sigma_{23} \\ \sigma_{31} & \sigma_{32} & \sigma_{33} \end{bmatrix}^{R} \tag{3.4}$$

The equivalent von Mises stresses for the third indentation region are obtained as given in Eqn. (3.5) using Eqn.s (3.4) and (3.1).

$$\begin{aligned} (\sigma_{vM}^{L+R})_a &= 104 \text{ MPa} \\ (\sigma_{vM}^{L+R})_b &= 46 \text{ MPa} \\ (\sigma_{vM}^{L+R})_c &= 59 \text{ MPa} \end{aligned} \tag{3.5}$$

where $\sigma_{vM}^{L+R}$ denotes equivalent von Mises of loading stresses added to residual stresses.

From Eqn.s (3.3) and (3.4) it can be deduced that although for an indentation without residual stresses yielding has started, with residual stresses higher forces are needed to reach the yield stress of the material.

The simulation and calculations identify the reason why the force-displacement curves for these three indentations vary with respect to each other. It has also added another perspective to the indentation process which was not considered before.

### 3.4.1.2 Multiple-Simultaneous Indentation

Regarding the similarity between Meguid *et al.*'s study on co-indentation [20, 21] and the triple indentation work in this thesis, it was necessary also to see the case for co-indentation which is named as multiple-simultaneous indentation here.

The difference between the two studies is that in the sequential indentations an indentation is applied at the middle of two previous indentations. The distance between indentations is to be found in order that the force-displacement curves, in fact the deformation zones underneath the indenters, are not affected by others. In this study, indentations are performed in a sequence, not at the same time but on the same specimen and there is only one indenter.

In the co-indentation case, two indentations are applied on the same specimen, at the same time. There are two indenters. Different from the previously explained case, there are no residual stresses on the specimen; instead the deformation zones develop at the same time.

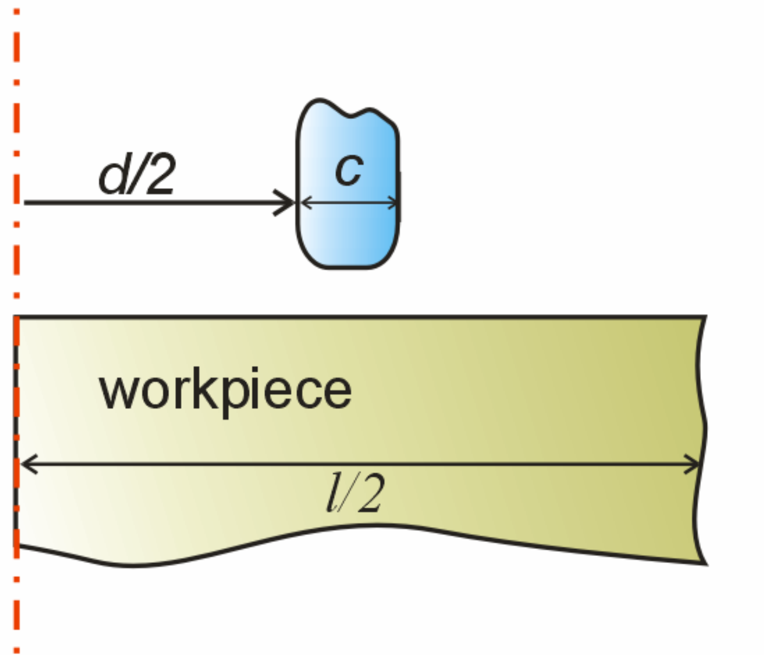


**Figure 3.29** Model for multiple-simultaneous indentation (co-indentation)

In this study, a two-dimensional finite element model with a symmetry line is used. Figure 3.29 shows a representation of the model.

The force-displacement curves obtained for different $d/c$ are plotted and compared to check the minimum distance between the indenters, so that they behave independently. The resulting force-displacement curves are seen in Figure 3.30.

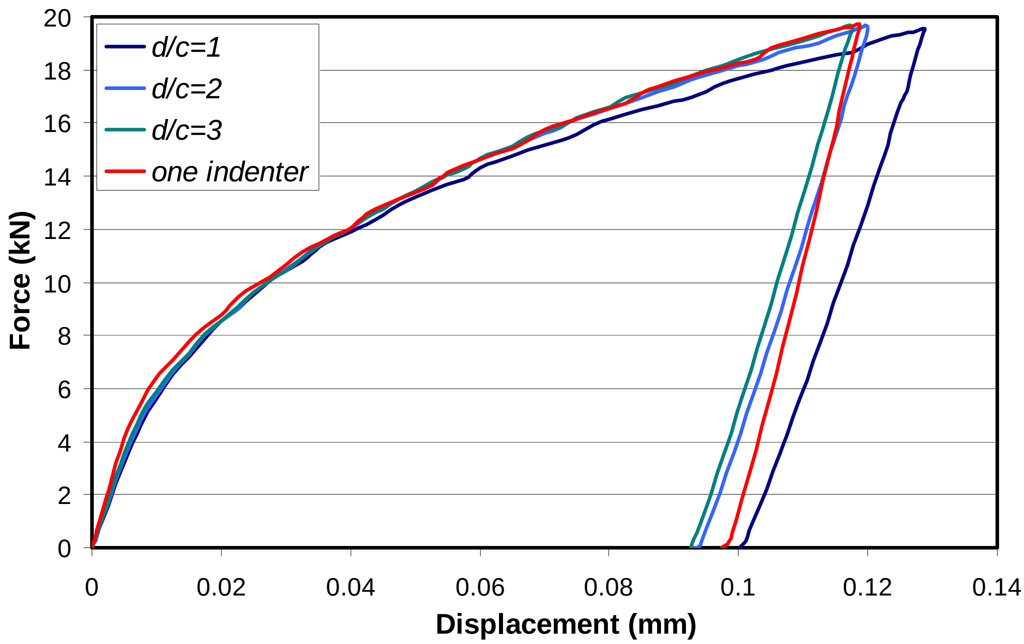


**Figure 3.30** Force-displacement curves of multiple-simultaneous indentations

The simulation results with different distance ratios $d/c$ are compared with the force-displacement curves obtained from a single indentation applied in the middle of the specimen. As seen from Figure 3.30, when $d/c=1$ lower forces are required. Since indenters are too close to each other their deformation zones interact with each other. The force-displacement curve of indentation when $d/c=2$ is closer to the force-displacement curve obtained by a single indenter. For $d/c=3$ and one indenter the curves are coincident. So, it can be concluded from these curves that for $d/c \geq 3$ there is no interaction between the two deformation regions.

Figure 3.31 shows total equivalent plastic strain figures for different spacing of indenters. As seen in the figure on the upper left corner, for $d/c=1$ the plastic deformation zone is in contact with the symmetric one. For the case where the total equivalent plastic strain figure beneath the indenter is similar to the one beneath the indenter where only one indentation is applied, it can be said that plastic zone is not affected. It is also worth noting that the total equivalent plastic strain bands for one indenter case is symmetric, whereas this symmetry is too much distorted for $d/c = 1$, but very little distortion is observed for $d/c = 3$.

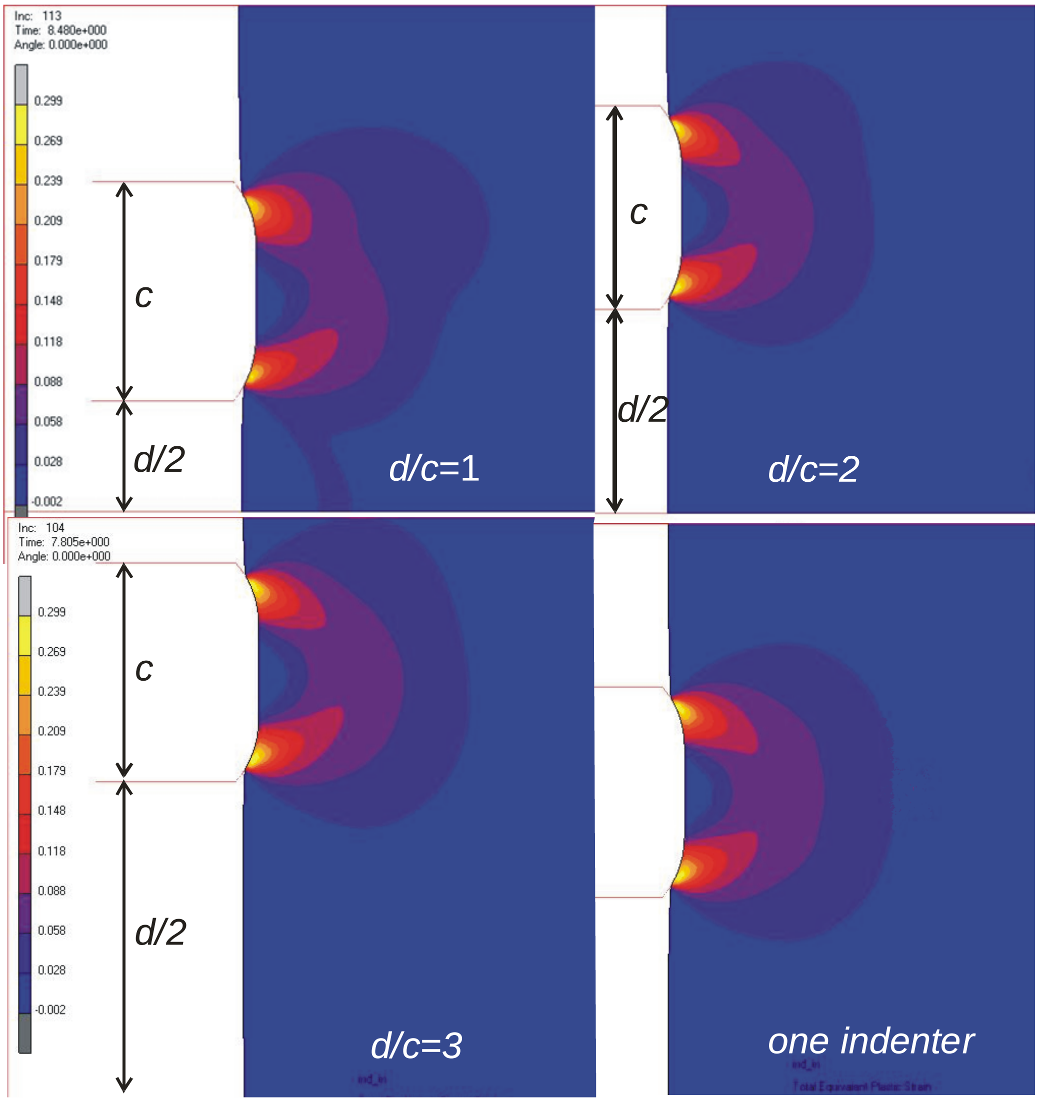


**Figure 3.31** Total equivalent plastic strain when indenter is at maximum displacement from the surface

### 3.4.2 Analysis of Clamping of Specimen

In order to fix the specimens during indentation, the reference plate is screwed and the specimen is stuck between the reference plate and the anvil as in Figure

3.32. This application, when the plate is screwed with higher forces, increases the repeatability for the experiments. But it is to be investigated if this force affects the force-displacement curves as well.

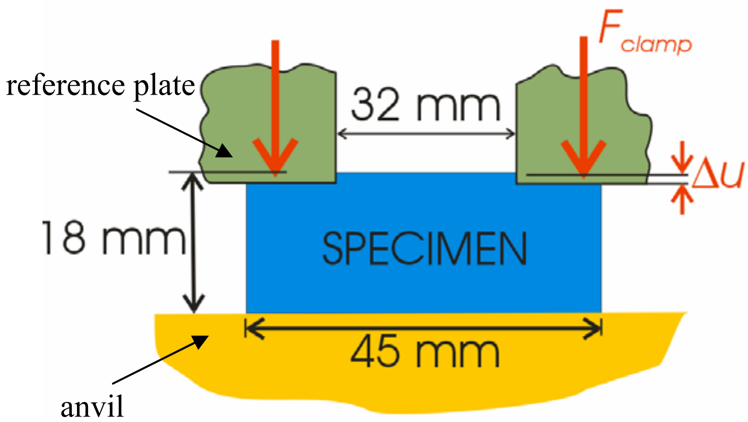


**Figure 3.32** Clamping of Specimen

### 3.4.2.1 Finite Element Model and Results

In order to see if the clamping force affects the force-displacement curves finite element analyses are performed. In the two-dimensional (plane strain) model the reference plate had a certain displacement which is called Δu here. Figure 3.33 shows force-displacement curves for aluminum alloy for three cases, free of clamping, clamping with 10 μm displacements of the reference plate and for clamping with 50 μm displacement of the reference plate. These curves show that there is an effect on the force-displacement curves with changing squeezing of the reference table.

The second question is how much force is applied on the specimen with these specified displacements. Figure 3.34 shows forces on the reference plate for two materials C15 and AlMgSi1.

As expected, for steel these forces are higher and for aluminum lower. The linear parts at the ends of the curves where displacement is constant show change of force during indentation.

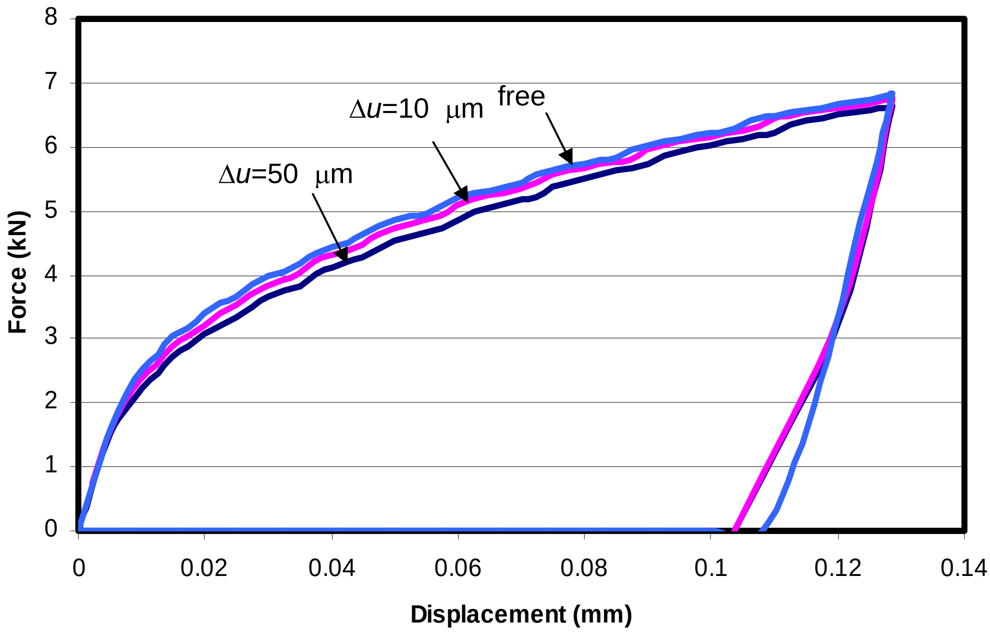


**Figure 3.33** Force-displacement curves for different Δu

(Material: AlMgSi1, $\mu$=0.1)

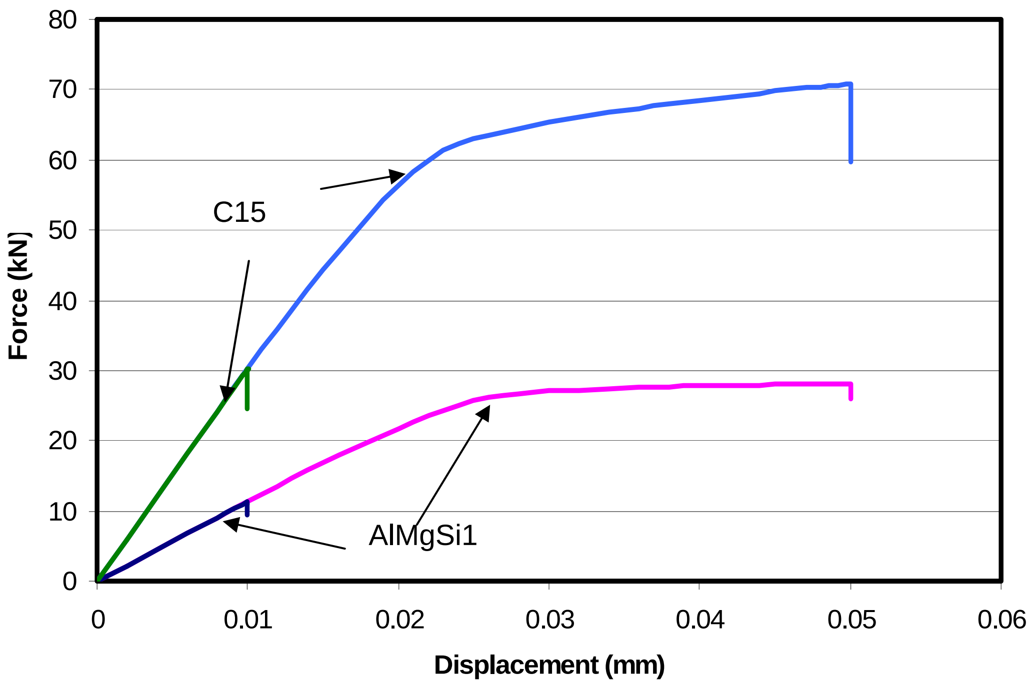


**Figure 3.34** Forces on reference plate for different Δu

(Material: AlMgSi1, C15, $\mu$=0.1)

### 3.4.2.2 Comparison of Results with Analytical Solution

In Figure 3.34 the forces on the reference plate for the given displacements are seen. In order to be able to compare these results with the real case, the force applied on the plate is to be calculated, at least approximately.

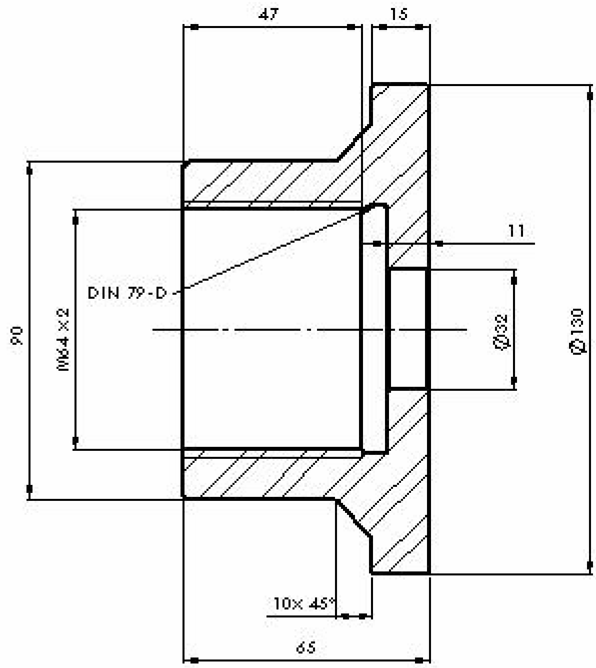


**Figure 3.35** Cross-section of the reference plate with dimensions

Assuming that the manually applied force to fix the reference plate is a 250 N force couple where the distance between the force components is 150 mm, the torque can be calculated as $T = 250 \cdot 150 \cdot 10^{-3} = 37.5$ N.m.

The formula for tightening a screw or bolt is given as follows in [46].

$$T = \frac{Fd_m}{2}\left(\frac{l + \pi\mu d_m}{\pi d_m - \mu l}\right) \tag{3.6}$$

The mean diameter $d_m$ is 64 mm and lead $l$ is 2 mm for the threads used to tighten the reference plate (Figure 3.35). The coefficient of friction, which depends upon the surface smoothness, accuracy and degree of lubrication, can be taken as 0.15 [49]. Using these parameters, the axial compressive force F is calculated by using Eqn. 3.6 and it is obtained as 7316 N. The Eqn. 3.6 is very conservative since it neglects the friction on the collar and the thread angle. If they have been included in the calculation, the axial compressive force is even less than this value.

Comparing the axial force with the forces in Figure 3.34, it is seen that the 50 μm displacement of the reference plate, which causes plastic deformation of the specimen, is impossible to achieve manually. With this amount of applied force it is still impossible to reach 10 μm displacement even for aluminum specimen.

The conclusion for this analysis is that the clamping forces do not affect force-displacement curves of indentation.

# CHAPTER 4

# COMPRESSION TEST ANALYSIS WITH FEM

## 4.1 Introduction

In this chapter, finite element analyses of compression tests will be presented. In order to verify indentation experiments and check anisotropy of the material, compression tests are done on the available setup. The possible errors and effects in a compression test are considered and simulated by the commercial finite element analysis program MSC.SuperForm. Some of these analyses are done in order to have previous knowledge about the process and some are done after the compression tests to find reasons of unexpected results.

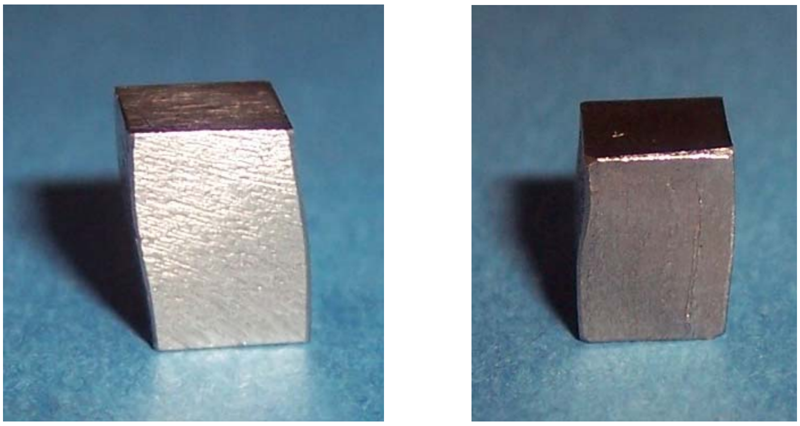

**Figure 4.1** Compression specimens after test

Figure 4.1 gives two extreme examples of final geometries of specimens. They look as if they have experienced buckling and torsion. Figure 4.2 gives the true stress-true strain curves obtained form these compression tests. The stresses start to decrease after some strain. The reason for decrease of stresses needs to be investigated.

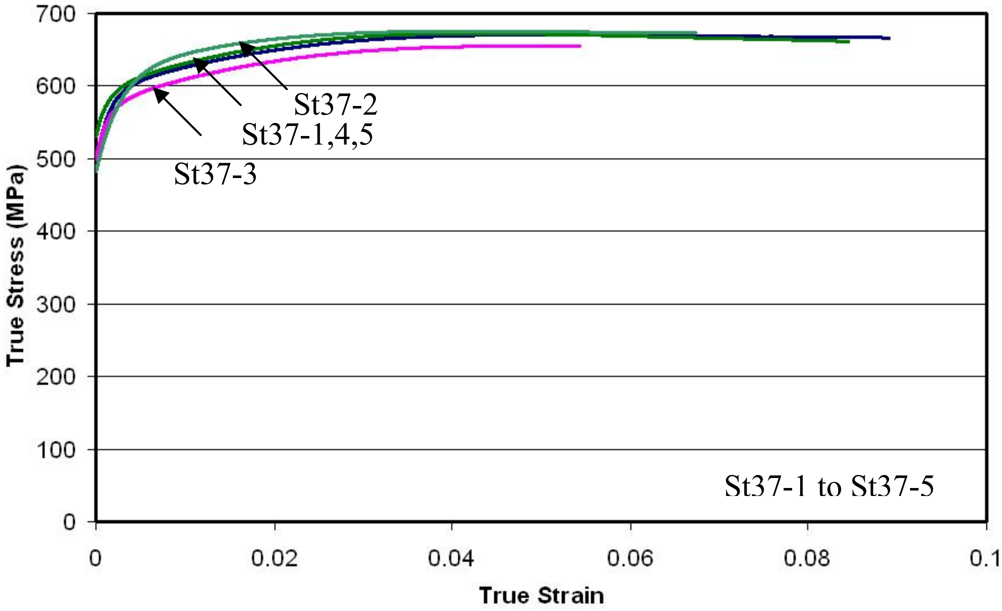


**Figure 4.2** Compression test results of prismatic specimen of St37

The possible effects on the results could be the geometry, the production processes of the specimens, friction at the contact surfaces or a misalignment of upper and lower surfaces of the press where the compression test is done.

This chapter includes finite element modeling of compression tests and effect of specimen geometry on true stress- true strain data. Effect of height of specimen, effect of friction coefficient and effect of tilting of the upper punch are analyzed.

## 4.2 Finite Element Models

The experimental study of compression tests was to be done on St37 which was in the form of sheet metal. Since it would be more practical and easy to produce prismatic specimens for compression, first finite element simulation was done to check the effect of specimen geometry. Analysis for cylindrical specimen is done using an axisymmetric model. The prismatic specimen is modeled in three dimensions.

For analysis of compression of cylindrical specimen, an axisymmetric model which is shown in Figure 4.3 is used. The model is composed of 384 four-node quadrilateral elements. C15 is selected as the material whose material properties can be seen in Appendix B. No boundary conditions are applied; the specimen rests on the base die. The coefficient of Coulomb friction between base die and the specimen is 0.1 as well as the Coulomb friction coefficient between the punch and the specimen. The dies are defined as rigid, velocity controlled bodies. Base die has zero velocity whereas the punch moves with 1 mm/min velocity towards the specimen.

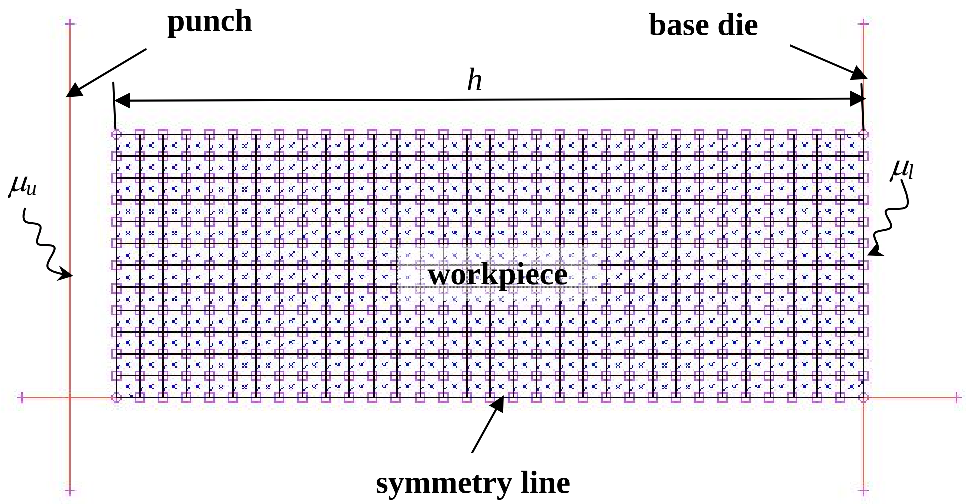


**Figure 4.3** Finite element model of axisymmetric compression

Figure 4.4 shows a sketch of the prismatic specimen with height *h* and width *b*. The prismatic compression is modeled in three dimensions with two symmetry planes. One more symmetry plane could be added but this would prevent the study of two different friction coefficients on two die-workpiece contact surfaces.

The three-dimensional finite element model in Figure 4.5 contains 3200 elements which are four-node hexahedral elements. The Coulomb coefficient of friction between the upper and lower dies and the workpiece are assigned different values for different analyses. Throughout this chapter the coefficient of Coulomb friction between the moving upper punch and the workpiece will be called $\mu_u$ and the coefficient of Coulomb friction between the fixed base die and the workpiece will be called $\mu_l$. The dies are rigid as for the axisymmetric model. Material of the workpiece is C15 as used in all compression analyses in this chapter.

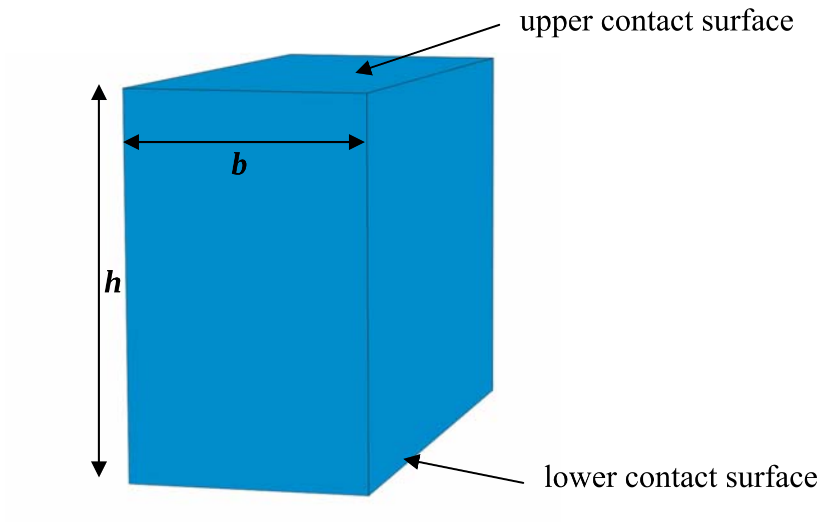


**Figure 4.4** Sketch of prismatic compression specimen

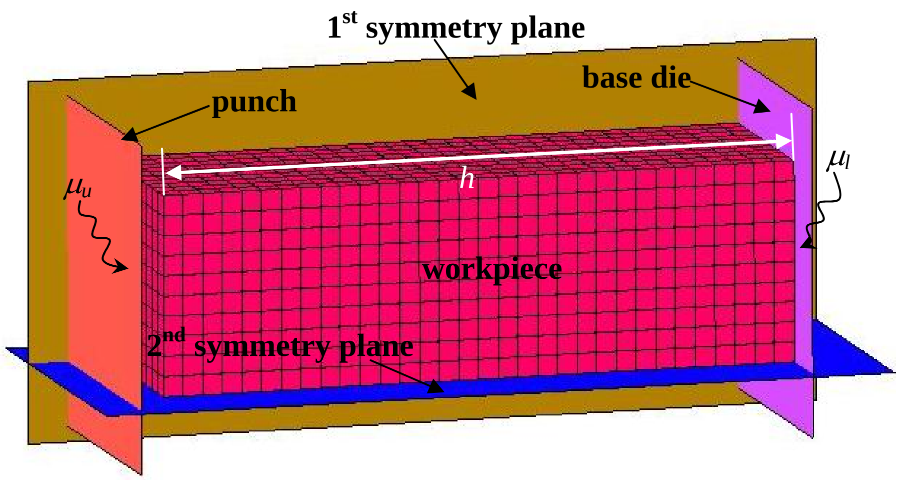


**Figure 4.5** Finite element model of three-dimensional compression

Since, the available bars which will be used for compression tests had 5x5 $mm^2$ cross-sections and 8 mm height, the finite element model is also constructed accordingly. The workpiece in Figure 4.4 has 8 mm height, and 2.5 x 2.5 $mm^2$ cross-sectional area since one quarter of the cross-section of the specimen is modeled.

## 4.3 Effect of Specimen Geometry

It is common to use cylindrical specimens for flow curve determination by compression. Since it is more practical to produce prismatic specimens from a rolled plate, it is needed to analyze and compare the compression test results of a cylindrical and a prismatic specimen.

At first, two finite element simulations are done to investigate if there is a difference in flow curves obtained by a cylindrical and a square prismatic specimen. This study was necessary to prove that the results do not differ for these different specimen geometries. The cylindrical specimen is modeled as axisymmetric (Figure 4.3) and the square prismatic specimen is modeled in three dimensions with two planes of symmetry as in Figure 4.5.

In order to have the same surface area, the radius for axisymmetric model is calculated equating the circular cross-sectional area of the cylindrical specimen to 25 $mm^2$. Then, the radius for the axisymmetric model is found as 2.821 mm.

The force-displacement data obtained at the end of each simulation are used to calculate true stress and true strain values. The surface area at any displacement of the upper punch is calculated making use of the volume constancy. Let $F$ denote the force, $h$ denote the height of specimen at a given displacement of the indenter, $A$ denote the cross-sectional area and $V_o$ denote initial volume of the specimen. $h$ is calculated by subtracting the amount of displacement from the initial height. Then, true stress $\sigma_t$ is calculated by:

$$\sigma_t = \frac{F}{A} = \frac{F}{V_o / h} \tag{4.1}$$

$$\sigma_t = \frac{F \cdot h}{V_o} \tag{4.2}$$

Eqn. (4.3) is used to calculate true total strain of the compression specimen where $h_o$ denotes initial height of the specimen.

$$\varepsilon_t = \ln \frac{h_o}{h} \tag{4.3}$$

The true stress-true total strain plot of data obtained from Eqn.s (4.2) and (4.3) for cylindrical and prismatic specimens are seen in Figure 4.6.

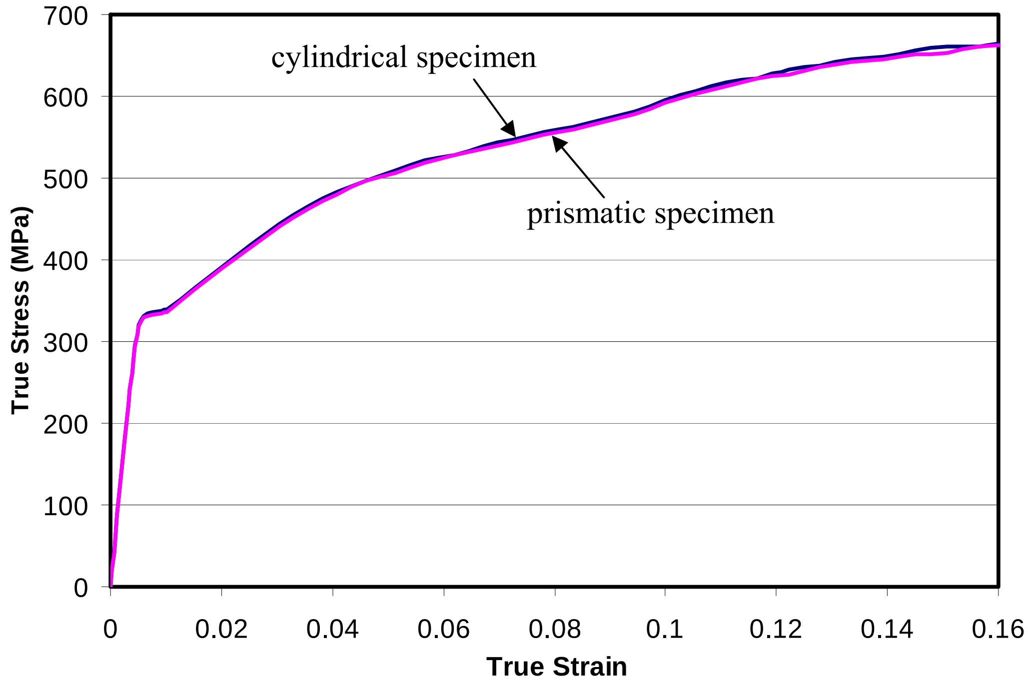


**Figure 4.6** True stress-true total strain curves of cylindrical and prismatic specimens

(Material: C15, $\mu_u = 0.1$, $\mu_l = 0.1$, $h = 8$ mm)

The true stress values for both of the specimens for a given true strain are very close to each other. The very small difference might be a result of round off error while calculating the radius of the cylindrical specimen which affects the contact area.

According to this analysis and its results, compression tests done using a prismatic specimen reveal same flow curve as with a cylindrical specimen under ideal modeling conditions. With this knowledge, experiments are done using the prismatic specimens.

## 4.4 Effect of Specimen Height

Finite element analyses are done to analyze the effect of height of specimen on true stress-true strain curves. In the analyses, specimens with 4 mm and 5 mm height are modeled in addition to 8 mm specimen height.

The model given in Figure 4.5 is used but height is changed for each simulation. Finite element modeling conditions are given in Table 4.1.

When the force-displacement curves of these analyses are used to obtain true stress and true total strain values for compression, the curves in Figure 4.7 are obtained with assumptions of volume constancy and no barreling. The Eqn.s (4.2) and (4.3) are used to calculate true stress and true total strain data.

Figure 4.7 shows that true total strain increases when height decreases. The most probable reason for that are the deformation zones. Starting from the upper and lower surfaces deformation zones develop to the core of the specimen. When the specimen higher, these zones do not interfere with each other. On the other hand, when the specimen height is smaller they interfere with each other causing the stresses to increase.

**Table 4.1** Modeling conditions for height comparison of compression tests

| | $h$ = 8 mm | $h$ = 5 mm | $h$ = 4 mm |
|---|---|---|---|
| Number of elements | 3200 | 2000 | 1600 |
| Element type | 8 node hexahedral | | |
| Material | C15 | | |
| Total loadcase time (sec) | 120 | | |
| Number of steps | 800 | | |
| Punch velocity (mm/sec) | 0.016667 | | |
| $\mu_u$ , $\mu_l$ | 0.1 | | |
| Relative force tolerance (δ) | 0.01 | | |
| Termination | Maximum force, 5000 N | | |

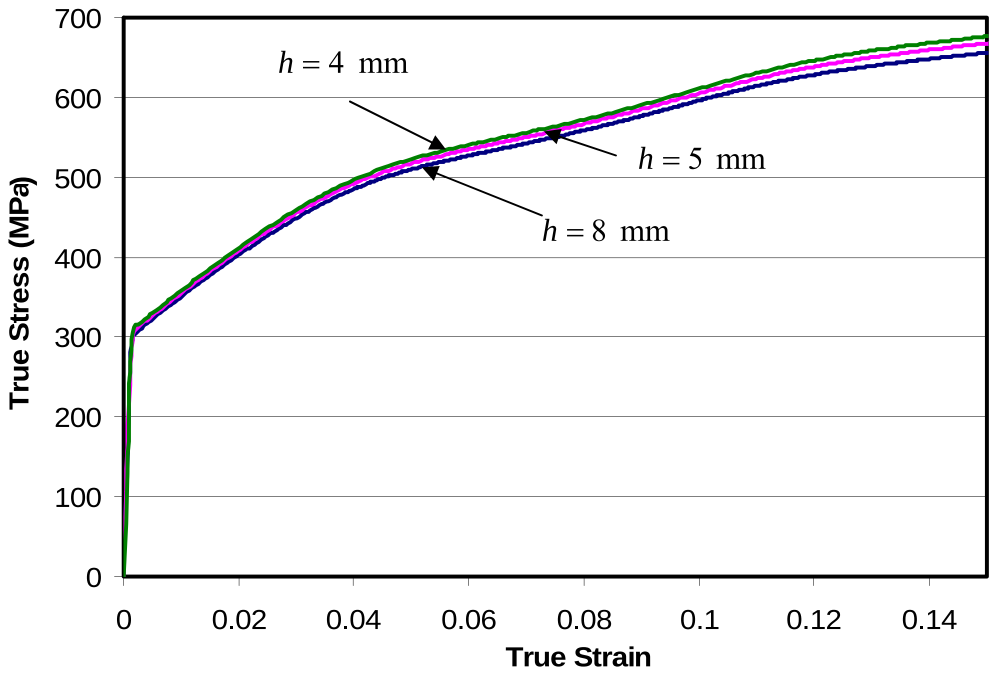


**Figure 4.7** True stress-true total strain curves of different specimen height (Material: C15, $\mu_u = 0.1$, $\mu_l = 0.1$, $b = 5$ mm)

## 4.5 Effect of Friction

The friction coefficient and its effects play an important role in determination of flow curve of the material. In order to analyze the effects of the Coulomb friction coefficient, the values for friction coefficient are varied either keeping same coefficient of friction on upper and lower contact surfaces or assigning different friction coefficients to different surfaces.

### 4.5.1 Effect of Same Friction Coefficient on Upper and Lower Surfaces

Three different Coulomb friction coefficient values are assigned to the upper and lower contact surfaces during calculations. The coefficients used are same for both surfaces. They are 0.1, 0.2 and 0.4.

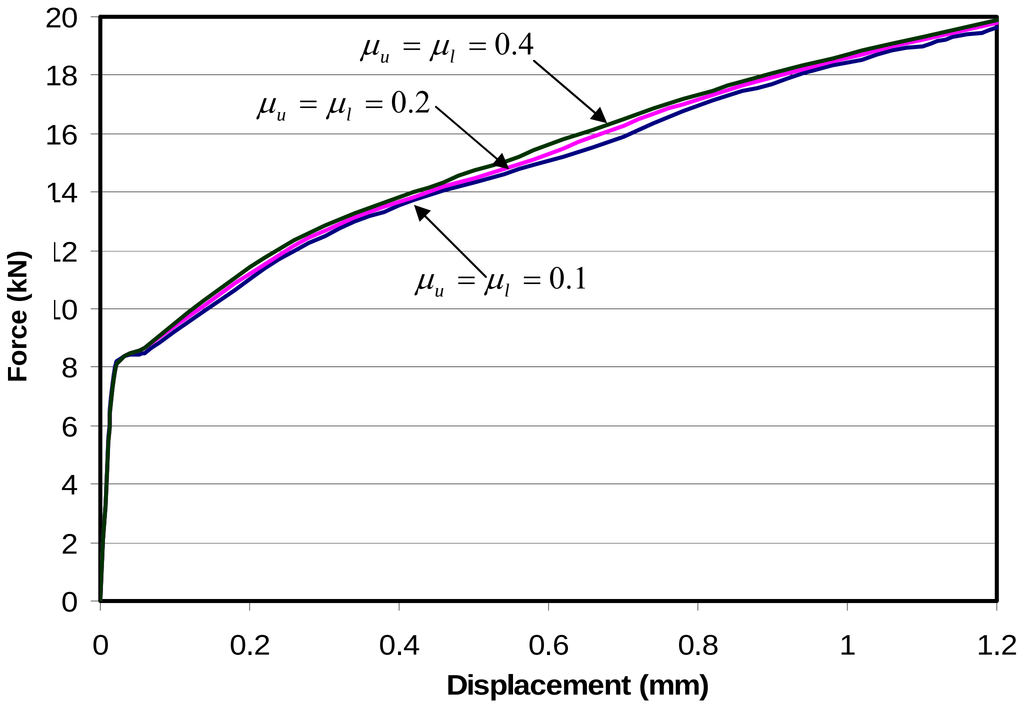


**Figure 4.8** True stress-true strain curves of different friction coefficients (3D prismatic specimen, Material: C15, $h$ = 8 mm, $b$ = 5 mm)

Figure 4.8 gives force-displacement curves of compression with the assigned Coulomb friction coefficient values. As expected, higher forces are needed for the same amount of displacement when coefficient of friction is higher.

From these curves, a multiplying factor for the friction coefficient is obtained and the plot of the multiplying factors versus $b/h$ value is given in Figure 4.9. To calculate the friction multiplying factor which is denoted by $Q$, the frictionless analysis is conducted for upper and lower contact surfaces. For each increment, the force results for the specified coefficient of friction are divided by the force value without friction as given by Eqn. (4.4). This value is plotted against the ratio $b/h$ and trendlines of the data are also given in Figure 4.9.

$$Q = \frac{F_{\mu \neq 0}}{F_{\mu = 0}} \tag{4.4}$$

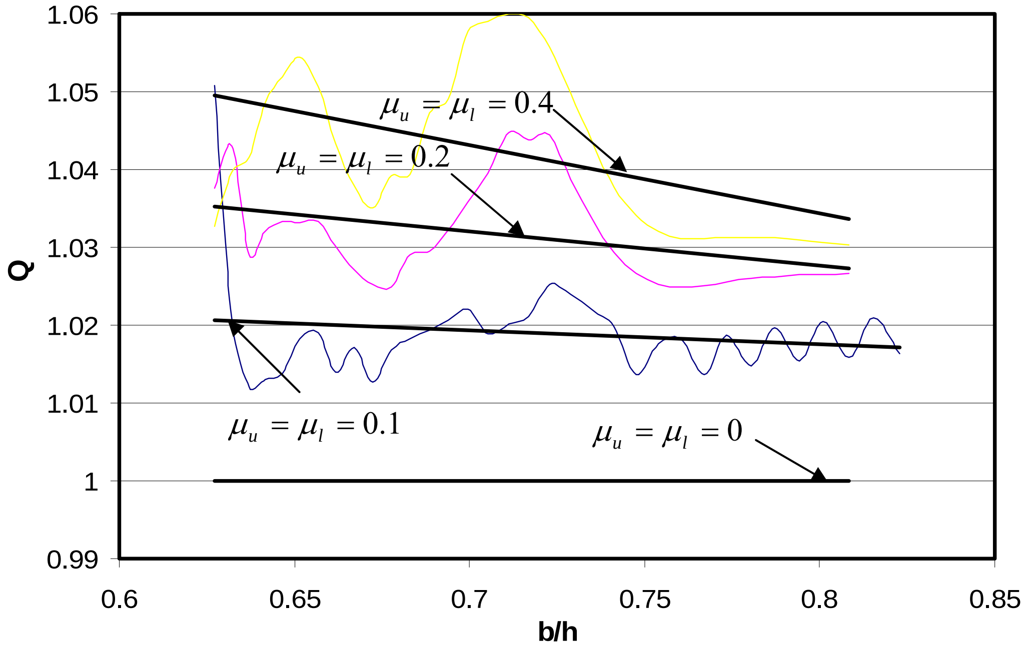


**Figure 4.9** Friction multiplying factor for compression tests

The friction multiplying factor is advantageous in that it gives an estimate of forces and stresses for a known coefficient of friction.

### 4.5.2 Effect of Different Friction Coefficient on Upper and Lower Surfaces

It is visible that the surface qualities of the anvil and the compression punch used in the experiments are different. This can cause friction coefficients different from each other on upper and lower surfaces. This case is analyzed assigning Coulomb coefficient of friction on the upper surface as 0.1, 0.2 and 0.4 for different calculations since the upper surface is rougher than the lower surface, and coefficient of friction for the lower surface is assigned 0.1 for all three calculations. Other parameters are given in Table 4.2.

**Table 4.2** Modeling conditions for different friction compression tests

| | |
|---|---|
| Model | A quarter model with 2 symmetry planes |
| Specimen dimensions | $h$ = 8 mm, $b$ = 5 mm |
| Material | C15 |
| Number of elements | 3200 |
| Element type | 8 node hexahedral |
| Total loadcase time (sec) | 12 |
| Number of steps | 60 |
| Punch velocity (mm/sec) | 0.2 |
| $\mu_u$ | 0.1, 0.2, 0.4 |
| $\mu_l$ | 0.1 |
| Relative force tolerance (δ) | 0.01 |
| Termination | Maximum force, 5000 N |

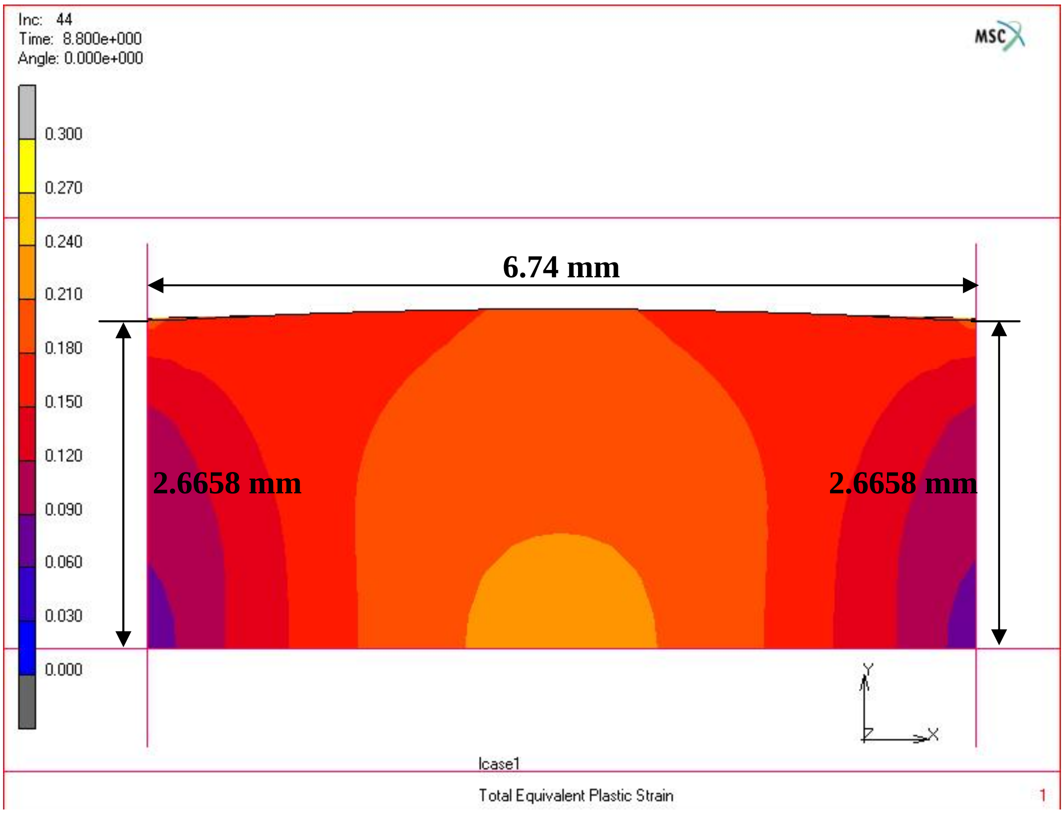


**Figure 4.10** Total equivalent plastic strain for $\mu_u = 0.1$ and $\mu_l = 0.1$

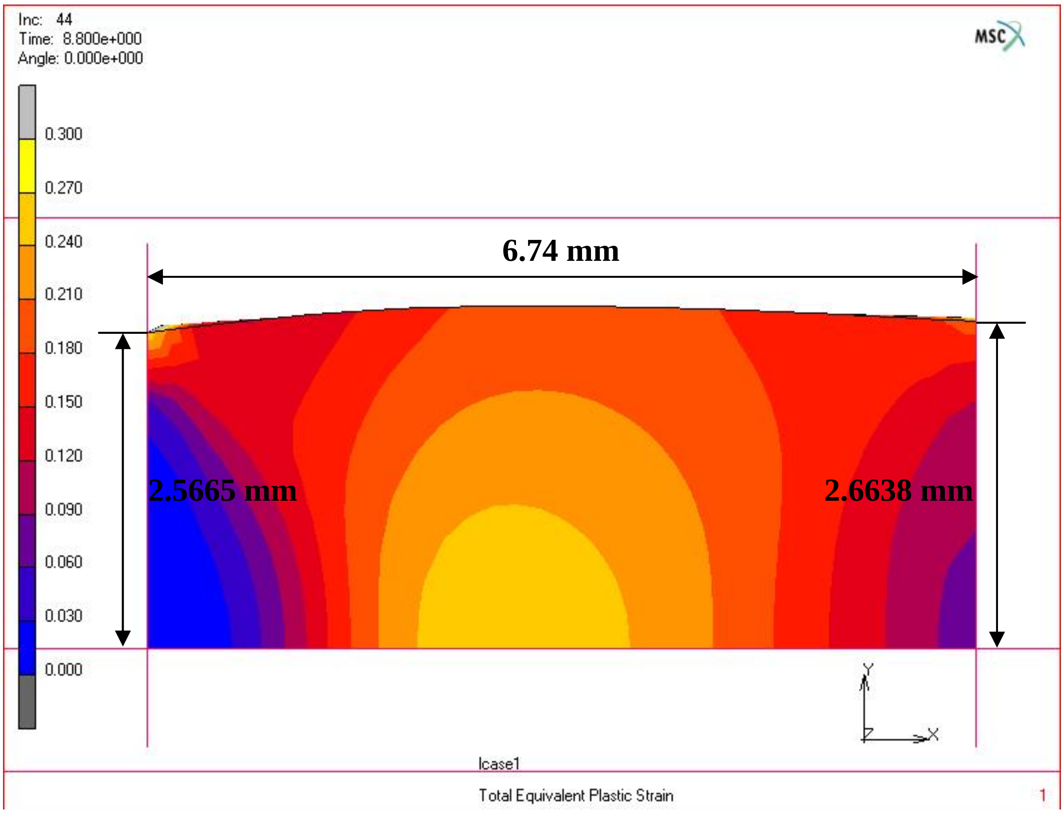


**Figure 4.11** Total equivalent plastic strain for $\mu_u = 0.4$ and $\mu_l = 0.1$

Figures 4.10 and 4.11 show total equivalent plastic strain values and side dimensions for $\mu_u = 0.4$, $\mu_l = 0.1$ and $\mu_u = 0.1$, $\mu_l = 0.1$. Different coefficient of friction on upper and lower surfaces result in unsymmetrical geometry where on the surface with higher friction coefficient the surface area is smaller than the area of surface with smaller friction coefficient. The maximum dimension of barreling appeared closer to the surface with higher friction. The strain distributions can also be compared by looking at Figures 4.10 and 4.11. Comparison of force-displacement curves are given in Figure 4.12. When friction coefficient on the upper surface increases, the forces also increase as expected.

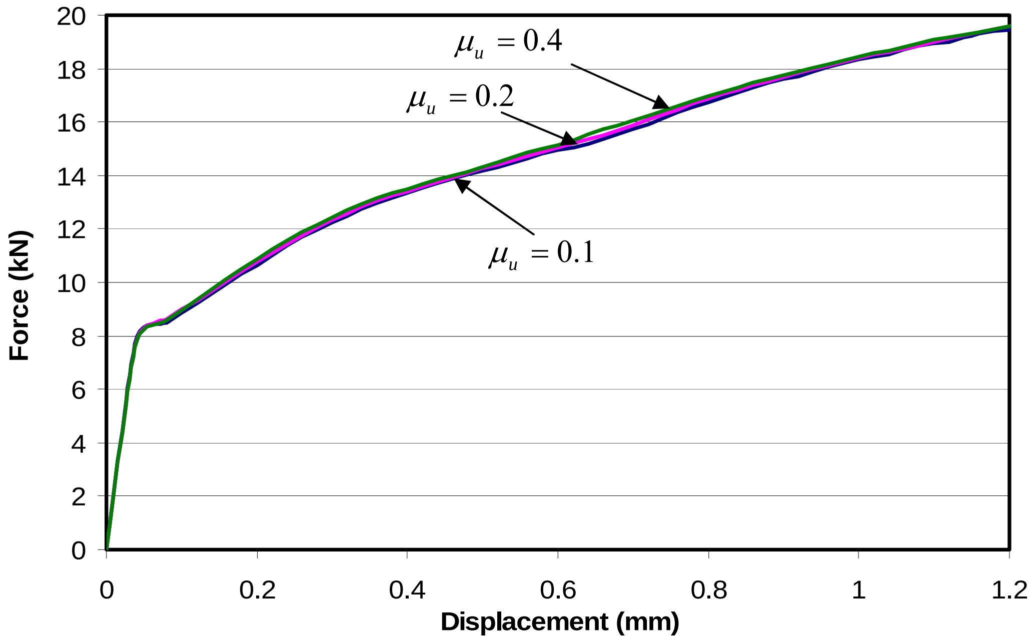


**Figure 4.12** Force-displacement curves of compression for different Coulomb coefficient of friction on upper and lower surfaces ($\mu_l = 0.1$)

## 4.6 Effect of Tilting of Upper Punch

As for the indentation, there is a possibility of tilting of the compression punch. A three-dimensional analysis is performed for tilting angles of 0.2° and 0.5° then the results are compared with perfectly parallel compression case. The model used for analysis of tilting of the indenter has one plane of symmetry. Modeling conditions for tilting of the upper punch are as given in Table 4.3.

The force-displacement results of compression with tilted punch are given in Figure 4.13. The effect is dominant especially at the elastic part of compression.

The angles 0.2° and 0.5° correspond to 0.11 mm and 0.28 mm height difference respectively for the compression punch which has a diameter of 32 mm. Although it is possible to recognize 0.1 mm with naked eye, smaller height differences may not be recognized. In addition, the parallelity of the compression punch must be checked circumferentially whereas it is enough to check from one side for the indenter. It is easier to adjust the indenter because the indenter is longitudinal and the only visible parallelity is in the longitudinal direction. But the compression punch is axisymmetric and this increases possibility of making an error in parallelity adjustment of it.

**Table 4.3** Modeling conditions for different friction compression tests

| | |
|---|---|
| Model | Half model with one symmetry plane |
| Specimen dimensions | $h$ = 8 mm, $b$ = 5 mm |
| Material | C15 |
| Number of elements | 6400 |
| Element type | 8 node hexahedral |
| Material | C15 |
| Total loadcase time (sec) | 120 |
| Number of steps | 800 |
| Punch velocity (mm/sec) | 0.0166667 |
| $\mu_u$ , $\mu_l$ | 0.1 |
| Relative force tolerance (δ) | 0.01 |
| Termination | Maximum force, 10000 N |

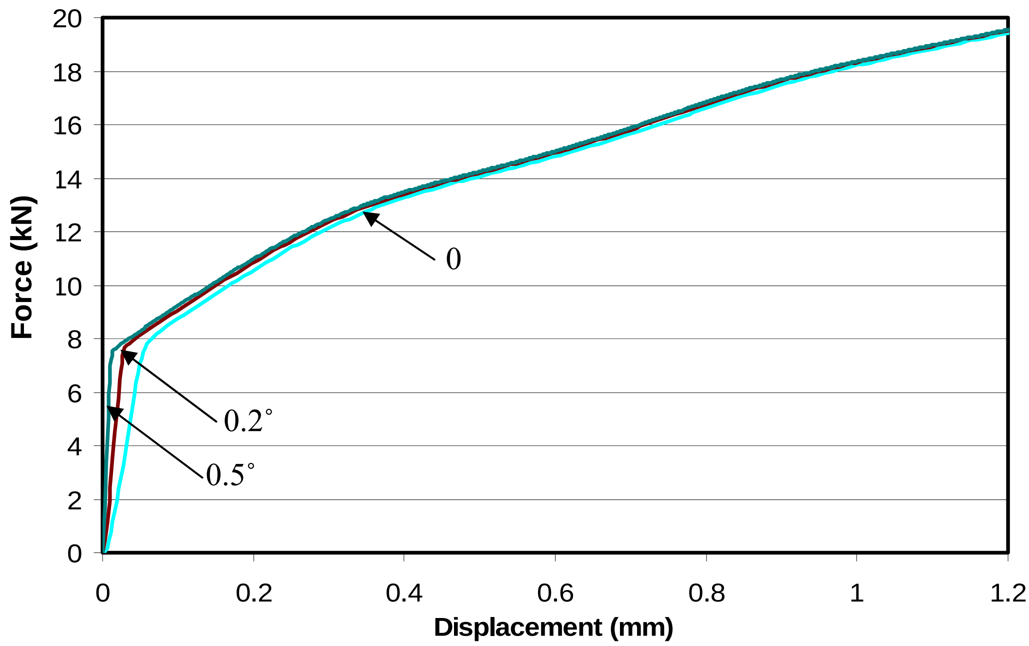


**Figure 4.13** Force-displacement curves of compression with tilted punch

This analysis shows that non-parallelity of the anvil and compression punch or upper and lower surfaces of the specimens affect flow curves. This effect is more dominant in the elastic region.

## 4.7 Conclusions

The aim of this chapter was to investigate the decrease of true stress-true strain curves and geometric irregularities after compression. For this purpose two different specimen geometries are analyzed. The specimen height is varied and different friction coefficients are assigned to lower and upper contact surfaces.

The forces or stresses have shown no decrease as in the experimental results. On the other hand, had there been buckling of the specimen with height 8 mm, it could be seen in the simulations with half symmetry. The analyses in this chapter enlightened the process but could not answer questions about unexpected experimental results. This shows that answers are to be searched in experimental errors and adjustments.

# CHAPTER 5

# UPPER BOUND METHOD SOLUTION OF INDENTATION

## 5.1 Introduction

In this chapter, upper bound method approach to the plane strain indentation is considered. This method gives an estimate of the load by equating the internal rate of energy dissipation to the rate at which external forces do work. For this purpose, a pattern of deformation is assumed and the calculated forces will be greater than or equal to the correct load.

Basically, a flow field is assumed which accounts for the required shape change. Energy consumed internally in this deformation field is calculated and equated to external work.

## 5.2 Upper Bound Model I

### 5.2.1 Problem and Model Description

In this indentation problem, there is a long indenter with a radius and there is a workpiece. It is assumed that the workpiece and indenter contact length is long enough to fulfill plane strain assumption. In fact, it is proven by finite element analyses in [42] that indentation in reality cannot reach plane strain conditions with increasing length. Still this assumption is used because it is much easier to handle the problem analytically with plane strain assumption. On the other hand, it is assumed that the workpiece is large enough so that deformation occurs only in a limited zone around the indenter and the rest of the workpiece acts as a dead zone.

For upper bound method solution, the problem is modeled by some assumptions and approximations. Figure 5.1 shows the workpiece divided into areas each of which have their own velocity fields. Between these areas there are the discontinuity surfaces where the continuity of velocity fields perpendicular to these surfaces must be fulfilled.

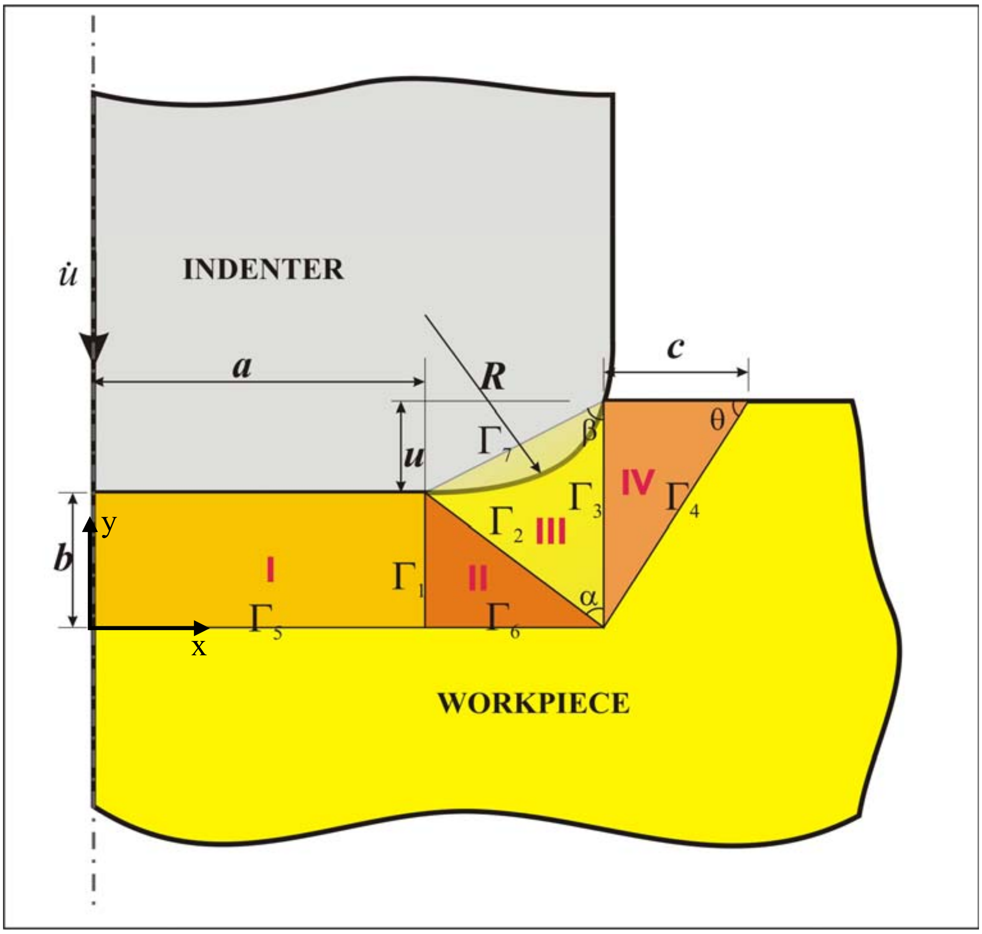


**Figure 5.1** Upper bound model of plane strain indentation (Model I)

### 5.2.2 Basic Assumptions and Approximations

The material is assumed to be isotropic and homogeneous. The effect of strain rate on flow stress is neglected as well as that of strain hardening which may be introduced to the solution later. The tool workpiece interface is considered to be either frictionless or to have constant shear stress. In this model, the circular boundary of the indenter is approximated by a line. The velocity fields are assumed to be uniform except for Area I.

### 5.2.3 Velocity Fields and Determination of Velocity Components

The velocity fields are considered to be uniform in areas II, III and IV. These areas behave as rigid blocks. Only area I can deform, and in this area x and y components of velocity are assumed to be $\dot{u}_x = \dot{u}_x(x)$ and $\dot{u}_y = \dot{u}_y(y)$.

Between the areas, normal component of the velocity field must be continuous while the tangential component is discontinuous. This causes shearing of the material.

Using these velocity fields the rate of energy dissipation within the areas, the rate of energy dissipation due to shearing of the material by the tangential velocity discontinuity and the rate of work caused by friction between tool and workpiece surface are calculated.

In the Figure 5.1 and in the following formulations $\dot{u}$ corresponds to the tool velocity. The depth of workpiece is taken as L.

#### 5.2.3.1 Velocity Field of Area I

Figure 5.2 is a part of the workpiece just beneath the indenter. The material flow direction is marked.

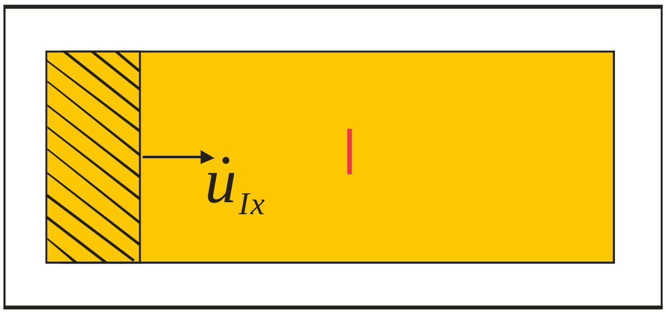


**Figure 5.2** Determination of x-component of velocity field for Area I

The velocity field in this area is found by using global volume invariancy. The material entering the control volume must be equal to the material leaving the control volume. This leads to Eqn. (5.1).

$$\dot{u} \cdot x \cdot L = \dot{u}_{Ix} \cdot b \cdot L \tag{5.1}$$

With the assumption $\dot{u}_x = \dot{u}_x(x)$ Eqn. (5.2) is obtained.

$$\dot{u}_{Ix} = \frac{\dot{u} \cdot x}{b} \tag{5.2}$$

In this area, $\dot{\varepsilon}_x$ which is the strain rate in x direction is found as in Eqn. (5.4).

$$\dot{\varepsilon}_x = \frac{\partial u_x}{\partial x} \tag{5.3}$$

$$\dot{\varepsilon}_x = \frac{\dot{u}}{b} \tag{5.4}$$

Using local volume invariancy $\dot{\varepsilon}_x + \dot{\varepsilon}_y + \dot{\varepsilon}_z = 0$ and the plane strain assumption $\dot{\varepsilon}_z = 0$, $\dot{\varepsilon}_y$ is obtained as in Eqn. (5.5).

$$\dot{\varepsilon}_y = -\dot{\varepsilon}_x = -\frac{\dot{u}}{b} \tag{5.5}$$

The equivalent plastic strain rate is calculated by Eqn. (5.6) using Eqn.s (5.4) and (5.5). In addition $\dot{\varepsilon}_{xy} = 0$ since $\dot{u}_x = \dot{u}_x(x)$ and $\dot{u}_y = \dot{u}_y(y)$. Then, equivalent plastic strain rate is given by Eqn. (5.7).

$$\dot{\bar{\varepsilon}} = \sqrt{\frac{2}{3}\cdot\left(\dot{\varepsilon}_x{}^2 + \dot{\varepsilon}_y{}^2\right) + \frac{4}{3}\cdot\dot{\varepsilon}_{xy}{}^2} = \sqrt{\frac{2}{3}\cdot\left(2\cdot\frac{\dot{u}^2}{b^2}\right)} \tag{5.6}$$

$$\dot{\bar{\varepsilon}} = \frac{2}{\sqrt{3}}\cdot\frac{\dot{u}}{b} \tag{5.7}$$

From the strain rate $\dot{\varepsilon}_y$ which is given by Eqn. (5.5) the velocity component in y-direction for Area I can be obtained by integration.

$$\dot{\varepsilon}_y = \frac{\partial \dot{u}_{Iy}}{\partial y} = -\frac{\dot{u}}{b}$$

$$\dot{\varepsilon}_y = \frac{\partial \dot{u}_{Iy}}{\partial y} = \frac{d\dot{u}_{Iy}}{dy} \quad \text{since } \dot{u}_y \neq \dot{u}_y(x)$$

$$\dot{u}_{Iy} = \int d\dot{u}_{Iy} = \int -\frac{\dot{u}}{b}\cdot dy$$

$$\dot{u}_{Iy} = -\frac{\dot{u}}{b}\cdot y + c \tag{5.8}$$

The boundary conditions are $\dot{u}_{Iy} = 0$ at $y = 0$ and $\dot{u}_{Iy} = -\dot{u}$ at $y = b$. This makes $c = 0$ and $\dot{u}_{Iy}$ is given by Eqn. (5.9).

$$\dot{u}_{Iy} = -\frac{\dot{u}}{b}\cdot y \tag{5.9}$$

Equivalent plastic strain can also be calculated by integrating $\dot{\bar{\varepsilon}}$.

$$\bar{\varepsilon} = \int \dot{\bar{\varepsilon}} \cdot dt = \int \frac{2}{\sqrt{3} \cdot b} \cdot \frac{du}{dt} \cdot dt = \frac{2}{\sqrt{3} \cdot b} \cdot \int_0^u du = \frac{2 \cdot u}{\sqrt{3} \cdot b} \qquad (5.10)$$

### 5.2.3.2 Velocity Field of Area II

Figure 5.3 shows a closer view of Area II. The velocity field of this area is found using continuity of velocities on surfaces $\Gamma_1$ and $\Gamma_6$.

Velocity continuity on surface $\Gamma_1$ requires that at $x=a$ Eqn. (5.11) is valid.

$$\dot{u}_{Ix} = \dot{u}_{IIx} = \dot{u} \cdot \frac{a}{b} \qquad (5.11)$$

From surface $\Gamma_6$ it is seen that $\dot{u}_{IIy} = 0$ since there is no material flow perpendicular to this surface. So the velocity of this area has only x component and is as in Eqn. (5.12).

$$\dot{u}_{II} = \dot{u} \cdot \frac{a}{b} \qquad (5.12)$$

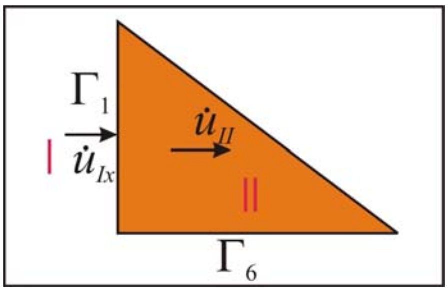


**Figure 5.3** The velocity field for Area II

### 5.2.3.3 Velocity Field of Area III

Figure 5.4 is a sketch of Area III showing velocity components. Using material continuity on surfaces $\Gamma_2$ and $\Gamma_7$ which is the surface in contact with the indenter Eqn.s (5.13) and (5.14) are obtained.

$$\dot{u}_{IIx} \cdot \cos\alpha = \dot{u}_{IIIx} \cdot \cos\alpha + \dot{u}_{IIIy} \cdot \sin\alpha \tag{5.13}$$

$$\dot{u} \cdot \sin\beta = \dot{u}_{IIIx} \cdot \cos\beta - \dot{u}_{IIIy} \cdot \sin\beta \tag{5.14}$$

Then, the velocity components are calculated as in Eqn.s (5.15) and (5.16).

$$\dot{u}_{IIIy} = \frac{\dot{u}_{IIx} - \dot{u} \cdot \tan\beta}{\tan\alpha + \tan\beta} \tag{5.15}$$

$$\dot{u}_{IIIx} = \dot{u} \cdot \tan\beta + \dot{u}_{IIIy} \cdot \tan\beta \tag{5.16}$$

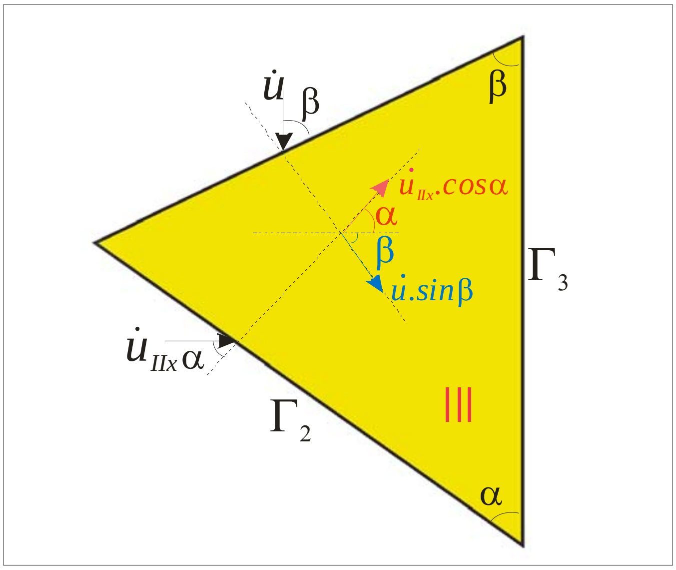


**Figure 5.4** The velocity field for Area III

### 5.2.3.4 Velocity Field of Area IV

The velocity field in this area is parallel to the $\Gamma_4$ surface. Since continuity must be fulfilled on the $\Gamma_3$ surface, the x component of the velocity field of this area is equal to the x component of the velocity field in Area III. This is given by Eqn. (5.17).

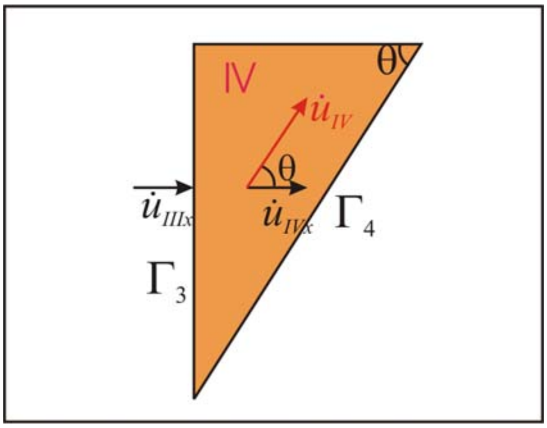


**Figure 5.5** A representation of velocity field in Area IV

$$\dot{u}_{IVx} = \dot{u}_{IIIx} \tag{5.17}$$

$$\dot{u}_{IVy} = \dot{u}_{IVx} \cdot \tan\theta = \dot{u}_{IV} \cdot \sin\theta \tag{5.18}$$

### 5.2.4 Geometry Analysis of Model I

Figure 5.6 is a closer look to the model. Some necessary angles and dimension are marked on the figure and are going to be derived.

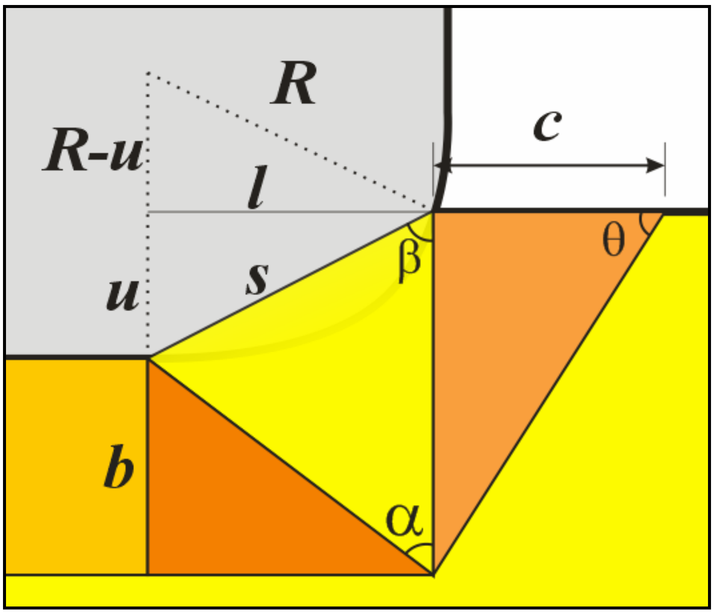


**Figure 5.6** Geometry and angle analysis for Model I

From Figure 5.6 the dimensions *l* and *s* are derived using Pythagoras' theorem as in Eqn.s (5.19) and (5.20).

$$l = \sqrt{R^2 - (R-u)^2} = \sqrt{2 \cdot R \cdot u - u^2} \tag{5.19}$$

$$s = \sqrt{l^2 + u^2} = \sqrt{2 \cdot R \cdot u - u^2 + u^2} = \sqrt{2 \cdot R \cdot u} \tag{5.20}$$

The angles are determined by their arctangent values as in Eqn.s (5.21),(5.22) and (5.23).

$$\alpha = \arctan\left(\frac{\sqrt{2 \cdot R \cdot u - u^2}}{b}\right) \tag{5.21}$$

$$\beta = \arctan\left(\frac{\sqrt{2 \cdot R \cdot u - u^2}}{u}\right) \tag{5.22}$$

$$\theta = \arctan\left(\frac{b+u}{c}\right) \tag{5.23}$$

### 5.2.5 Determination of Power Terms

The total rate of work calculated by using a velocity field model is formulated as given in Eqn. (5.24).

$$P_m = P_D + P_\Gamma + P_{fr} \tag{5.24}$$

In this formulation $P_D$ is the rate of energy dissipation within the areas and is calculated as in Eqn. (5.25).

$$P_D = \sum \sigma_f \int_V \dot{\bar{\varepsilon}} \cdot dV \tag{5.25}$$

$P_\Gamma$ is the rate of energy dissipation due to shearing of the material by the tangential velocity discontinuity and is formulated as in Eqn. (5.26).

$$P_\Gamma = \sum \frac{\sigma_f}{\sqrt{3}} \cdot \int_{A_\Gamma} |\Delta \dot{u}_t| \cdot dA_\Gamma \tag{5.26}$$

$P_{fr}$ is the rate of work caused by friction between tool and workpiece surface. It is calculated by Eqn. (5.27).

$$P_{fr} = \sum \frac{m \cdot \sigma_f}{\sqrt{3}} \cdot \int_{Afr} |\Delta \dot{u}_t| \cdot dA_{fr} \tag{5.27}$$

These power terms are calculated for each area and surface and then summed up to get the total rate of work.

### *Area I*

The energy dissipation caused by the relative velocity between tool surface and workpiece is calculated as in Eqn. (5.28). In this case, relative velocity corresponds to the velocity of material in x-direction in Area I since the indenter has no y-component of velocity.

$$\begin{aligned} P_{fr1} &= m \cdot \frac{\sigma_f}{\sqrt{3}} \cdot \int_{A_{fr}} |\dot{u}_t| \cdot dA_{fr} \\ &= m \cdot \frac{\sigma_f}{\sqrt{3}} \cdot \int_0^a \frac{\dot{u} \cdot x}{b} \cdot L \cdot dx \\ &= m \cdot \frac{\sigma_f}{\sqrt{3}} \cdot \frac{\dot{u}}{b} \cdot L \cdot \left. \frac{x^2}{2} \right|_0^a \end{aligned}$$

$$P_{fr1} = m \cdot \frac{\sigma_f}{\sqrt{3}} \cdot \frac{\dot{u}}{b} \cdot L \cdot \frac{a^2}{2} \tag{5.28}$$

On $\Gamma_5$ surface $\left|\Delta \dot{u}_t\right| = \dfrac{\dot{u} \cdot x}{b}$ and the infinitesimal area is $dA_{\Gamma 5} = L \cdot dx$. The rate of energy dissipation due to shearing of the material on surface $\Gamma_5$ is calculated as given by the Eqn. (5.29) using Eqn. (5.26).

$$P_{\Gamma 5} = \frac{\sigma_f}{\sqrt{3}} \cdot \int_{A_{\Gamma 5}} \left|\Delta \dot{u}_t\right| \cdot dA_{\Gamma 5} = \frac{\sigma_f}{\sqrt{3}} \cdot \int_0^a \frac{\dot{u} \cdot x}{b} \cdot L \cdot dx = \frac{\sigma_f}{2\sqrt{3}} \cdot \frac{\dot{u}}{b} \cdot L \cdot a^2$$

$$P_{\Gamma 5} = \frac{\sigma_f}{2\sqrt{3}} \cdot \frac{\dot{u}}{b} \cdot L \cdot a^2 \tag{5.29}$$

The rate of energy dissipation in Area I is calculated from Eqn. (5.25). The infinitesimal volume is $dV = a \cdot L \cdot dy$ and the equivalent strain rate is calculated in Eqn (5.7). The result is given by Eqn. (5.30).

$$P_{D1} = \sigma_f \cdot \int \dot{\bar{\varepsilon}} \cdot dV = \sigma_f \cdot \int_0^b \frac{2}{\sqrt{3}} \cdot \frac{\dot{u}}{b} \cdot a \cdot L \cdot dy = \frac{2}{\sqrt{3}} \cdot \sigma_f \cdot \frac{\dot{u}}{b} \cdot a \cdot L \cdot b$$

$$P_{D1} = \frac{2}{\sqrt{3}} \cdot \sigma_f \cdot \dot{u} \cdot a \cdot L \tag{5.30}$$

*Area II*

The shear power term on surface $\Gamma_1$ is calculated using Eqn. (5.26). On this surface $\left|\Delta \dot{u}_t\right|$ corresponds to the y-component of velocity in Area I since Area II has no vertical motion. The infinitesimal area is $dA_{\Gamma 1} = L \cdot dy$. Then, the rate of energy dissipation during shearing on this surface is given by Eqn. (5.31).

$$P_{\Gamma 1} = \frac{\sigma_f}{\sqrt{3}} \cdot \int_{A_{\Gamma 5}} |\Delta \dot{u}_t| \cdot dA_{\Gamma 1} = \frac{\sigma_f}{\sqrt{3}} \cdot \int_0^b \frac{\dot{u} \cdot y}{b} \cdot L \cdot dy = \frac{\sigma_f}{2\sqrt{3}} \cdot \frac{\dot{u}}{b} \cdot L \cdot b^2$$

$$P_{\Gamma 1} = \frac{\sigma_f}{\sqrt{3}} \cdot \int_{A_{\Gamma 5}} |\Delta \dot{u}_t| \cdot dA_{\Gamma 1} = \frac{\sigma_f}{\sqrt{3}} \cdot \int_0^b \frac{\dot{u} \cdot y}{b} \cdot L \cdot dy = \frac{\sigma_f}{2\sqrt{3}} \cdot \dot{u} \cdot L \cdot b$$

$$P_{\Gamma 1} = \frac{\sigma_f}{2\sqrt{3}} \cdot \dot{u} \cdot L \cdot b \tag{5.31}$$

Since the areas except for Area I behave as rigid blocks, the equivalent strain rate is $\dot{\bar{\varepsilon}} = 0$, so no energy is dissipated during deformation.

$$P_{DII} = 0 \tag{5.32}$$

The rate of energy dissipation due to shearing of the material on surface $\Gamma_6$ is:

$$P_{\Gamma 6} = \frac{\sigma_f}{\sqrt{3}} \cdot \int_{A_{\Gamma 6}} |\Delta \dot{u}_t| \cdot dA_{\Gamma 6} \tag{5.33}$$

$$P_{\Gamma 6} = \frac{\sigma_f}{\sqrt{3}} \cdot \dot{u}_{II} \cdot \sqrt{2 \cdot R \cdot u - u^2} \cdot L \tag{5.34}$$

where $|\Delta \dot{u}_t| = \dot{u}_{II} = \dot{u} \cdot \dfrac{a}{b}$ and $A_{\Gamma 6} = \sqrt{2 \cdot R \cdot u - u^2} \cdot L$ from geometry.

*Area III*

The power caused by friction between the tool and workpiece on surface $\Gamma_7$ is calculated by Eqn. (5.22).

The relative tangential velocity on the contact surface is found as in Eqn. (5.35).

$$\left|\Delta \dot{u}_t\right| = \left|\dot{u}_{IIIy} \cdot \cos\beta + \dot{u}_{IIIx} \cdot \sin\beta + \dot{u} \cdot \cos\beta\right| \tag{5.35}$$

Then, from Eqn. (5.22) combining with Eqn (5.35) and the area of surface $\Gamma_7$ where $A_{\Gamma 7} = \sqrt{2 \cdot R \cdot u} \cdot L$, rate of work caused by friction is obtained as in Eqn. (5.36).

$$P_{fr3} = m \cdot \frac{\sigma_f}{\sqrt{3}} \cdot \left|\dot{u}_{IIIy} \cdot \cos\beta + \dot{u}_{IIIx} \cdot \sin\beta + \dot{u} \cdot \cos\beta\right| \cdot \sqrt{2 \cdot R \cdot u} \cdot L \tag{5.36}$$

On the shear surface $\Gamma_2$ between Area II and Area III, the relative tangential velocity is obtained as in Eqn. (5.37).

$$\left|\Delta \dot{u}_t\right| = \left|\dot{u}_{IIIx} \cdot \sin\alpha - \dot{u}_{IIIy} \cdot \cos\alpha - \dot{u}_{IIx} \cdot \sin\alpha\right| \tag{5.37}$$

Then,

$$P_{\Gamma 2} = \frac{\sigma_f}{\sqrt{3}} \cdot \left|\dot{u}_{IIIx} \cdot \sin\alpha - \dot{u}_{IIIy} \cdot \cos\alpha - \dot{u}_{IIx} \cdot \sin\alpha\right| \cdot \sqrt{2 \cdot R \cdot u - u^2 + b^2} \cdot L \tag{5.38}$$

where $A_{\Gamma 2} = \sqrt{2 \cdot R \cdot u - u^2 + b^2} \cdot L$.

The rate of energy dissipation caused by deformation within Area III is given by Eqn. (5.39) since $\dot{\bar{\varepsilon}} = 0$.

$$P_{DIII} = 0 \tag{5.39}$$

### *Area IV*

For the $\Gamma_3$ surface power dissipated due to shearing of the material is formulated again by using Eqn. (5.26). First, the relative tangential velocity is found as given by Eqn. (5.40) and area of the shear surface is calculated by Eqn. (5.41).

$$\left|\Delta \dot{u}_t\right| = \left|\dot{u}_{IIIy} - \dot{u}_{IVy}\right| \tag{5.40}$$

$$A_{\Gamma 3} = (b+u) \cdot L \tag{5.41}$$

Then, using Eqn.s (5.40) and (5.41) in Eqn. (5.26), Eqn. (5.42) is obtained.

$$P_{\Gamma 3} = \frac{\sigma_f}{\sqrt{3}} \cdot \left| \dot{u}_{IIIy} - \dot{u}_{IVy} \right| \cdot \left( b+u \right) \cdot L \tag{5.42}$$

For the $\Gamma_4$ surface, power dissipated due to shearing of the material calculated following the same procedure as surface $\Gamma_3$. Relative tangential velocity and the area are given by Eqn.s (5.43) and (5.44) respectively.

$$\left| \Delta \dot{u}_t \right| = \left| \dot{u}_{IV} \right| \tag{5.43}$$

$$A_{\Gamma 4} = \sqrt{\left( b+u \right)^2 + c^2} \cdot L \tag{5.44}$$

Then, the shear power is formulated as in Eqn. (5.45).

$$P_{\Gamma 4} = \frac{\sigma_f}{\sqrt{3}} \cdot \left| \dot{u}_{IV} \right| \cdot \sqrt{\left( b+u \right)^2 + c^2} \cdot L \tag{5.45}$$

The power dissipated within the Area IV is given by Eqn. (5.46) since $\dot{\bar{\varepsilon}} = 0$.

$$P_{DIV} = 0 \tag{5.46}$$

### 5.2.6 Non-Dimensional Power Terms

The dimensionless parameters $u^* = \dfrac{u}{a}, R^* = \dfrac{R}{a}, b^* = \dfrac{b}{a}, c^* = \dfrac{c}{a}, P_m^* = \dfrac{P_m}{\sigma_f \cdot \dot{u} \cdot a \cdot L}$ are used in all power terms in calculations. Dividing all terms by $\sigma_f \cdot \dot{u} \cdot a \cdot L$ and also writing $u$, $R$, $b$, $c$ in form of $u^*$, $R^*$, $b^*$, $c^*$ by simplifying with $a$, the total power is made non-dimensional.

The dimensionless equivalents of some power terms are given in Eqn.s (5.47) to (5.52).

$$P^*_{fr1} = \frac{m}{2\sqrt{3}\cdot b^*} \tag{5.47}$$

$$P^*_{\Gamma 5} = \frac{1}{2\sqrt{3}\cdot b^*} \tag{5.48}$$

$$P^*_{DI} = \frac{2}{\sqrt{3}} \tag{5.49}$$

$$P^*_{\Gamma 6} = \frac{\sqrt{2\cdot R^*\cdot u^* - u^{*2}}}{b^*\cdot\sqrt{3}} \tag{5.50}$$

$$P^*_{DII} = 0 \tag{5.51}$$

$$P^*_{\Gamma 1} = \frac{b^*}{2\sqrt{3}} \tag{5.52}$$

For the rest of the power terms, for simplicity, first the velocity fields are simplified by $\dot{u}$ since this term in the power exists because of the relative velocity. Then, the power term is divided by $\sigma_f \cdot a \cdot L$. So, the dimensionless velocity components are obtained as in Eqn.s (5.53) to (5.56).

$$\dot{u}^*_{IIx} = \frac{1}{b^*} \tag{5.53}$$

$$\dot{u}^*{}_{IIIx} = \tan\beta + \dot{u}^*{}_{IIIy} \cdot \tan\beta \qquad (5.54)$$

$$\dot{u}^*{}_{IIIy} = \frac{\frac{1}{b^*} - \tan\beta}{\tan\alpha + \tan\beta} \qquad (5.55)$$

$$\dot{u}^*{}_{IV} = \frac{\dot{u}^*{}_{IIIx}}{\cos\theta} \qquad (5.56)$$

The dimensionless power terms are as in Eqn.s (5.57) to (5.62).

$$P^*_{fr7} = \frac{m}{\sqrt{3}} \cdot \left| \dot{u}^*{}_{IIIy} \cdot \cos\beta + \dot{u}^*{}_{IIIx} \cdot \sin\beta + \dot{u}^* \cdot \cos\beta \right| \cdot \sqrt{2 \cdot R^* \cdot u^*} \qquad (5.57)$$

$$P^*_{\Gamma 2} = \frac{1}{\sqrt{3}} \cdot \left| \dot{u}^*{}_{IIIx} \cdot \sin\alpha - \dot{u}^*{}_{IIIy} \cdot \cos\alpha - \dot{u}^*{}_{IIx} \cdot \sin\alpha \right| \cdot \sqrt{2 \cdot R^* \cdot u^* - u^{*2} + b^{*2}} \qquad (5.58)$$

$$P^*_{DIII} = 0 \qquad (5.59)$$

$$P^*_{\Gamma 3} = \frac{1}{\sqrt{3}} \cdot \left| \dot{u}^*{}_{IV} \cdot \sin\theta - \dot{u}^*{}_{IIIy} \right| \cdot \left(b^* + u^*\right) \qquad (5.60)$$

$$P^*_{\Gamma 4} = \frac{1}{\sqrt{3}} \cdot \left| \dot{u}^*{}_{IV} \right| \cdot \sqrt{\left(b^* + u^*\right)^2 + c^{*2}} \qquad (5.61)$$

$$P^*_{DIV} = 0 \qquad (5.62)$$

The angles in terms of dimensionless parameters are given in Eqn.s (5.63), (5.64) and (5.65).

$$\alpha = \arctan\left(\frac{\sqrt{2 \cdot R^* \cdot u^* - u^{*2}}}{b^*}\right) \tag{5.63}$$

$$\beta = \arctan\left(\frac{\sqrt{2 \cdot R^* \cdot u^* - u^{*2}}}{u^*}\right) \tag{5.64}$$

$$\theta = \arctan\left(\frac{b^* + u^*}{c^*}\right) \tag{5.65}$$

### 5.2.7 Force-Displacement Data

$P_m$ which is the total rate of work calculated by summing all the power terms caused by friction, shearing of the surfaces and deformation of the workpiece supplies an upper bound to the actual rate of work done by the surface tractions. By optimization, the minimum upper bound for the total power term can be obtained.

In this study the commercial programs MathCAD and Microsoft Excel are used to get optimum $P_m$ and to plot the results. The free parameters to be optimized are $b^*$ and $c^*$.

In this case, $R^* = \frac{R}{a} = 2$ which is the real ratio of $R$ to $a$ for the indenter which is used throughout finite element analyses and experiments.

First of all, the values of $b^*$ and $c^*$ which make $P_m^*$ minimum as $u$ changes are obtained. And these $b^*$ and $c^*$ are used to evaluate the power and then the force for the chosen displacement $u$.

Figure 5.7 is a plot of the optimum values of $b^*$ and $c^*$ versus $u^*$.

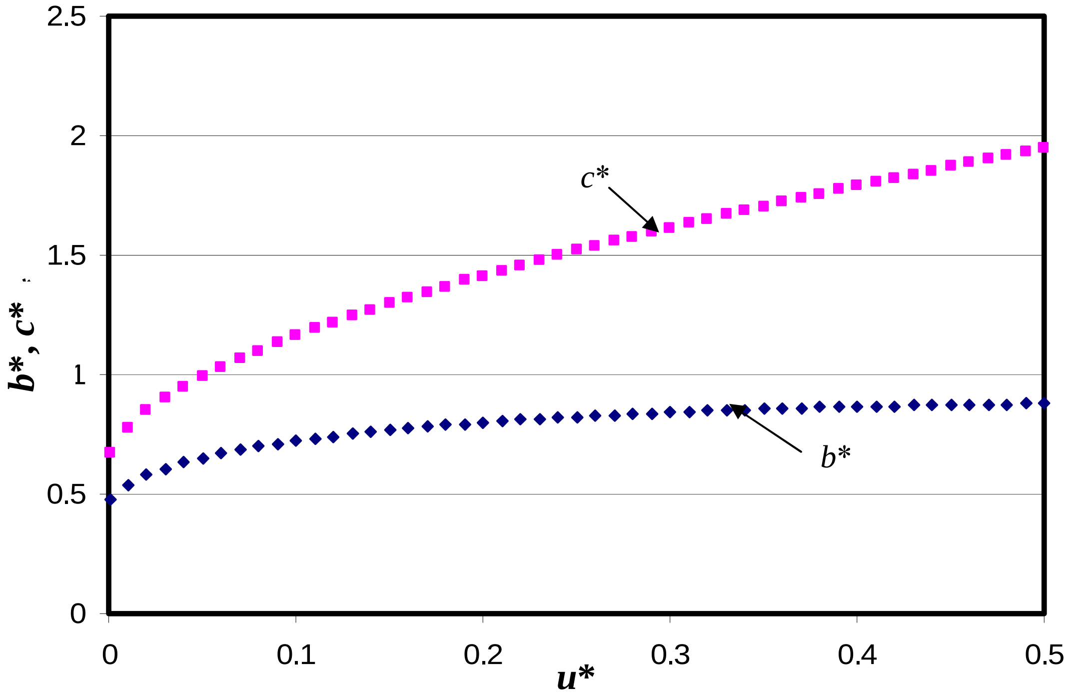


**Figure 5.7** Data points showing optimum $b^*$ and $c^*$ as functions of $u^*$

The upper bound method whose power term calculations are given in the previous sections is solved for the shear coefficient of friction m is equal to 0. On the other hand, the finite element simulation is performed with the same friction coefficient.

The finite element mesh used for the analysis is seen in Figure 5.8. A plane strain solution is applied to the model which rests on the base die and has 6319 four-node quadrilateral elements.

To be able to compare the results of upper bound method solution with the finite element results this non-dimensional power term $P_m^*$ obtained from upper bound method solution is multiplied by $\sigma_f \cdot a \cdot L$ where a non-hardening material with Young's Modulus of 80 GPa and a constant flow stress of 250 MPa is used. The result directly supplies the force since $P_m = \sigma_f \cdot \dot{u} \cdot a \cdot L$ and $F = \dfrac{P_m}{\dot{u}}$. The force-displacement data is obtained as seen in Figure 5.9.

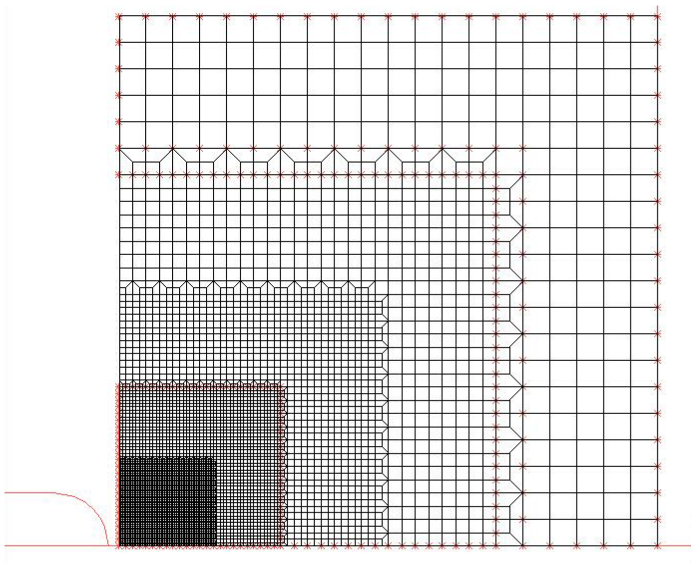

**Figure 5.8** Finite element mesh

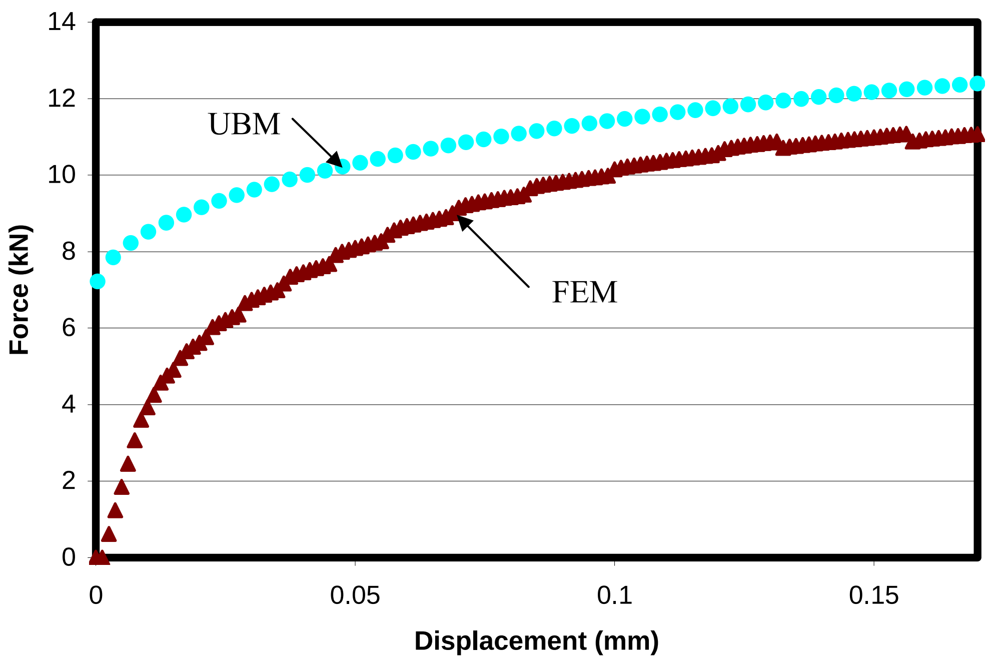


**Figure 5.9** Results of UBM and FEM

## 5.3 Upper Bound Model II

### 5.3.1 Problem and Model Description

The second model is quite similar to the first model. The only difference is that the area underneath the indenter radius is divided into two areas. It is assumed that this way a better approximation especially from the radius point of view will be achieved. This second model, the velocity field and discontinuity field it represents is seen in Figure 5.10.

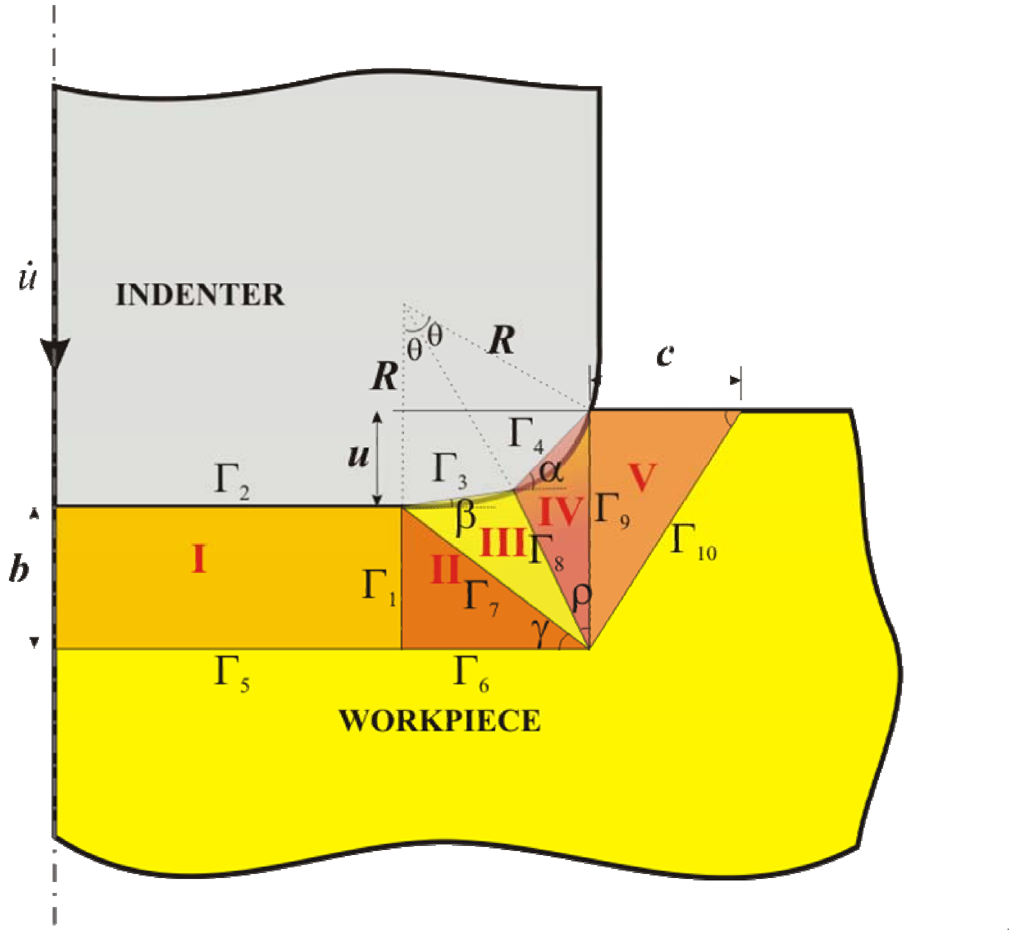


**Figure 5.10** Upper bound model of plane strain indentation (Model II)

### 5.3.2 Basic Assumptions and Approximations

The basic assumptions are the same as previous model. Only the radius of the indenter is approximated by two lines instead of one. The areas under the radius of the indenter are determined by an angle bisector which bisects the angle facing the arc of the radius in the material for that displacement, so the arc is also bisected.

### 5.3.3 Velocity Fields and Determination of Velocity Components

Only Area I can deform as in the previous model, and in this area x and y components of velocity are assumed to be $\dot{u}_x = \dot{u}_x(x)$ and $\dot{u}_y = \dot{u}_y(y)$. The velocity fields are considered to be uniform in Areas II, III, IV and V. These areas behave as rigid blocks. With those in hand, the velocity components are calculated as for the previous model.

#### 5.3.3.1 Velocity Field of Area I

The velocity components of this area are the same as those for the previous model. Please see Eqn.s (5.1) and (5.2).

#### 5.3.3.2 Velocity Field of Area II

In this area the velocity components are also the same as in the previous model since the shear surfaces and velocity components perpendicular to these surfaces are the same. The y-component of velocity is already equal to 0 since on $\Gamma_6$ surface there is no perpendicular velocity to Area II which means there is no motion in y direction. See Eqn. (5.12) for velocity of Area II.

### 5.3.3.3 Velocity Field of Area III

Two equations with two unknowns are obtained from the equations written for velocity continuities on surfaces $\Gamma_3$ and $\Gamma_7$. These are as follows:

$$\dot{u} \cdot \cos\beta = \dot{u}_{IIIx} \cdot \sin\beta - \dot{u}_{IIIy} \cdot \cos\beta \qquad (5.66)$$

$$\dot{u}_{IIx} \cdot \sin\gamma = \dot{u}_{IIIx} \cdot \sin\gamma + \dot{u}_{IIIy} \cdot \cos\gamma \qquad (5.67)$$

When both sides of Eqn. (5.66) are simplified by $\cos\beta$ and Eqn. (5.67) by $\cos\gamma$ the following equations are obtained:

$$\dot{u} = \dot{u}_{IIIx} \cdot \tan\beta - \dot{u}_{IIIy} \qquad (5.68)$$

$$\dot{u}_{IIx} \cdot \tan\gamma = \dot{u}_{IIIx} \cdot \tan\gamma + \dot{u}_{IIIy} \qquad (5.69)$$

which yield x and y components of velocity as:

$$\dot{u}_{IIIx} = \frac{\dot{u}_{IIx} \cdot \tan\gamma + \dot{u}}{\tan\gamma + \tan\beta} \qquad (5.70)$$

$$\dot{u}_{IIIy} = \dot{u}_{IIIx} \cdot \tan\beta - \dot{u} \qquad (5.71)$$

### 5.3.3.4 Velocity Field of Area IV

The same method is used to determine the velocity components of this area. The velocity continuities on surfaces $\Gamma_4$ and $\Gamma_8$ result in the following equations.

$$\dot{u}_{IIIx} \cdot \cos\rho + \dot{u}_{IIIy} \cdot \sin\rho = \dot{u}_{IVx} \cdot \cos\rho + \dot{u}_{IVy} \cdot \sin\rho \qquad (5.72)$$

$$\dot{u}\cdot\cos\alpha=\dot{u}_{IVx}\cdot\sin\alpha-\dot{u}_{IVy}\cdot\cos\alpha \tag{5.73}$$

If both sides of Eqn. (5.72) are simplified by $\sin\rho$ and Eqn. (5.73) by $\cos\alpha$, the equations become:

$$\frac{\dot{u}_{IIIx}}{\tan\rho}+\dot{u}_{IIIy}+\dot{u}=\frac{\dot{u}_{IVx}}{\tan\rho}+\dot{u}_{IVy} \tag{5.74}$$

$$\dot{u}=\dot{u}_{IVx}\cdot\tan\alpha-\dot{u}_{IVy} \tag{5.75}$$

When Eqns. (5.74) and (5.75) are added side by side, only $\dot{u}_{IVx}$ term remains and as a result the velocity components of area IV are obtained as:

$$\dot{u}_{IVx}=\frac{\dfrac{\dot{u}_{IIIx}}{\tan\rho}+\dot{u}_{IIIy}+\dot{u}}{\dfrac{1}{\tan\rho}+\tan\alpha} \tag{5.76}$$

$$\dot{u}_{IVy}=\dot{u}_{IVx}\cdot\tan\alpha-\dot{u} \tag{5.77}$$

#### 5.3.3.5 Velocity Field of Area V

The velocity of this area is parallel to the surface $\Gamma_4$ and its x component is equal to the x component of velocity of Area IV which is a result of velocity continuity on surface $\Gamma_9$.

Then, the velocity components are written as follows:

$$\dot{u}_{Vx}=\dot{u}_{IVx} \tag{5.78}$$

$$\dot{u}_{Vy}=\dot{u}_{IVx}\cdot\frac{b+u}{c} \tag{5.79}$$

$$\dot{u}_V = \dot{u}_{IVx} \cdot \frac{\sqrt{(b+u)^2 + c^2}}{c} \tag{5.80}$$

### 5.3.4 Geometry Analysis of Model II

The geometrical relations for this model are determined referring to the Figure 5.11.

The dimensions $l$ and $s$ are calculated by using Pythagoras' theorem as in Eqn.s (5.81) and (5.82).

$$l = \sqrt{R^2 - (R-u)^2} = \sqrt{2 \cdot R \cdot u - u^2} \tag{5.81}$$

$$s = \sqrt{l^2 + u^2} = \sqrt{2 \cdot R \cdot u - u^2 + u^2} = \sqrt{2 \cdot R \cdot u} \tag{5.82}$$

The angles are determined using their tangent values. They are as given form Eqn. (5.83) to Eqn. (5.91).

$$\tan\theta = \frac{s/2}{\sqrt{R^2 - \left(\frac{s}{2}\right)^2}} = \frac{\sqrt{u}}{\sqrt{2 \cdot R - u}} \tag{5.83}$$

$$\theta = \arctan \frac{\sqrt{u}}{\sqrt{2 \cdot R - u}} \tag{5.84}$$

$$\tan\beta = \frac{R - R \cdot \cos\theta}{\sqrt{R^2 - R^2 \cdot \cos^2\theta}} = \frac{\sqrt{1-\cos\theta}}{\sqrt{1+\cos\theta}} \tag{5.85}$$

$$\beta = \arctan \sqrt{\frac{1-\cos\theta}{1+\cos\theta}} \tag{5.86}$$

$$\tan\alpha = \frac{u-(R-R\cdot\cos\theta)}{l-k} = \frac{u-R+R\cdot\cos\theta}{\sqrt{2\cdot R\cdot u-u^2}-R\cdot\sin\theta} \tag{5.87}$$

$$\alpha = \arctan\frac{u-R+R\cdot\cos\theta}{\sqrt{2\cdot R\cdot u-u^2}-R\cdot\sin\theta} \tag{5.88}$$

$$\tan\gamma = \frac{b}{l} = \frac{b}{\sqrt{2\cdot R\cdot u-u^2}} \tag{5.89}$$

$$\gamma = \arctan\frac{b}{\sqrt{2\cdot R\cdot u-u^2}} \tag{5.90}$$

$$\tan\rho = \frac{l-k}{b+(R-R\cdot\cos\theta)} = \frac{\sqrt{2\cdot R\cdot u-u^2}-R\cdot\sin\theta}{b+R-R\cdot\cos\theta} \tag{5.91}$$

$$\rho = \arctan\frac{\sqrt{2\cdot R\cdot u-u^2}-R\cdot\sin\theta}{b+R-R\cdot\cos\theta} \tag{5.92}$$

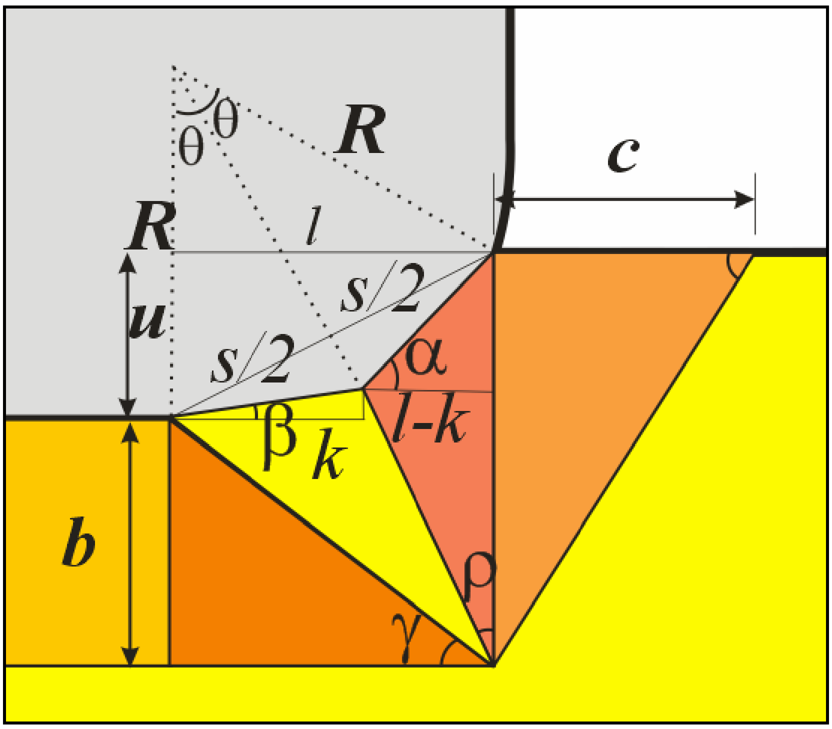


**Figure 5.11** Geometry and angle analysis for Model II

### 5.3.5 Determination of Power Terms

The total rate of work is calculated as it was explained in part 5.2.5 for this model.

*Area I*

The energy dissipation caused by the relative velocity between tool surface and workpiece is as given in Eqn. (5.28) since the velocity field and area is the same as in the previous model.

The rate of energy dissipation due to shearing of the material on surface $\Gamma_5$ and the deformation power are also the same as in Eqns. (5.29) and (5.30).

*Area II*

The power terms $P_{\Gamma 1}$ and $P_{\Gamma 6}$ are the same as calculated in part 5.2.4.2 since the contact surfaces, areas and velocity fields are the same. So, one should refer to Eqns. (5.31) and (5.34) respectively.

*Area III*

The power caused by friction between the tool and workpiece on surface $\Gamma_3$ is calculated as:

$$P_{fr} = m \cdot \frac{\sigma_f}{\sqrt{3}} \cdot \int_{A_{fr}} \left|\Delta \dot{u}_t\right| \cdot dA_{fr} \tag{5.93}$$

The relative tangential velocity on this surface is:

$$\left|\Delta \dot{u}_t\right| = \left|\dot{u} \cdot \sin\beta + \dot{u}_{IIIx} \cdot \cos\beta + \dot{u}_{IIIy} \cdot \sin\beta\right| \tag{5.94}$$

$$P_{fr3} = m \cdot \frac{\sigma_f}{\sqrt{3}} \cdot \left| \dot{u} \cdot \sin\beta + \dot{u}_{IIIx} \cdot \cos\beta + \dot{u}_{IIIy} \cdot \sin\beta \right| \cdot R \cdot \frac{\sin\theta}{\cos\beta} \cdot L \qquad (5.95)$$

On $\Gamma_7$ surface the relative tangential velocity is as follows:

$$\left|\Delta\dot{u}_t\right| = \left| \dot{u}_{IIIx} \cdot \cos\gamma - \dot{u}_{IIIy} \cdot \sin\gamma - \dot{u}_{IIx} \cdot \cos\gamma \right| \qquad (5.96)$$

Then,

$$P_{\Gamma 7} = \frac{\sigma_f}{\sqrt{3}} \cdot \left| \dot{u}_{IIIx} \cdot \cos\gamma - \dot{u}_{IIIy} \cdot \sin\gamma - \dot{u}_{IIx} \cdot \cos\gamma \right| \cdot \sqrt{2 \cdot R \cdot u - u^2 + b^2} \cdot L \qquad (5.97)$$

where $$A_{\Gamma 7} = \sqrt{2 \cdot R \cdot u - u^2 + b^2} \cdot L \qquad (5.98)$$

And since $\dot{\bar{\varepsilon}} = 0$, for deformation power Eqn. (5.99) holds.

$$P_{DIII} = 0 \qquad (5.99)$$

*Area IV*

For the $\Gamma_8$ surface power dissipated due to shearing of the material is formulated as follows:

First, the relative tangential velocity is found as:

$$\left|\Delta\dot{u}_t\right| = \left| \dot{u}_{IVx} \cdot \sin\rho - \dot{u}_{IVy} \cdot \cos\rho - \dot{u}_{IIIx} \cdot \sin\rho + \dot{u}_{IIIy} \cdot \cos\rho \right| \qquad (5.100)$$

Area of the surface is:

$$A_{\Gamma 8} = \frac{l-k}{\sin\rho} \cdot L = \frac{\sqrt{2 \cdot R \cdot u - u^2} - R \cdot \sin\theta}{\sin\rho} \cdot L \qquad (5.101)$$

Then,

$$P_{\Gamma 8} = \frac{\sigma_f}{\sqrt{3}} \cdot \left| \dot{u}_{IVx} \cdot \sin\rho - \dot{u}_{IVy} \cdot \cos\rho - \dot{u}_{IIIx} \cdot \sin\rho + \dot{u}_{IIIy} \cdot \cos\rho \right| \cdot A_{\Gamma 8} \tag{5.102}$$

To find the power dissipated by friction between the tool and workpiece for the $\Gamma_4$ surface, the relative velocity is found as follows:

$$\left|\Delta \dot{u}_t\right| = \left| \dot{u} \cdot \sin\alpha + \dot{u}_{IVx} \cdot \cos\alpha + \dot{u}_{IVy} \cdot \sin\alpha \right| \tag{5.103}$$

$$A_{\Gamma 4} = R \cdot \frac{\sin\theta}{\cos\beta} \cdot L \tag{5.104}$$

$$P_{fr4} = m \cdot \frac{\sigma_f}{\sqrt{3}} \cdot \left| \dot{u} \cdot \sin\alpha + \dot{u}_{IVx} \cdot \cos\alpha + \dot{u}_{IVy} \cdot \sin\alpha \right| \cdot R \cdot \frac{\sin\theta}{\cos\beta} \cdot L \tag{5.105}$$

$$P_{DIV} = 0 \text{ since } \dot{\bar{\varepsilon}} = 0 \tag{5.106}$$

### *Area V*

There are the shear power components on surfaces $\Gamma_9$ and $\Gamma_{10}$ to be calculated using the velocity field in this area.

On the $\Gamma_9$ surface the relative tangential velocity is simply the difference between the y-components of velocity fields in areas III and IV.

$$\left|\Delta \dot{u}_t\right| = \left| \dot{u}_{IVy} - \dot{u}_{Vy} \right| \tag{5.107}$$

$$A_{\Gamma 9} = (b + u) \cdot L \tag{5.108}$$

$$P_{\Gamma 9} = \frac{\sigma_f}{\sqrt{3}} \cdot \left| \dot{u}_{IVy} - \dot{u}_{Vy} \right| \cdot (b + u) \cdot L \tag{5.109}$$

For shear power dissipated on $\Gamma_{10}$ surface the velocity of area V is used since the relative velocity on this surface is $|\dot{u}_V|$ itself. Then,

$$P_{\Gamma 10} = \frac{\sigma_f}{\sqrt{3}} \cdot |\dot{u}_V| \cdot \sqrt{(b+u)^2 + c^2} \cdot L \tag{5.110}$$

### 5.3.6 Non-Dimensional Power Terms

The dimensionless parameters used are same as the previous model.

Dividing all terms by $\sigma_f \cdot \dot{u} \cdot a \cdot L$ and also writing *u, R, b, c* in form of $u^*$, $R^*$, $b^*$, $c^*$ by simplifying with *a*, the non-dimensional power terms are obtained.

$$P^*_{fr1} = m \cdot \frac{a}{2\sqrt{3} \cdot b} = \frac{m}{2\sqrt{3} \cdot b^*} \tag{5.111}$$

$$P^*_{\Gamma 5} = \frac{a}{2\sqrt{3} \cdot b} = \frac{1}{2\sqrt{3} \cdot b^*} \tag{5.112}$$

$$P^*_{DI} = \frac{2}{\sqrt{3}} \tag{5.113}$$

As for Area I, power terms obtained using the velocity field in Area II are non-dimensionalized.

$$P^*_{\Gamma 6} = \frac{\sqrt{2 \cdot R \cdot u - u^2}}{b \cdot \sqrt{3}} = \frac{\sqrt{2 \cdot R^* \cdot a \cdot u^* \cdot a - u^{*2} \cdot a^2}}{b^* \cdot a \cdot \sqrt{3}} = \frac{\sqrt{2 \cdot R^* \cdot u^* - u^{*2}}}{b^* \cdot \sqrt{3}} \tag{5.114}$$

$$P^*_{DII} = 0 \quad (\dot{\varepsilon} = 0) \tag{5.115}$$

$$P^*_{\Gamma 1} = \frac{b^*}{2\sqrt{3}} \tag{5.116}$$

For the rest of the power terms, for simplicity, first, the velocity fields are simplified by $\dot{u}$ since this term in the power comes from the velocity component. Then, the power term is divided by $\sigma_f \cdot a \cdot L$. So, the velocity components are obtained as follows:

$$\dot{u}^*_{IIx} = \frac{1}{b^*} \tag{5.117}$$

$$\dot{u}^*_{IIIx} = \frac{\dot{u}^*_{IIx} \cdot \tan\gamma + 1}{\tan\gamma + \tan\beta} \tag{5.118}$$

$$\dot{u}^*_{IIIy} = \dot{u}^*_{IIIx} \cdot \tan\beta - 1 \tag{5.119}$$

$$\dot{u}^*_{IVx} = \frac{\dfrac{\dot{u}^*_{IIIx}}{\tan\rho} + \dot{u}^*_{IIIy} + 1}{\dfrac{1}{\tan\rho} + \tan\alpha} \tag{5.120}$$

$$\dot{u}^*_{IVy} = \dot{u}^*_{IVx} \cdot \tan\alpha - 1 \tag{5.121}$$

$$\dot{u}^*_{Vy} = \dot{u}^*_{IVx} \cdot \frac{b^* + u^*}{c^*} \tag{5.122}$$

$$\dot{u}^*_{V} = \dot{u}^*_{IVx} \cdot \frac{\sqrt{\left(b^* + u^*\right)^2 + c^{*2}}}{c^*} \tag{5.123}$$

And the dimensionless power terms are:

$$P_{fr3}^{*} = \frac{m}{\sqrt{3}} \cdot \left| \sin\beta + \dot{u}_{IIIx}^{*} \cdot \cos\beta + \dot{u}_{IIIy}^{*} \cdot \sin\beta \right| \cdot \frac{R \cdot \sin\theta}{\cos\beta} \tag{5.124}$$

$$P_{\Gamma 7}^{*} = \frac{1}{\sqrt{3}} \cdot \left| \dot{u}_{IIIx}^{*} \cdot \cos\gamma - \dot{u}_{IIIy}^{*} \cdot \sin\gamma - \dot{u}_{IIx} \cdot \cos\gamma \right| \cdot \sqrt{2 \cdot R^{*} \cdot u^{*} - u^{*2} + b^{*2}} \tag{5.125}$$

$$P_{DIII}^{*} = 0 \quad (\dot{\bar{\varepsilon}} = 0) \tag{5.126}$$

$$P_{\Gamma 8}^{*} = \frac{1}{\sqrt{3}} \cdot \left| \dot{u}_{IVx}^{*} \cdot \sin\rho - \dot{u}_{IVy}^{*} \cdot \cos\rho - \dot{u}_{IIIx}^{*} \cdot \sin\rho + \dot{u}_{IIIy}^{*} \cdot \cos\rho \right| \cdot \frac{\sqrt{2 \cdot R^{*} \cdot u^{*}} - R^{*} \cdot \sin\theta}{\sin\rho} \tag{5.127}$$

$$P_{fr4}^{*} = \frac{m}{\sqrt{3}} \cdot \left| \sin\alpha + \dot{u}_{IVx}^{*} \cdot \cos\alpha + \dot{u}_{IVy}^{*} \cdot \sin\alpha \right| \cdot R^{*} \cdot \frac{\sin\theta}{\cos\beta} \tag{5.128}$$

$$P_{DIV}^{*} = 0 \quad (\dot{\bar{\varepsilon}} = 0) \tag{5.129}$$

$$P_{\Gamma 9}^{*} = \frac{1}{\sqrt{3}} \cdot \left| \dot{u}_{IVy}^{*} - \dot{u}_{Vy}^{*} \right| \cdot \left( b^{*} + u^{*} \right) \tag{5.130}$$

$$P_{\Gamma 10}^{*} = \frac{1}{\sqrt{3}} \cdot \left| \dot{u}_{V}^{*} \right| \cdot \sqrt{\left( b^{*} + u^{*} \right)^{2} + c^{*2}} \tag{5.131}$$

The angles in terms of dimensionless parameters are:

$$\theta = \arctan \frac{\sqrt{u^{*}}}{\sqrt{2 \cdot R^{*} - u^{*}}} \tag{5.132}$$

$$\beta = \arctan \sqrt{\frac{1 - \cos\theta}{1 + \cos\theta}} \tag{5.133}$$

$$\alpha = \arctan \frac{u^* - R^* + R^* \cdot \cos\theta}{\sqrt{2 \cdot R^* \cdot u^* - u^{*2}} - R^* \cdot \sin\theta} \tag{5.134}$$

$$\gamma = \arctan \frac{b^*}{\sqrt{2 \cdot R^* \cdot u^* - u^{*2}}} \tag{5.135}$$

$$\rho = \arctan \frac{\sqrt{2 \cdot R^* \cdot u^* - u^{*2}} - R^* \cdot \sin\theta}{b^* + R^* - R^* \cdot \cos\theta} \tag{5.136}$$

### 5.3.7 Force-Displacement Data

In this part, the same method as in part 5.2.7 is followed to obtain the lowest upper bound for the indentation force.

Again, the values of $b^*$ and $c^*$ which make $P_m^*$ minimum as $u$ changes are obtained and these $b^*$ and $c^*$ are used to evaluate the power and then the force for the chosen displacement $u$. Their values are given in Figure 5.12.

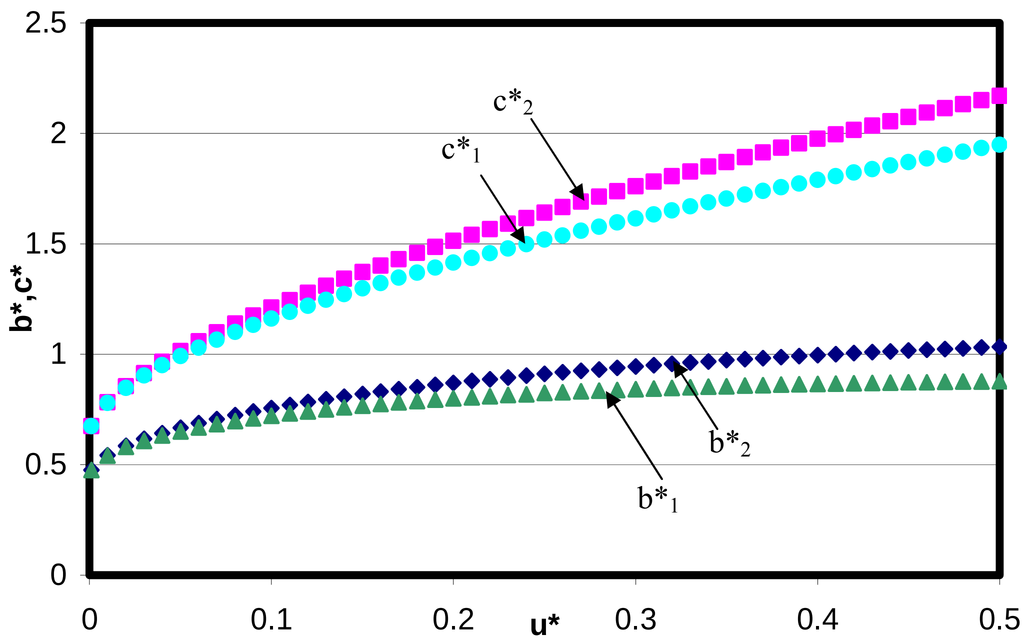


**Figure 5.12** Data points showing optimum $b^*$ and $c^*$ as functions of $u^*$

Figure 5.13 gives force-displacement data obtained by the finite element simulation, upper bound Model I and upper bound Model II.

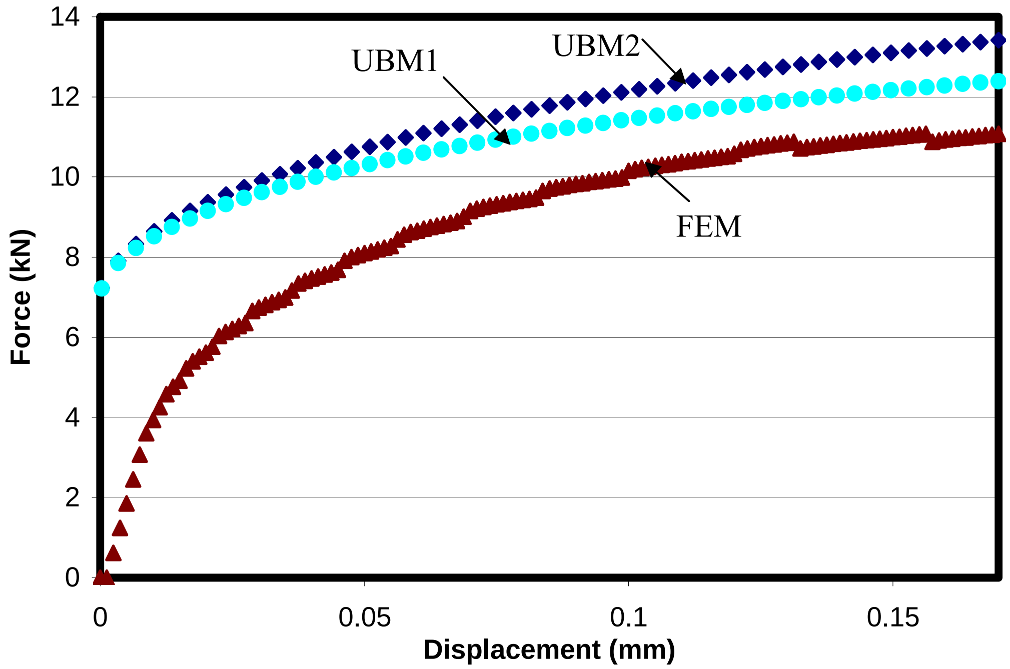


**Figure 5.13** Results of UBM1, UBM2 and FEM

## 5.4 Conclusions

In Figure 5.13, the graphs of two upper bound method solutions and finite element method are seen. The upper bound method gives force values higher than the finite element results as expected. When finite element method and upper bound method are compared finite element method can be considered as very close to the real case. The percent difference between the first upper bound method results and the finite element result is 12.4 % at 0.1 mm displacement of the indenter and it is 27.4 % at 0.5 mm displacement of the indenter. This decrease in percent difference as the indenter penetrates into the material could be a result of approximation of the radius by a line. The most prominent effect on the upper bound method results is the selection of the velocity field in the workpiece.

In order to get results closer to finite element method results a second model is used for upper bound solution. The second model is also used to get the force-displacement curve when shear coefficient of friction m is equal to 0. The results are compared with the previous model and the finite element method results.

This model was expected to be a better pattern of deformation in the sense that it represents the radius with two lines. With this idea in mind, lower force values compared with the results of first model are expected. But the new model yields to higher force values.

# CHAPTER 6

# EXPERIMENTAL STUDY

## 6.1 Introduction

This chapter deals with the experimental studies on indentation, compression and tension tests. In addition to indentation tests which have been the main experimental aim of this thesis, compression and tension tests have been done in order to verify and check indentation test results.

First, the experimental setups used, their working principles and the method of the experiments will be explained. The setup is the same for indentation and compression tests and another setup is used for tension tests. The measurement systems, apparatus and method of experimentation are also explained. Next section explains properties and preparation of the specimens. Finally, the experimental results are presented.

## 6.2 Experimental Setup

Two different setups are used to perform the experiments in this thesis. The indentation and compression tests are done on the computer controlled press which has a vertically moving crosshead. The tension tests are done on a setup where the load and displacement between two points can be measured and works horizontally.

### 6.2.1 Experimental Setup for Indentation and Compression

#### 6.2.1.1 Components and Properties of the Setup

During the experiments, the press Zwick Z020 has been used. It has a maximum capacity of 2 tons. The crosshead moves vertically on two power screws on each side. Press is controlled by a computer.

The load cell measures the load and the displacement data of the crosshead of press is also collected. The load cell is able to measure in an error range of 0.01-0.08%. Either a force limit or a displacement can be defined for termination of the test. The punch speed can be controlled such that different speeds for loading and unloading or application of preload can be defined. In addition, cyclic loading can be applied. The force-displacement graphs appear on the screen while the test is being performed. The press and its computer control system are given in Figure 6.1.


**Figure 6.1** Press used for indentation and compression tests

In the experiments, instead of the displacement measurement taken from the crosshead, measurements are taken from three transducers placed by 120˚ angle to each other. The measurement system is seen in Figure 6.2.

The most important property of this system is that it can take displacement data with three displacement transducers from three points on a circular surface which is free of the applied force. This eliminates the rotational effects of the solid parts from displacement data. The experiments have also proved the necessity of such a design. With a reference plate free from the indentation forces the accuracy of the displacement measurements is increased. On the other hand, the test specimen can be fixed between the anvil and the fixing plate which prevents the rigid body motion.

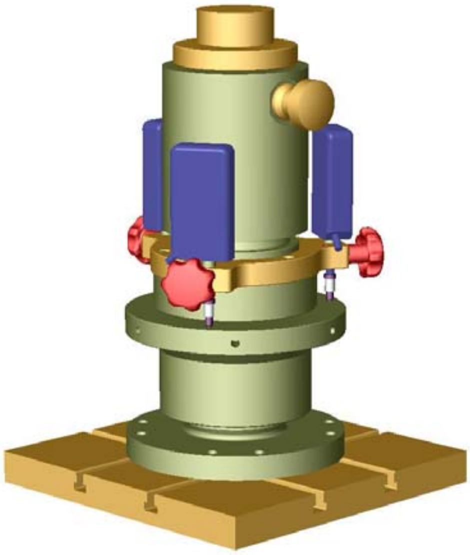

CAD-drawing

Measuring system fixed to the press

**Figure 6.2** The measuring system of indentation and compression tests

The parts of the measuring system are seen in Figure 6.3. The part holding the transducers together with the indenter is made of aluminum and it has teeth so that it is screwed to the upper part of the system. The anvil is of hardened tool steel. The specimen rests on the anvil and clamped there by the reference plate. The reference plate of the system is also made of aluminum. The reference plate has teeth so that it is screwed to the lower support of the system.

The indenter can be removed and changed depending on the process. There are three parts which can be fit in the position of indenter. They are the indenter, the centering punch and the compression punch.

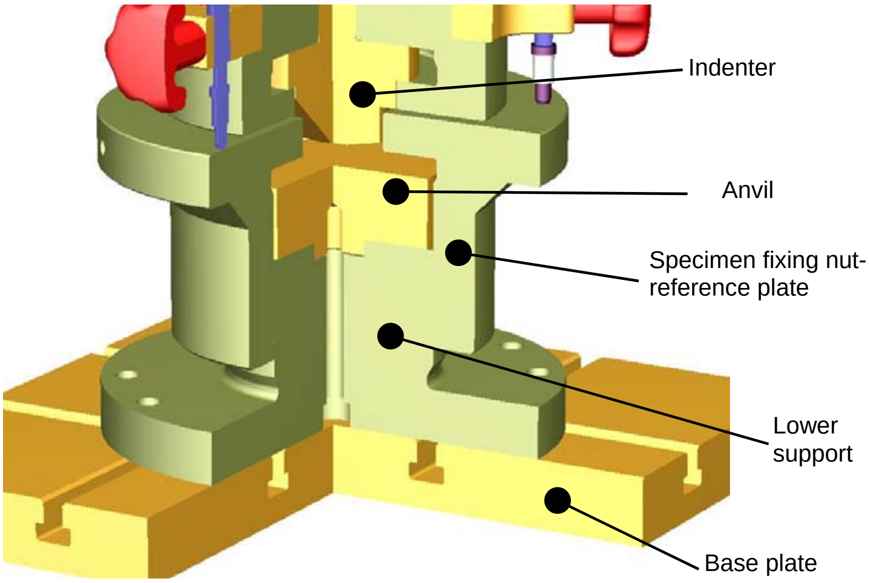


**Figure 6.3** Parts of the measuring system

The indenter used for indentation tests can be seen in Figure 6.4. It is made of diamond which is penetrated into hardened tool steel.

The indenter is fixed to the upper support of the measuring system by placing the positioning step tangential to the two support pins, so that the indenter is made sure to keep its same position when it is replaced. This also assures that the longitudinal positioning of the indenter is parallel to the horizontal axis of the cross-head.

Two types of indenters are available. The difference is the geometry of the diamond part whereas dimensions, materials and manufacturing processes of the whole indenter are same. Figure 6.5 shows these two types of indenters. Figure 6.5 (a) is the flat base indenter where the flat part is 0.68 mm and radii at two sides are also 0.68 mm. On the other hand, Figure 6.5 (b) shows the indenter with circular base.

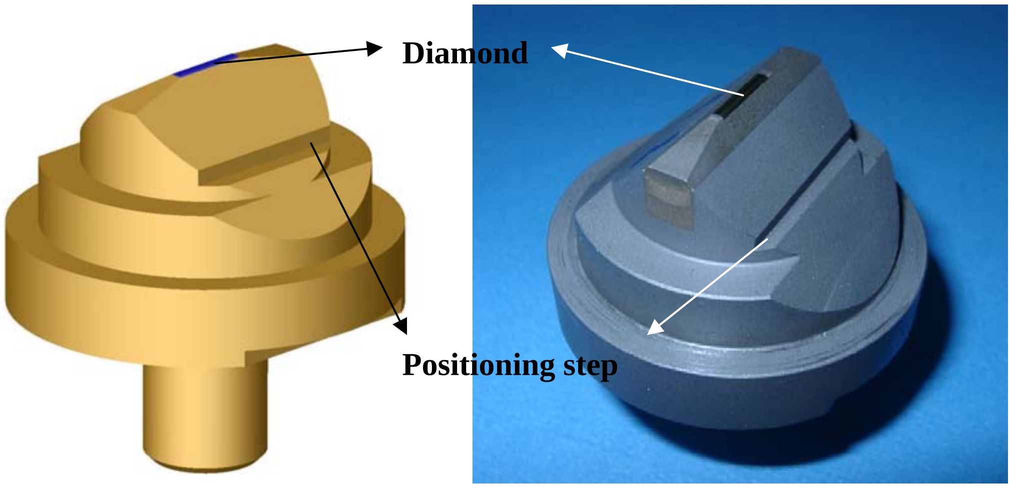


**(a)** **(b)**

**Figure 6.4** (a) CAD-drawing of indenter, (b) Photo of indenter

The indenter type used in this thesis study is the flat base indenter which is seen in Figure 6.5 (a). Some results of indenter with circular base and comparisons of both indenter test results are also given in the following parts of this chapter.

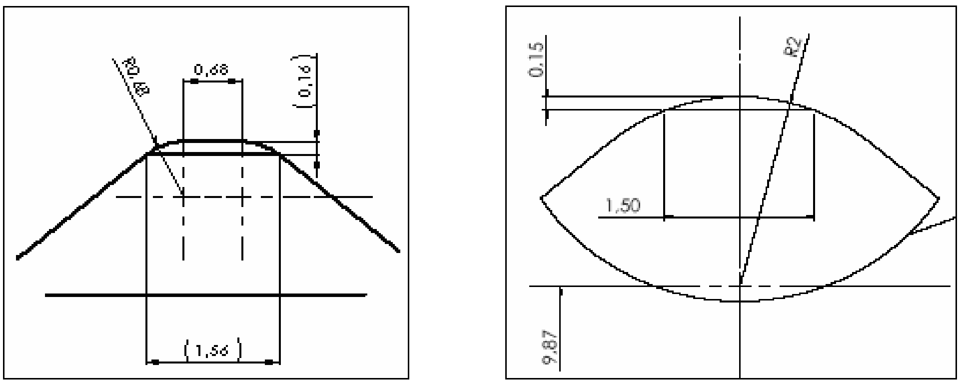


**(a)** **(b)**

**Figure 6.5** (a) Indenter with flat base ( $R = 0.68$ mm),

(b) Indenter with circular base ( $R = 2$ mm)

On the other hand, the indenter can be replaced by a punch which is used for compression tests. This punch with a flat surface is seen in Figure 6.6.

**Figure 6.6** Compression punch

### 6.2.1.2 Adjustments before Experiments

Before starting the experiments, some adjustments are needed to be done. These are to make the vertical centerlines of the indenter and the reference plate coincident and to check the parallelity between the anvil surface and the indenter or the compression punch.

For making the centers coincident, the centering punch is used. It is made of aluminum and used only for this purpose; no metal forming process can be done using this punch. Figure 6.7 shows the centering punch.

While centering, this punch is inserted in the place of the indenter seen in Figure 6.3. The nuts connecting the lower support to the base plate are loosened. Then, the upper part is lowered slowly and made fit in the hole of the reference plate. Then the nuts are tightened.

**Figure 6.7** Centering punch

Another adjustment which is the parallelity of the anvil and the indenter is made visually. The indenter is lowered till it is very close to the anvil. Then, the gap between the anvil and the indenter is observed and depending on the angle between the indenter and the anvil, the related side is raised or lowered with thin sheet metal placed between the base plate and the lower support which are seen in Figure 6.3. Figure 6.8 shows the parallelity between the anvil and the indenter.

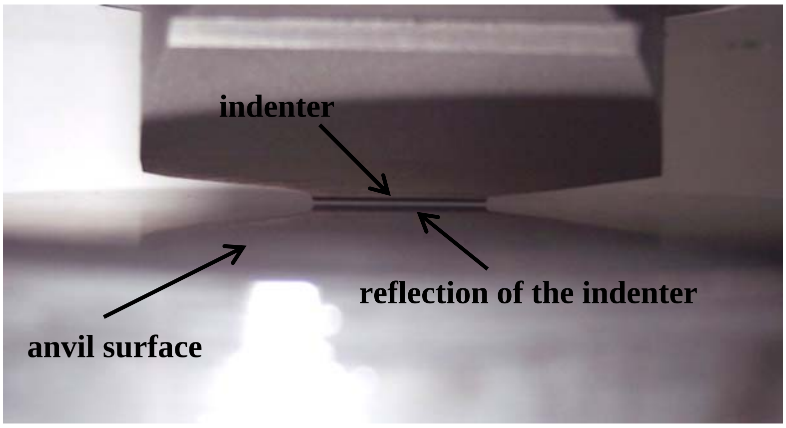


**Figure 6.8** Indenter and anvil parallelity

### 6.2.2 Experimental Setup for Tension Tests

Tension tests are done on aluminum sheet in order to check the anisotropy of the material on which indentation tests are to be done. The setup in Figure 6.9 is used for these experiments. The power screw is actuated by an electric motor and can also be controlled manually by a handle. The specimen is mounted horizontally between the grips.

Maximum load that can be carried by this setup is 2 tons. The load and gage length can be measured.

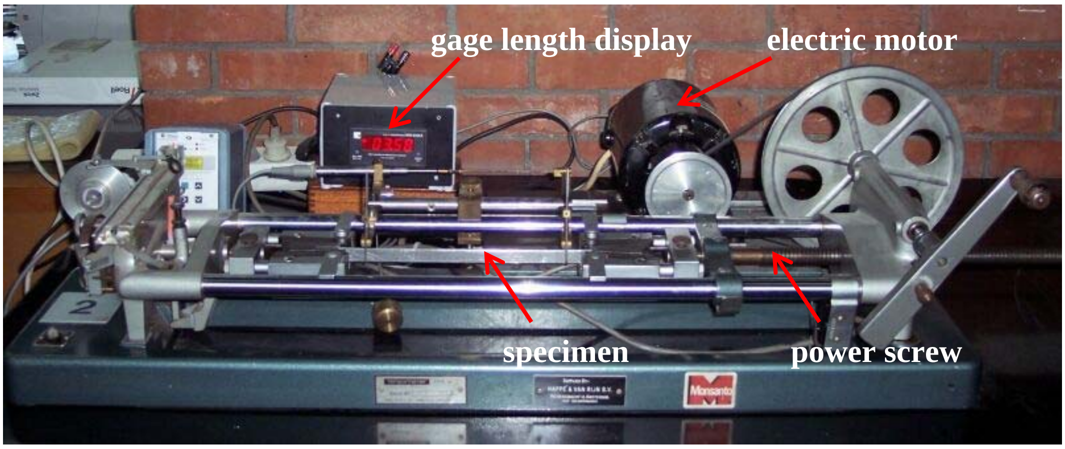


**Figure 6.9** Tension test setup

During a test specimen is elongated step by step. The elongation is controlled from the gage length display which shows a relative number for the distance between the two reference points. At the end of each step the gage lengths, thicknesses, widths are measured and a set of data is collected. Using these data strain values are calculated. Then, anisotropy values are found and plotted with respect to true strain in longitudinal direction.

## 6.3 Specimens

In this part, types and production steps of specimens in addition to their geometric properties are explained. Materials are either bought from the suppliers or received from the project partners of the Stuttgart University in semi-prepared or prepared forms.

### 6.3.1 Compression Specimens

Compression tests are done in order to check the anisotropy of the material and they have also been useful to check the measuring system elasticity and accuracy. The specimens used for compression tests are produced from bars of St37 which are seen in Figure 6.10.

These bars have cross-sections of 5x8 $mm^2$ each. Compression specimens are produced with 5x5 $mm^2$ cross-section and 8 mm height. They are cut using a round saw connected to the milling machine. Specimens of 4 mm and 5 mm height are also produced and upset. The finite element analyses of these compression tests are given in Chapter 4 of this thesis and experimental results are explained in [42, Chapter 6].

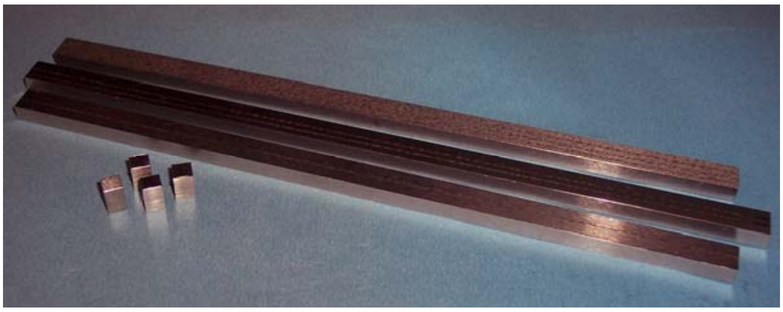

**Figure 6.10** Compression specimens of St37

Later, cylindrical specimens produced from these bars are also used in compression tests. These bars are machined by turning and then specimens of 5 mm are cut from these bars.

### 6.3.2 Tension Specimens

The tension specimens are produced from the aluminum alloy Al5086 in three directions with respect to rolling in 0˚, 90˚ and 45˚ directions. They are cut as strips from the sheet. They are first cut using the shear blade and then machined to have constant area through the length.

Machining was necessary since while cutting, the blade leaves a surface at an angle different form 90˚ to the upper and lower surfaces. This causes not only an inhomogeneous area distribution but also prevents the accuracy of measurements of width using the micrometer.

Figure 6.11 is a photo of one of the test strips. The vernier caliper marks and the centerline mark are seen in that figure also. The longitudinal elongation is measured using the calipers and the width contraction is measured each time at the center mark by a micrometer.

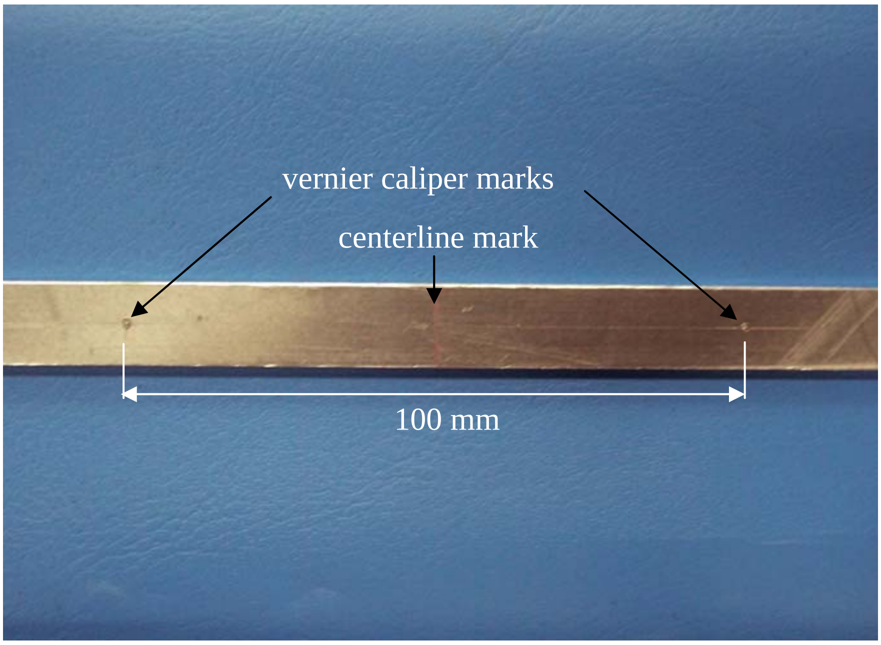


**Figure 6.11** Tensile test specimen

### 6.3.3 Indentation Specimens

The specimens used in first experiments are produced from the aluminum plate which has a thickness of 16 mm. In deciding the material of specimen the capacity of the press and the indenter is considered, whereas the dimensions of the anvil and fixing plate are considered for the specimen dimensions, later the finite element analysis results have played important role to determine the dimensions. The analyses have proven that the specimen dimensions affect the force-displacement curves and after some dimension saturation of these curves is reached. These analyses are seen in [42, Chapter 4]. The material used is Al2014 plate which is known to be cold rolled.  On this plate, the rolling direction is determined visually since the grain orientations are visible and specimens are prepared in rolling and perpendicular to rolling direction.

Two groups of these specimens are produced; some are produced in the machine shop at Department of Mechanical Engineering of Middle East Technical University. For better surface quality requirements some parts are ground at the ORS bearing company since the needed equipment is not available in the above mentioned machine shop.

Figure 6.12, shows one typical specimen produced from Al2014 where the dimensions are also given.

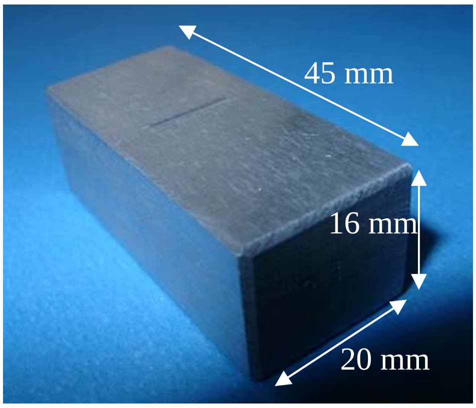


**Figure 6.12** Al2014 specimen

In addition, some indentation specimens of Al5086 sheet are produced. The anisotropy of this material can be checked by tension tests and compared with indentation tests.

On this sheet of Al5086, the rolling direction is visible. Knowing the rolling direction of the material, specimens in rolling and perpendicular to rolling direction are prepared.

A specimen of Al5086 is seen in Figure 6.13. Same dimensions as Al2014 have been used in length and width directions, but thickness is 3.2 mm in this case. The line in the middle of the specimen is drawn to help correct positioning of the specimen. The specimen is placed such that the indenter imprint is on that line. The arrow on the specimen shows direction of rolling. For example, the indentation on the specimen given in Figure 6.13 is an indentation in the rolling direction.

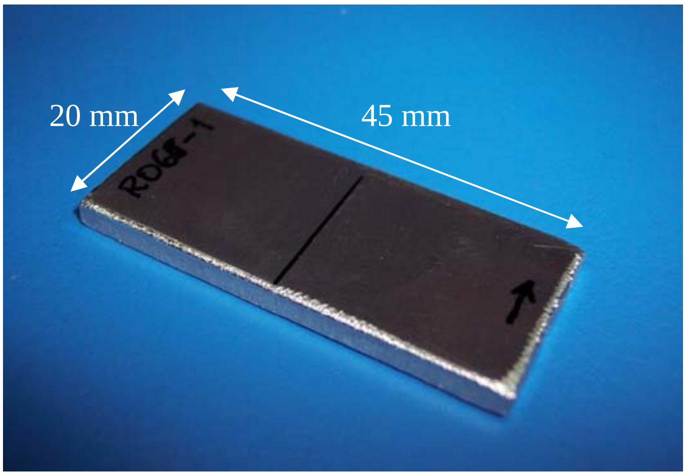


**Figure 6.13** Al5086 specimen

Since the material is thin, bending occurs easily during indentation and this causes wrong displacement measurements in the experiments. The basic issue in production was not to cause bending of the specimens. When the parts are produced from a piece of material as in Figure 6.14 (a) bending in the longitudinal direction is more and when parts are produced as in Figure 6.14 (b) this bending effect is less compared to parts produced as in (a).

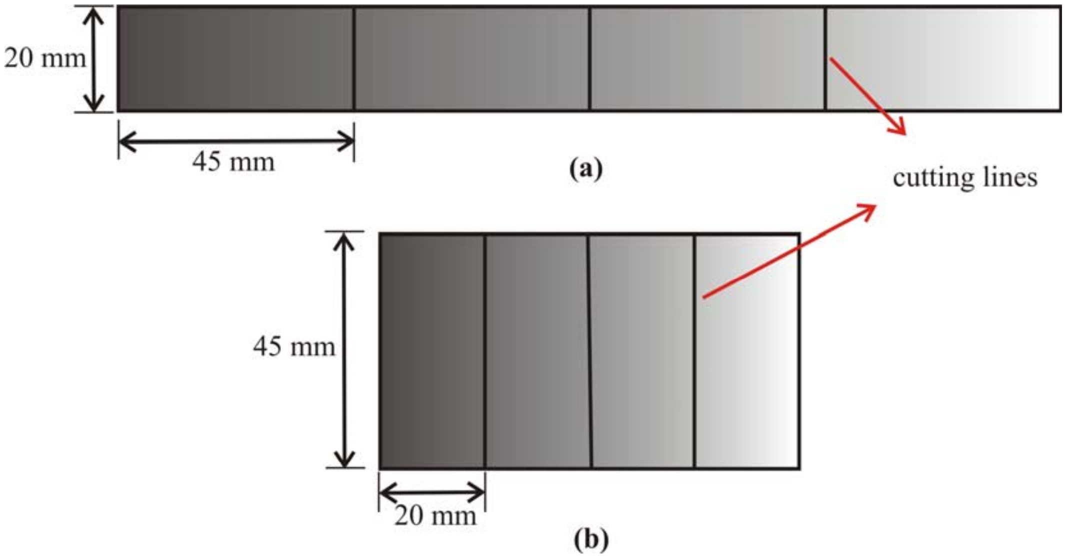


**Figure 6.14** Two different cutting sequences of sheet specimens

To avoid indentation on bent specimens, the compression punch is used to flatten the specimens before indentation. A load of 10 kN is applied to each specimen in addition to careful production steps. Figure 6.15 shows flattening of specimens using the compression punch.

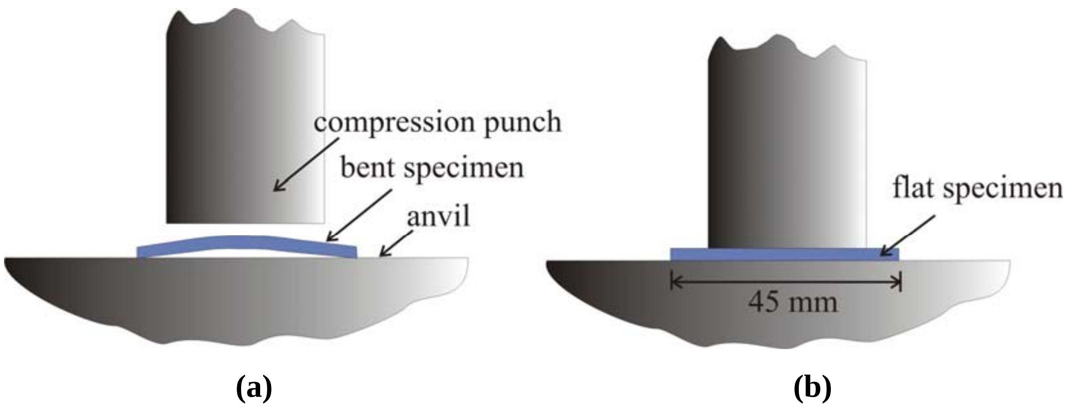


**Figure 6.15** Flattening of Al5086 specimen

The experimental results graphs contain the numbers of the specimens. Table D.1 in Appendix D gives surface properties, rolling directions and dimensions of the specimens.

### 6.3.4 Material Properties

In order to be able to observe anisotropy of the metals, rolled plates or sheets are chosen as the material of the specimens. In the experimental part of this thesis mainly two aluminum alloys are used. These are Al 2014 and Al 5086. Chemical compositions of these materials are given in Table 6.1.

**Table 6.1** Chemical composition of Al 2014 and Al5086 [51]

| **Element \ Alloy** | **Al 2014** | **Al 5086** |
|---|---|---|
| Cu | 3.9-5.0 | $\leq$ 0.10 |
| Mn | 0.40-1.2 | 0.20-0.7 |
| Si | 0.50-1.2 | $\leq$ 0.40 |
| Mg | 0.20-0.8 | 3.5-4.5 |
| Fe | $\leq$ 0.7 | $\leq$ 0.50 |
| Zn | $\leq$ 0.25 | $\leq$ 0.25 |
| Zr+Ti | $\leq$ 0.20 | - |
| Total Other | $\leq$ 0.15 | $\leq$ 0.15 |
| Ti | $\leq$ 0.15 | $\leq$ 0.15 |
| Cr | $\leq$ 0.10 | 0.05-0.25 |
| Other elements | $\leq$0.05 | $\leq$ 0.05 |
| Al | remainder | remainder |

Some of the mechanical properties of these materials are given in Table 6.2.

**Table 6.2** Some mechanical properties of Al 2014 and Al5086 [52]

| Alloy | Modulus of Elasticity E (GPa) | Initial yield strength $\sigma_{yo}$ (MPa) | Poisson's ratio $\upsilon$ |
|---|---|---|---|
| Al 2014 | 72.4 | 276 | 0.33 |
| Al 5086 | 71 | 207 | 0.33 |

## 6.4 Experimental Results

In this part, experimental results of compression tests, tension tests and indentation tests will be explained.

### 6.4.1 Compression Test Results

The need for compression tests have appeared as it has been decided to perform indentation tests to determine anisotropy of metals. When indentation tests of St37 have started with the circular base indenter [42, Chapter 5] compression tests are decided to be performed to verify and to compare the results of indentation tests with the results of compression tests.

Having specimens prepared in three orthogonal directions to rolling, the difference in the true stress-true strain curves could be observed by compression tests, if exists.

Figure 6.16 gives true stress-true strain curves for compression tests in one direction. The details of calculations and experiments are given in [42, Chapter 6]. The unexpected result of these tests was that the curves show a behavior that stresses start to decrease after some strain.

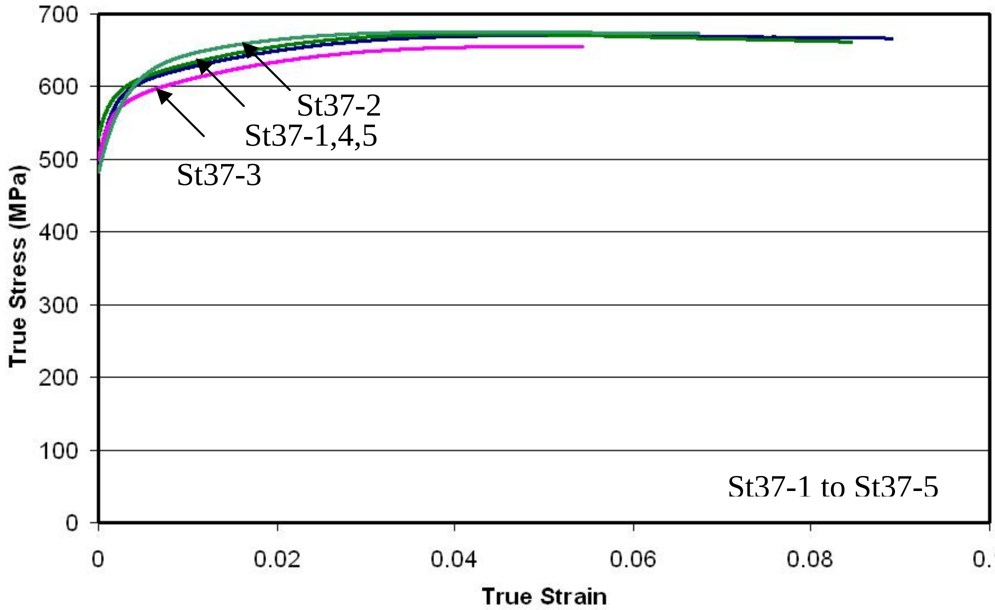


**Figure 6.16** Compression test results of prismatic specimen of St37

The reasons for such a decrease in true stress values are tried to be identified. Possible reasons could be height of the specimens, non-uniform friction at the contact between upper punch and the specimen and the lower die and the specimen.

These effects are analyzed in Chapter 4 of this thesis. More detailed experimental investigation and several experimental analyses are also given in [42, Chapter 6].

### 6.4.2 Tension Test Results

As in the case of compression tests, tension tests are done to prove if the material is anisotropic. With a 3.2 mm thick sheet of aluminum alloy it was preferred to make tension tests instead of compression. Production of the test specimens and the method of measurement are given in part 6.3.2.

In Table 6.3 and 6.4, measurement number "0" shows the initial length and width of the specimens. The measurements at each step are done after the load has been released. Using the new length and width of each measurement, the strains in length and width directions are calculated which are $\varepsilon_l = \ln \frac{l}{l_o}$ and $\varepsilon_w = \ln \frac{w}{w_o}$. Since the measurement of thickness includes considerably greater error than for length and width, strain in the thickness direction is calculated using volume constancy. Volume constancy requires:

$$\varepsilon_l + \varepsilon_w + \varepsilon_t = 0 \tag{6.1}$$

From Eqn. (6.1) $\varepsilon_t$ is calculated as:

$$\varepsilon_t = -(\varepsilon_l + \varepsilon_w) \tag{6.2}$$

Since the method of measurement using calipers and a micrometer is not so accurate as the measurement of the computer controlled press, data obtained are scattered. Figure 6.17 shows a plot of the anisotropy coefficient $r = \frac{\varepsilon_w}{\varepsilon_t}$ versus strain in the longitudinal direction $\varepsilon_l$. This result is satisfactory in that the anisotropy of the material is obvious. In addition, even with this scattered data, two sets of experiments are consistent with each other.

**Table 6.3** Tension test measurements of Al5086, set 1

| | Data | *l* (mm) | *w* (mm) | $\varepsilon_l$ | $\varepsilon_w$ | $\varepsilon_t$ | *r* |
|---|---|---|---|---|---|---|---|
| **0°** | 0 | 100.24 | 13.425 | | | | |
| | 1 | 101.58 | 13.390 | 0.0133 | -0.0026 | -0.0107 | 0.2447 |
| | 2 | 102.96 | 13.320 | 0.0268 | -0.0079 | -0.0189 | 0.4150 |
| | 3 | 103.68 | 13.248 | 0.0337 | -0.0133 | -0.0205 | 0.6484 |
| | 4 | 105.32 | 13.188 | 0.0494 | -0.0178 | -0.0316 | 0.5632 |
| | 5 | 106.54 | 13.165 | 0.0610 | -0.0196 | -0.0414 | 0.4724 |
| | 6 | 108.34 | 13.070 | 0.0777 | -0.0268 | -0.0509 | 0.5264 |
| | 7 | 108.88 | 13.070 | 0.0827 | -0.0268 | -0.0559 | 0.4796 |
| | 8 | 109.02 | 13.070 | 0.0840 | -0.0268 | -0.0572 | 0.4688 |
| **45°** | 0 | 100.10 | 13.435 | | | | |
| | 1 | 101.50 | 13.350 | 0.0139 | -0.0063 | -0.0075 | 0.8415 |
| | 2 | 102.98 | 13.250 | 0.0284 | -0.0139 | -0.0145 | 0.9563 |
| | 3 | 104.12 | 13.183 | 0.0394 | -0.0189 | -0.0204 | 0.9264 |
| | 4 | 105.48 | 13.106 | 0.0524 | -0.0248 | -0.0276 | 0.8997 |
| | 5 | 107.10 | 12.988 | 0.0676 | -0.0338 | -0.0338 | 1.0024 |
| | 6 | 108.04 | 12.982 | 0.0763 | -0.0343 | -0.0420 | 0.8160 |
| | 7 | 109.62 | 12.875 | 0.0909 | -0.0426 | -0.0483 | 0.8820 |
| | 8 | 110.38 | 12.840 | 0.0978 | -0.0453 | -0.0525 | 0.8635 |
| | 9 | 110.92 | 12.838 | 0.1026 | -0.0455 | -0.0572 | 0.7948 |
| | 10 | 112.74 | 12.668 | 0.1189 | -0.0588 | -0.0601 | 0.9776 |
| | **Data** | ***l* (mm)** | ***w* (mm)** | $\varepsilon_l$ | $\varepsilon_w$ | $\varepsilon_t$ | ***r*** |
| **90°** | 0 | 99.92 | 13.362 | | | | |
| | 1 | 101.68 | 13.270 | 0.0175 | -0.0069 | -0.0106 | 0.6548 |
| | 2 | 102.68 | 13.215 | 0.0272 | -0.0111 | -0.0162 | 0.6835 |
| | 3 | 103.54 | 13.158 | 0.0356 | -0.0154 | -0.0202 | 0.7615 |
| | 4 | 104.74 | 13.108 | 0.0471 | -0.0192 | -0.0279 | 0.6874 |
| | 5 | 106.12 | 13.051 | 0.0602 | -0.0236 | -0.0367 | 0.6426 |
| | 6 | 107.74 | 12.955 | 0.0754 | -0.0309 | -0.0444 | 0.6964 |
| | 7 | 109.40 | 12.865 | 0.0906 | -0.0379 | -0.0527 | 0.7187 |
| | 8 | 112.09 | 12.690 | 0.1149 | -0.0516 | -0.0633 | 0.8148 |
| | 9 | 114.00 | 12.685 | 0.1318 | -0.0520 | -0.0798 | 0.6513 |

**Table 6.4** Tension test measurements of Al5086, set 2

| | Data | $l$ (mm) | $w$ (mm) | $\varepsilon_l$ | $\varepsilon_w$ | $\varepsilon_t$ | $r$ |
|---|---|---|---|---|---|---|---|
| **0°** | 0 | 100.06 | 14.125 | | | | |
| | 1 | 100.58 | 14.110 | 0.0052 | -0.0011 | -0.0041 | 0.2578 |
| | 2 | 102.62 | 14.000 | 0.0253 | -0.0089 | -0.0164 | 0.5429 |
| | 3 | 102.84 | 13.970 | 0.0274 | -0.0110 | -0.0164 | 0.6740 |
| | 4 | 103.28 | 13.942 | 0.0317 | -0.0130 | -0.0186 | 0.6998 |
| | 5 | 103.84 | 13.920 | 0.0371 | -0.0146 | -0.0225 | 0.6509 |
| | 6 | 104.62 | 13.908 | 0.0446 | -0.0155 | -0.0291 | 0.5323 |
| | 7 | 105.06 | 13.850 | 0.0488 | -0.0197 | -0.0291 | 0.6756 |
| | 8 | 106.34 | 13.805 | 0.0609 | -0.0229 | -0.0380 | 0.6037 |
| | 9 | 107.12 | 13.785 | 0.0682 | -0.0244 | -0.0438 | 0.5561 |
| | 10 | 109.80 | 13.590 | 0.0929 | -0.0386 | -0.0543 | 0.7114 |
| **45°** | 0 | 100.84 | 14.167 | | | | |
| | 1 | 101.22 | 14.131 | 0.0038 | -0.0025 | -0.0063 | 0.4035 |
| | 2 | 102.96 | 14.020 | 0.0208 | -0.0104 | -0.0104 | 1.0053 |
| | 3 | 103.68 | 13.990 | 0.0278 | -0.0126 | -0.0152 | 0.8271 |
| | 4 | 104.42 | 13.905 | 0.0349 | -0.0187 | -0.0162 | 1.1509 |
| | 5 | 105.32 | 13.870 | 0.0435 | -0.0212 | -0.0223 | 0.9509 |
| | 6 | 106.38 | 13.800 | 0.0535 | -0.0262 | -0.0272 | 0.9637 |
| | 7 | 107.84 | 13.710 | 0.0671 | -0.0328 | -0.0343 | 0.9553 |
| | 8 | 108.20 | 13.690 | 0.0704 | -0.0342 | -0.0362 | 0.9462 |
| | 9 | 108.62 | 13.680 | 0.0743 | -0.0350 | -0.0393 | 0.8892 |
| | 10 | 109.60 | 13.680 | 0.0833 | -0.0350 | -0.0483 | 0.7239 |
| **90°** | 0 | 99.92 | 14.185 | | | | |
| | 1 | 100.06 | 14.170 | 0.0014 | -0.0011 | -0.0003 | 3.0925 |
| | 2 | 100.20 | 14.162 | 0.0028 | -0.0016 | -0.0012 | 1.3804 |
| | 3 | 100.46 | 14.146 | 0.0054 | -0.0028 | -0.0026 | 1.0442 |
| | 4 | 101.12 | 14.115 | 0.0119 | -0.0049 | -0.0070 | 0.7076 |
| | 5 | 101.84 | 14.078 | 0.0190 | -0.0076 | -0.0115 | 0.6606 |
| | 6 | 102.66 | 14.028 | 0.0271 | -0.0111 | -0.0159 | 0.6990 |
| | 7 | 103.08 | 13.990 | 0.0311 | -0.0138 | -0.0173 | 0.8004 |
| | 8 | 103.58 | 13.960 | 0.0360 | -0.0160 | -0.0200 | 0.8000 |
| | 9 | 104.40 | 13.908 | 0.0439 | -0.0197 | -0.0241 | 0.8170 |
| | 10 | 105.38 | 13.882 | 0.0532 | -0.0216 | -0.0316 | 0.6831 |
| | 11 | 107.16 | 13.781 | 0.0700 | -0.0289 | -0.0411 | 0.7037 |
| | 12 | 108.08 | 13.773 | 0.0785 | -0.0295 | -0.0490 | 0.6012 |
| | 13 | 109.30 | 13.700 | 0.0897 | -0.0348 | -0.0549 | 0.6333 |
| | 14 | 110.48 | 13.582 | 0.1005 | -0.0434 | -0.0570 | 0.7618 |

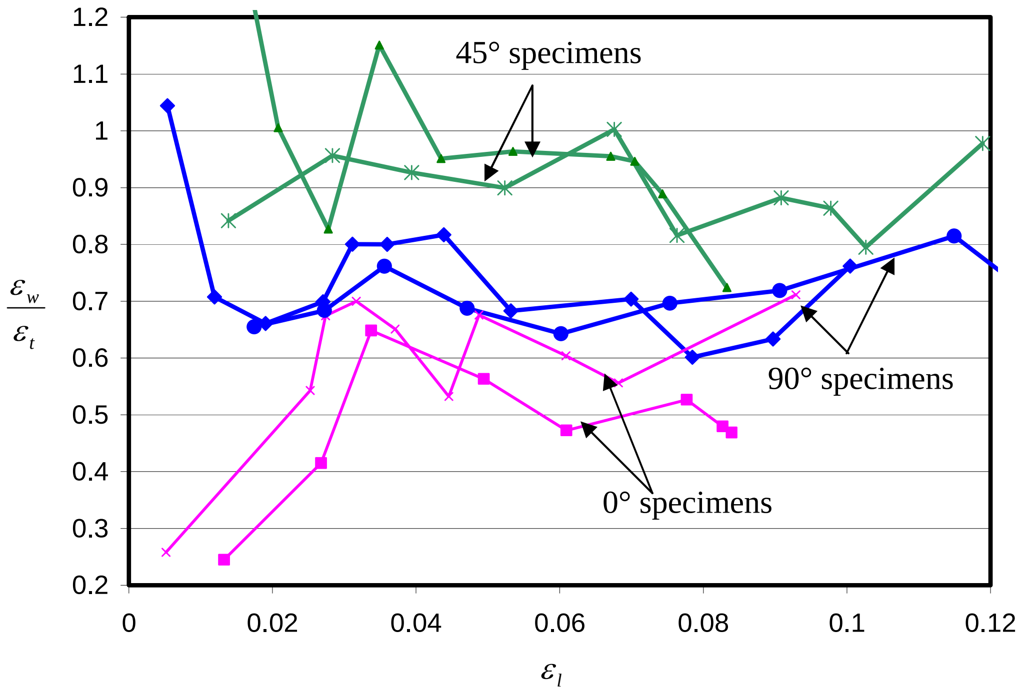


**Figure 6.17** Tension test results of Al 5086

Figure 6.17 shows that for both sets of experiments, the r-values for 0° specimens are the smallest, higher r-values are obtained for 90° specimens and 45° specimens have highest r-value.

When anisotropy values for changing angles are plotted for $\varepsilon_l = 0.02$, $\varepsilon_l = 0.05$ and $\varepsilon_l = 0.08$, Figure 6.18 is obtained. For determination of *r*-values, interpolation is used between the two closest data points. Then, the average is taken for two sets of experiments. These values are given in Table 6.5.

**Table 6.5** Normal and planar anisotropy values for Al 5086

| | $\varepsilon_l = 0.02$ | $\varepsilon_l = 0.05$ | $\varepsilon_l = 0.08$ |
|---|---|---|---|
| $r_0$ | 0.399 | 0.614 | 0.568 |
| $r_{45}$ | 0.973 | 0.932 | 0.809 |
| $r_{90}$ | 0.664 | 0.703 | 0.654 |
| $\overline{r}$ | 0.752 | 0.795 | 0.710 |
| $\Delta r$ | -0.442 | -0.273 | -0.198 |

It can be deduced from Figure 6.18 and Table 6.5 that the effect of anisotropy decreases for higher strains. This result may be useful for the indentation tests.

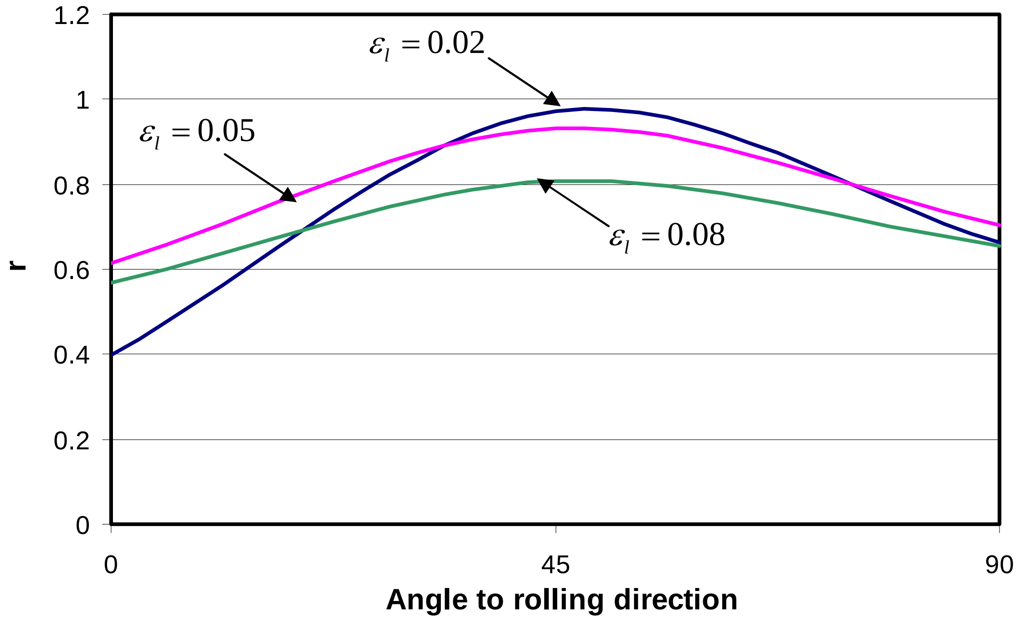


**Figure 6.18** Change of r-value with angle to rolling direction

### 6.4.3 Indentation Test Results

In this section indentation test results will be given. Various effects on force-displacement curves of indentation are investigated. The effect of surface quality, effect of triple indentations, effect of clamping, effect of the indenter geometry and the effect of anisotropy are tested.

#### 6.4.3.1 Effect of Surface Quality

Two groups of specimens from Al2014 are used for determination of effect of surface quality on force-displacement curves of indentation. Three specimens without surface processing and three specimens with ground surfaces are used. The results are as seen in Figure 6.19. The forces are higher for the ground specimens than for the ones with original surface.

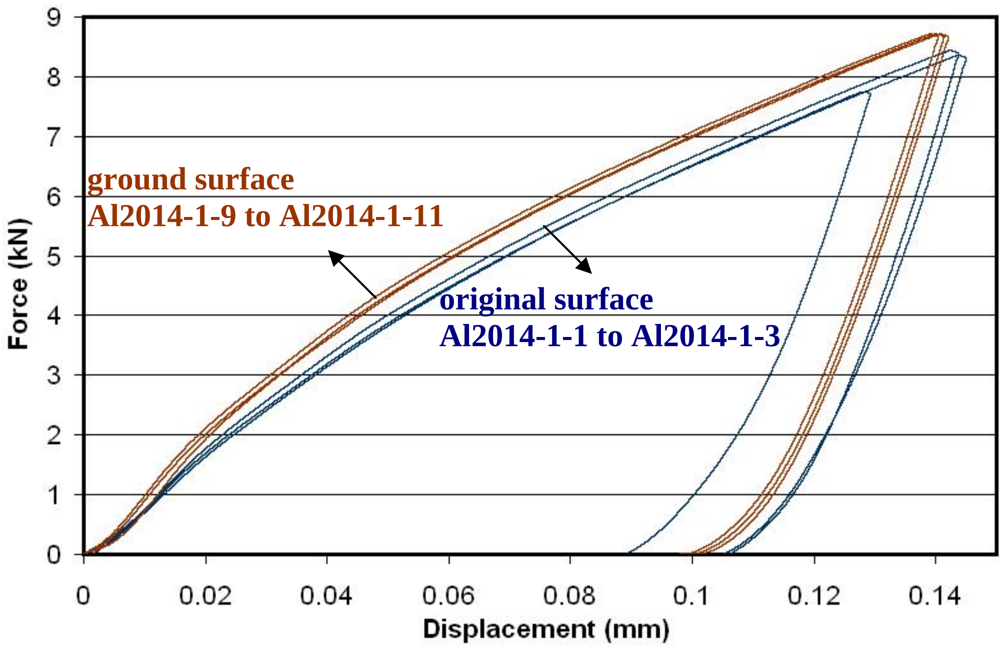


**Figure 6.19** Force-displacement curves for original and ground surfaces

There can be two explanations for this case. First explanation is that because of grinding, a layer close to the surface experiences strain hardening and higher yield stresses cause higher forces. Another reason may be the thickness of the specimens. Because after grinding, as seen in Table D.1 in Appendix D, ground specimens have thicknesses less than the original ones. Consider in the elastic zone the stress-strain relationship:

$$\sigma = E \cdot \varepsilon \tag{6.3}$$

If in Eqn. (6.3) $\sigma$ is replaced by $\sigma = \dfrac{F}{A_o}$ and $\varepsilon$ is replaced by $\varepsilon = \dfrac{\Delta t}{t_o}$, then force is obtained as follows:

$$F = A_o \cdot E \cdot \frac{\Delta t}{t_o} \tag{6.4}$$

According to Eqn. (6.4), force decreases if $t_o$ increases. This is an acceptable reason for the difference between forces.

### 6.4.3.2 Triple Indentations

In one set of experiments, one specimen is used to determine three force-displacement curves. With three different specimens, nine experiments have been performed. The idea was to reduce the effort and time to replace the specimen with a new one in addition to decrease number of specimens used.

The first two indentations were applied at the sides whereas the third was applied in the middle. This order was selected to have equal distances between the imprints. First the specimen is placed to the limit where the other edge remains still under the reference table, then second indentation is done on the other side where same precaution is taken for the previous edge. Finally, the specimen is placed such that the third imprint is in the middle of the previous two.

Figure 6.20 shows an indented specimen with triple indentations.

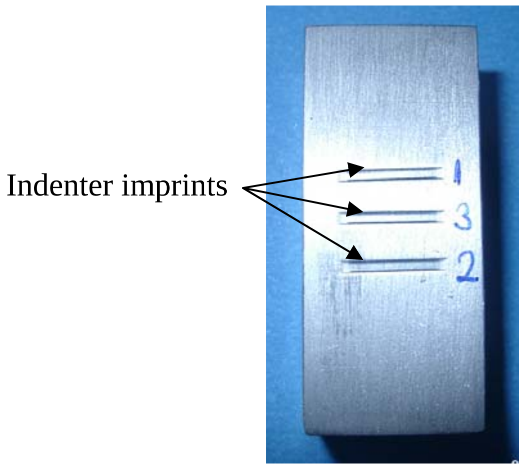


**Figure 6.20** Order and placements of indentations on one specimen (Al2014-1-6)

The results were quite unexpected. These experiment results for the indentation applied in the middle of the other two revealed force-displacement curves different from what is expected. For each three specimens the force-displacement curves for the third indentation was above those of other two. The force-displacement curves are as seen in Figure 6.21.

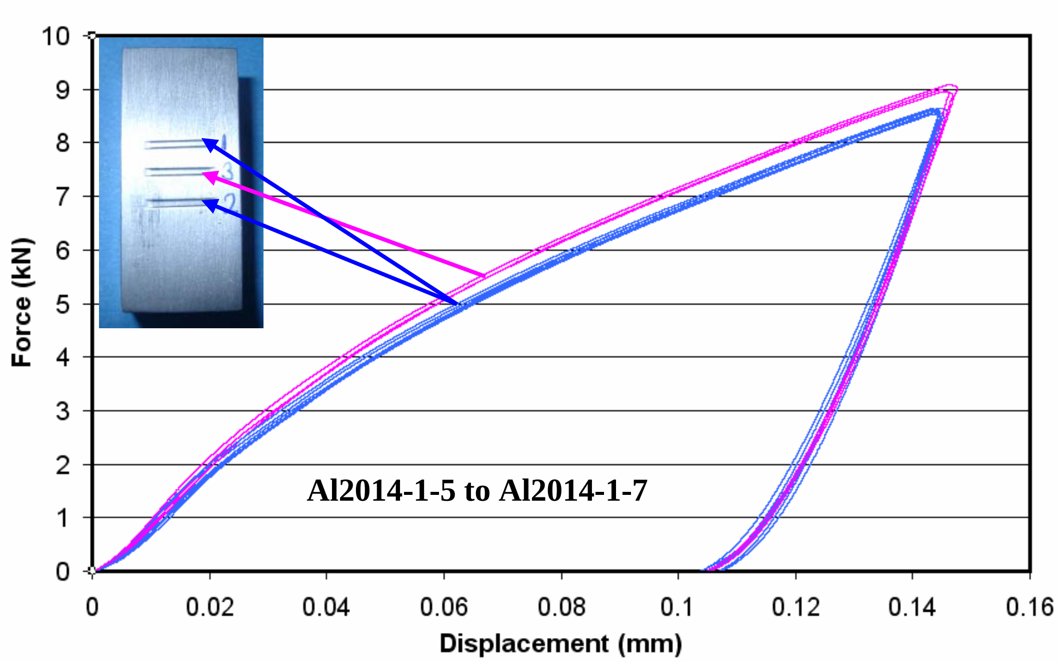


**Figure 6.21** Force-displacement curves of triple-indentations by experiments

The reason for rise of forces is analyzed by finite element method where details and results are given in Chapter 3 of this thesis. Higher forces for the third indentation are explained by the residual stresses which remain close to the surface in the middle after the first two indentations.

### 6.4.3.3 Effect of Clamping

The effect of clamping the specimens during indentation needed to be investigated in order to decide under which circumstances better results are obtained. The experiments for higher clamping forces have shown that clamping the indentation specimen tightly increases the repeatability of the tests. So, it is seen that clamping is advantageous to have higher repeatability of tests. Figure 6.22 shows how higher clamping forces increase repeatability.

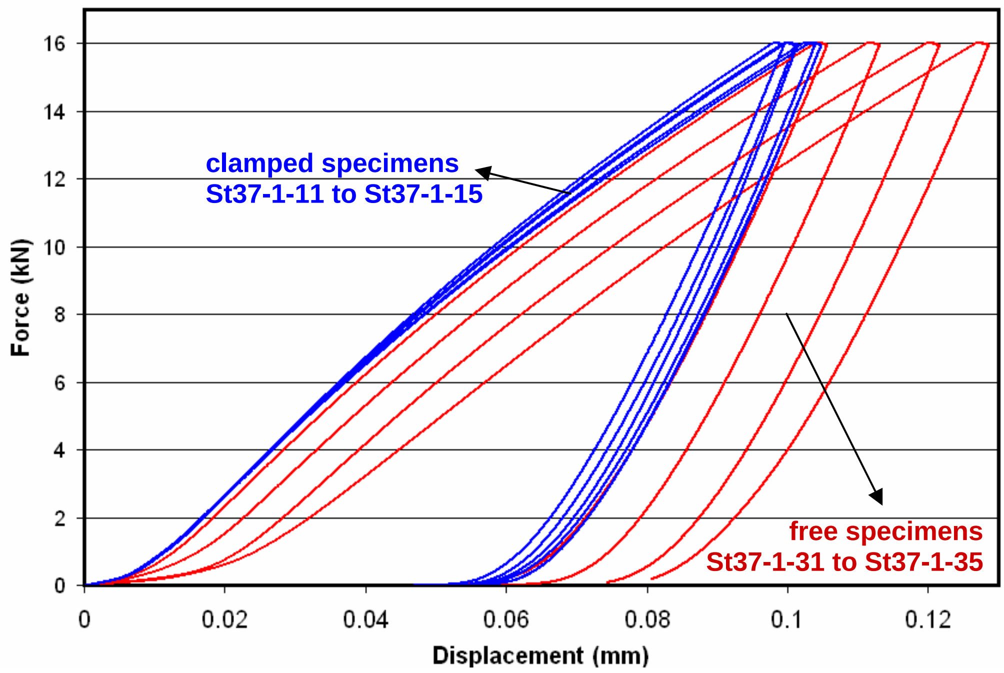


**Figure 6.22** Effect of clamping force on force-displacement curves (Circular base indenter with $R$ = 2 mm)

The experiments in Figure 6.22 are done by the circular cross-sectional indenter. Detailed explanations of these experiments can be found in [42, Chapter 5].

Clamping hinders the motion of specimens on the anvil surface. So, when the specimens are clamped indentation is repeated with the same boundary conditions each time. The possibility that the clamping force might affect the force-displacement curves is analyzed in Chapter 3 of this study.

### 6.4.3.4 Effect of Indenter Geometry

Indentation tests are done using two types of indenters given in Figure 6.5. Figure 6.23 shows the comparison of force-displacement curves obtained by experiments on Al 5086 specimens in transverse to rolling direction. Maximum load termination criteria up to 10 kN is applied.

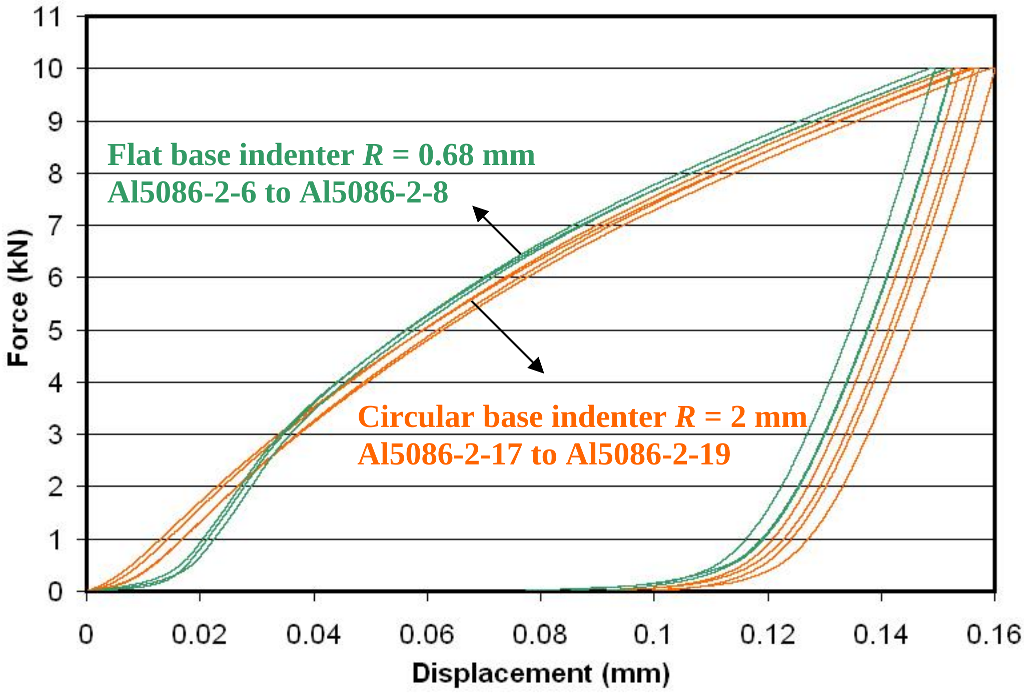


**Figure 6.23** Effect of indenter geometry on force-displacement curves

The figure shows that after 3 kN of force, flat base indenter needs higher forces to penetrate into the material. This is a reasonable result when also the finite element results of comparison of different radii given in Chapter 3 are considered. An indenter with a whole radius at the base part starts with smaller contact area so forces are smaller.

The non-linear behavior at the beginning of the curve can be explained by tilting of the indenter in the transverse direction. Tilting in transverse direction has no effect for the circular base indenter but it should be considered for the flat base indenter. In addition, since the parallelities of the two indenters are adjusted one after another, this may cause even some small angular difference between the flat base indenter and the indenter with circular base.

### 6.4.3.5 Effect of Anisotropy

In order to analyze the effect of anisotropy on indentation force-displacement curves, two groups of specimens, in rolling direction and in transverse to rolling direction are used. An indentation in rolling direction means that the longitudinal direction of the indenter is parallel to the rolling direction whereas an indentation transverse to rolling direction means the longitudinal direction of the indenter is perpendicular to the rolling direction.

Figure 6.24 shows indentation results in two directions. As observed, the force-displacement curves of indentations in rolling and transverse to rolling direction are very close to each other. The scatter bands overlap and difference between the force-displacement curves cannot be observed.

On the other hand, under same loading conditions and same preparation method of specimens, anisotropy of the material is observed by the circular base indenter. Those results can be seen in [42, Chapter 5].

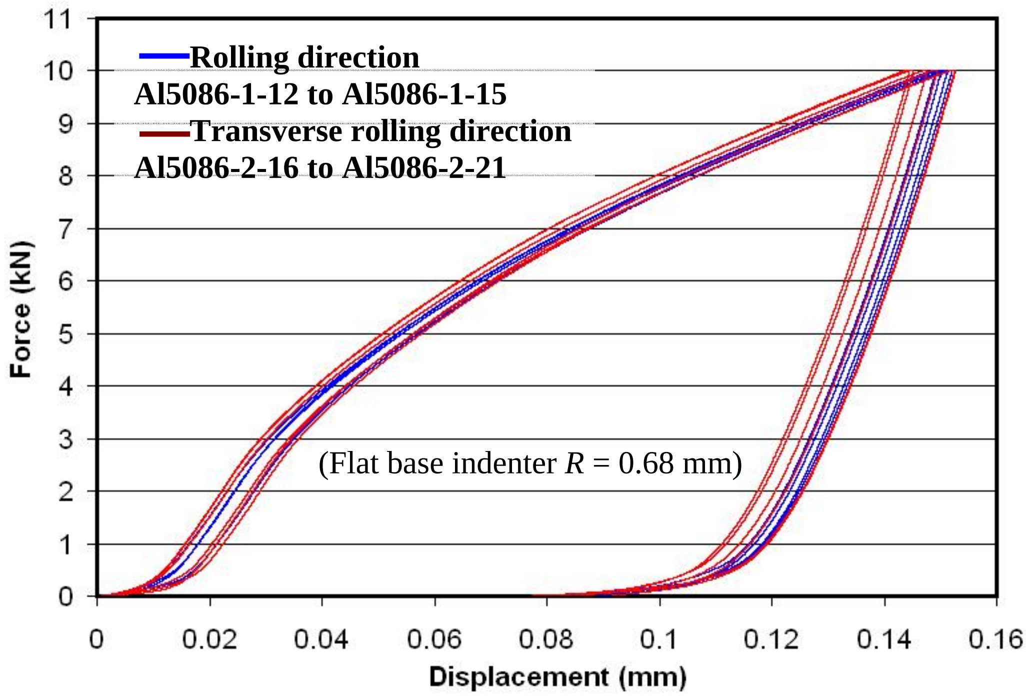


**Figure 6.24** Effect of rolling direction on force-displacement curves

# CHAPTER 7

# DISCUSSION AND CONCLUSIONS

The aim of this study is to investigate the method of determination of anisotropy by indentation tests. Force-displacement data obtained by finite element computations and by indentation experiments are to be used. A joint-study uses these data in an optimization function to determine the anisotropy parameters of Hill 1948 anisotropic yield criterion.

In order to reach the goal, finite element method is used to model and simulate the process and real indentation tests are done. In addition, an analytical method is used to predict force-displacement data.

In Chapter 3, finite element method analyses of indentation are given. The analyses have started with a plane strain model. First, the effect of element size and mesh topology on force-displacement data of indentation by finite element method is investigated and an optimum mesh topology is reached. Further two-dimensional plane strain analyses used this mesh. The effect of change of relative force tolerance parameter is investigated and a value is determined as supplying the smoothest curve with convergence. Later, the process parameters are investigated. These are the effect of radius of the indenter, effect of coefficient of friction at the contact surfaces and the effect of material. It was also required to check the effect of relative sliding velocity parameter to prove that the friction analyses give correct results.

These analyses helped to determine the indenter geometry. An indenter with $R / c = 1/3$ is chosen to be used in experiments. The analyses have also revealed that the coefficient of Coulomb friction has negligible effect on force-displacement curves.

The tilting of indenter is analyzed by a plane strain model for transverse tilting and by a three-dimensional model for longitudinal tilting. It is shown that tilting of indenter longitudinally has greater effect on force-displacement data than tilting in transverse direction. 2˚ tilting angle in transverse direction causes on the average 10% error in the plastic zone whereas 0.2˚ tilting angle in longitudinal direction is enough for the same amount of deviation of force-displacement data. In addition, tilting of indenter affects the elastic zone of the force-displacement curves such that the curvatures change. This study has shown that serious precautions have to be taken during tests to avoid non-parallelity of the surfaces.

Chapter 3 includes also analysis of multiple indentations on one specimen. This was necessary to analyze the results of a group of tests. The analyses have proven that if three indentations on one specimen of surface 20 mm x 45 mm is done with spacing of three indenters, the force-displacement curve of the indentation applied in the middle and after the first two on the sides is higher than the previous two curves. Two possible reasons strain-hardening and residual stress effect are investigated and the conclusion is that the primary reason is the residual stress state in the middle. The plastic-strain zones of the first two indentations on the two sides cannot reach the third indentation zone. For a specimen of this surface area it is shown that spacing of 7 times the indenter thickness is still not enough to reach the force-displacement curves of the first two indentations.

Chapter 4 of this thesis deals with finite element method analyses of compression tests. First, a cylindrical and prismatic specimen is compared to compare the flow curve data obtained by compression of these two. Cylindrical specimen is modeled as axisymmetric whereas prismatic specimen is modeled in three-dimensions. It is deduced that under ideal conditions there is no difference between the results. Later, using the three-dimensional model of prismatic specimen, friction and tilting analyses are done as well as analyses of changing height of the specimen. It is shown that increasing friction coefficient increases forces and when friction coefficients are not equal for upper and lower dies, the bulge leaves the center and approaches the surface with higher friction coefficient.

In Chapter 5, the upper bound method solution is used. In this solution, indentation is assumed to be frictionless and material is assumed to be rigid-plastic. The radius of the indenter is approximated by a line. Two different velocity fields are introduced. Then, the force-displacement data obtained by upper bound method analysis is compared with the finite element results and it is seen that around 0.1 mm displacement errors are 15 % and 20 %. The basic effects in the results are the velocity field and the representation of the radius.

Chapter 6 presents the experimental results. First of all, compression and tension test results are presented. For the material used in this study, tension tests are used to investigate the anisotropy of the material and it is shown that the material used for detection of anisotropy by indentation is really anisotropic.

Then, various effects on indentation force-displacement curves are investigated experimentally. The effect of surface quality tests have shown that specimens with ground surface have higher force values for the same displacement when compared with the original surface. The triple-indentation experiments reveal that when the last indentation is applied in the middle of the previous two indentations, the forces are higher for the third indentation. The reason of this fact is investigated by finite element analysis and shown to be the residual stresses in Chapter 3.

During experiments, the effect of clamping the specimen is also tested. It is seen that, clamping the specimens tightly increases the repeatability of the tests. The indenter geometry effect is also given by a graph where the force-displacement curves obtained by two indenters with a flat base and a circular base are compared. It is observed that the forces are higher for the flat base indenter after 0.035 mm of displacement. Before that displacement, because of curvature at the beginning, forces are lower for flat base indenter.

Finally, the effect of anisotropy is investigated by indentation with the flat base indenter. Specimens are prepared in parallel and transverse to rolling direction. Although the material's anisotropy is proven by the tension tests, effect of anisotropy is not observed by indentation with the flat base indenter. This shows that with this type of indenter anisotropic properties of the test material cannot be determined.

# REFERENCES

[1] E. N. Kaufmann, Characterization of Materials, Volume 1, Wiley-Interscience (2003), 316-323.

[2] W.D. Callister, Materials science and engineering an introduction, fifth Edition, John Wiley & Sons (2000), 136.

[3] K. Pöhlandt, T. Oberländer, Concepts for the description of plastic anisotropy in cold bulk metal forming, Journal of Materials Processing Technology 34 (1992), 187-194.

[4] D.Banabic, H. J. Bunge, K. Pöhlandt, A. E. Tekkaya, Formability of metallic materials, Springer (2000), 122-169.

[5] W. F. Hosford, R. M. Caddell, Metal Forming mechanics and metallurgy, Prentice-Hall (1983), 263-270.

[6] D. Banabic, K. Pöhlandt, Yield criteria for anisotropic sheet metal, UTF Science 2 (2001), 19-27.

[7] R. V. Von Mises, Mechanics of plastic deformation of crystals (in German), Z. Ang. Math. Mech. 8 (1928), 161-185.

[8] W. Olszak, W. Urbanowski, The orthotropy and the nonhomogeneity in the theory of plasticity, Pol. Arch. Mech. Stos. 8 (1956), 85-110.

[9] M. Lindner, Analyse des Einflusses der plastischen Orthotropie nach Hill auf die Kraft-Verschiebungs-Kurven beinm Stauchen, Diplomarbeit (2002), 12-14.

[10] J. Woodtrope, R. Pearce, The anomalous behavior of aluminum sheet under balanced biaxial tension, Int. J. Mech. Sci., 12 (1970), 341-347.

[11] R. Pearce, Some aspects of anisotropic plasticity in sheet metals, Int. J. Mech. Sci. 10 (1968), 995-1001.

[12] E. Chu, Generalization of Hill's 1979 anisotropic yield criteria, J. of Mat. Processing Tech. 50 (1995), 207-215.

[13] C. Vial-Edwards, Yield loci of fcc and bcc sheet metals, Int. J. of Plasticity, Vol. 13, No. 5 (1997), 521-531.

[14] W.F. Hosford, Comments on anisotropic yield criteria, Int. J. Mech. Sci.,Vol. 27, No. 7/8 (1985), 423-427.

[15] F. Barlat, O. Richmond, Prediction of tricomponent plane stress yield surfaces and associated flow and failure behavior of strongly textured fcc polycrystalline sheets, Materials Science and Engineering 91 (1987), 15-29.

[16] F. Barlat, J. Lian, Plastic behavior and stretchability of sheet metals (Part I): A yield function for orthotropic sheet under plane stress conditions, Int. J. Plasticity 5 ( 1989), 51-56.

[17] R. Hill, A user-friendly theory of orthotropic plasticity in sheet metals, Int. J. Mech. Sci.,Vol. 35, No. 1 (1993), 19-25.

[18] F. Barlat et al. , Yielding description for solution strengthened aluminium alloys, Int. J. Plasticity 13 (1997), 185-201.

[19] W. Hu, Characterized behaviors and corresponding yield criterion of anisotropic sheet metals, Materials Science and Engineering A00 (2002), 1-6.

[20] S.A. Meguid, I.F. Collins, W. Johnson, The co-indentation of a layer by two flat plane or spherical headed rigid punches, Int. J. Mech. Sci. 19 (1977) 1-9.

[21] Meguid, S.A.; Klair, M.S., Elasto-plastic co-indentation analysis of a bounded solid using finite element method, Int. J. Mech. Sci. 27 (3) (1985) 157-168.

[22] S.A. Meguid, G. Shagal, J.C. Stranart, J. Daly, Three-dimensional dynamic finite element analysis of shot-peening induced residual stresses, Finite Elements in Analysis and Design 31 (1999) 179-191.

[23] R.F. Bishop, R. Hill, N.F. Mott, The theory of indentation and hardness tests, Proc. Phys. Soc. 57, Part 3 (1945), 147-159.

[24] R. Hill, E.H. Lee, S.J. Tupper, The theory of indentation of ductile materials, Proc. Roy. Soc. A, 188 (1947), 273-289.

[25] D. Tabor, A Simple Theory of Static and Dynamic Hardness, Proc. Roy. Society Series A, 192 (1948), 247-274.

[26] J. Grunzweig, I.M. Longman, N.J. Petch, Calculations and measurements on wedge-indentation, J. Mech. Phys. Solids, 2 (1954), 81-88.

[27] F.J. Lockett, Indentation of a rigid-plastic material by a conical indenter, J. Mech. Phys. Solids, 11 (1963), 345-355.

[28] K.L. Johnson, The correlation of indentation experiments, J. Mech. Phys. Solids, 18 (1970), 115-126.

[29] N. Bay, T. Wanheim, Axisymmetric upper bound theory applied to indentation of cones, Int. J. Prod. Res., 12 (2) (1974), 195-208.

[30] E. Dannenmann, E. Steck, H. Wilhelm, Über den Zusammenhang zwischen Eindringhärte und Umformgrad bei Kaltumformvorgängen, Bänder Bleche Rohre, 9 (7) (1968), 368-394.

[31] H. Wilhelm, Untersuchungen über den Zusammenhang zwischen Vickershärte und Vergleichsformänderung bei Kaltumformvorgängen, Girardet, Essen (1969).

[32] J.A.H. Ramaekers, Härte und Verformung metallischer Werkstoffe, Dr-Ing. Dissertation, Technical University Eindhoven, Einghoven (1970).

[33] A.E. Tekkaya, Improved relationship between Vickers hardness and yield stress for cold formed materials, Steel Research 72, No. 8 (2001), 304-310.

[34] M. Dao, N. Chollacoop, K. J. Van Vliet, T. A. Venkatesh and S. Suresh, Computational modeling of the forward and reverse problems in instrumented sharp indentation, Acta Mater. 49 (2001), 3899-3918.

[35] J. L. Bucaille, S. Stauss, E. Felder, J. Michler, Determination of plastic properties of metals by instrumented indentation using different sharp indenters, Acta Mater. 51 (2003), 1663-1678.

[36] M.T. Attaf, Connection between the loading curve models in elastoplastic indentation, Materials Letters 58 (2004), 3491-3498.

[37] T. Nakamura, T. Wang, S. Sampath, Determination of properties of graded materials by inverse analysis and instrumented indentation, Acta Mater. 48 (2000), 4293-4306.

[38] Y. Gu, T. Nakamura, L. Prchlik, S. Sampath, J. Wallace, Micro-indentation and inverse analysis to characterize elastic-plastic graded materials, Materials Science and Engineering A345 (2003), 223-233.

[39] G. Bolzon, G. Maier, M. Panico, Material model calibration by indentation, imprint mapping and inverse analysis, Int. J. of Solids and Structures 41 (2004), 2957-2975.

[40] H. Cho, G. Ngaile, Simultaneous determination of flow stress and interface friction by finite element based inverse analysis technique.

[41] T.W. Capehart, Y-T. Cheng, Determining constitutive models from conical indentation: sensitivity analysis, J. Mater. Res., Vol. 18, No. 4 (2003), 827-832.

[42] (42,43) E. Koray, Numerical and experimental analysis of indentation, MS Thesis, METU, Ankara (2005).

[43] G. E. Dieter, Mechanical Metallurgy, McGraw-Hill (1988), pp. 409-401,557-559.

[44] A.E. Tekkaya, Ermittlung von Eigenspannungen in der Kaltmassivumformung, Springer-Verlag (1986).

[45] A.E. Tekkaya, Lecture Notes of Metal Forming Technology, Middle East Technical University, Ankara (2001).

[46] J.E. Shigley, C.R. Mischke, Mechanical Engineering Design, Fifth Edition, McGraw Hill (1989), 331.

[47] A.E. Tekkaya, Lecture notes of ME 581, Chapter VI-part IV, Middle East Technical University, Ankara (2001).

[48] MSC. SuperForm Command Reference, Version 2002.

[49] J.E. Shigley, C.R. Mischke, Mechanical Engineering Design, Fifth Edition, McGraw Hill (1989), 729.

[50] A.E. Tekkaya, Lecture notes of ME 453, Chapter VI, Middle East Technical University, Ankara (2001), 01.131.

[51] aluMATTER. (Copyright 2001-2004). Retrieved December 19, 2004 from the World Wide Web: http://aluminium.matter.org.uk

[52] MatWeb. (Copyright 1996-2005). Retrieved December 20, 2004 from the World Wide Web: http://www.matweb.com

# APPENDIX A

# MODELING FRICTION
# IN FINITE ELEMENT METHOD

The most common two methods to express frictional stress are the Coulomb law and the shear law. According to Coulomb law, which is used in the finite element analyses throughout this thesis, the frictional stress is expressed as in Eqn. (A.1) [47].

$$d\vec{f}_{Friction} = -\mu \cdot \sigma_{normal} \cdot dA \cdot \frac{\Delta\vec{v}}{|\Delta\vec{v}|} \tag{A.1}$$

where $0 \leq \mu \leq 0.577$.

For a given normal stress, the friction stress has a step function behavior based upon the value of $\Delta\vec{v}$, the relative sliding velocity, as given in Figure A.1.

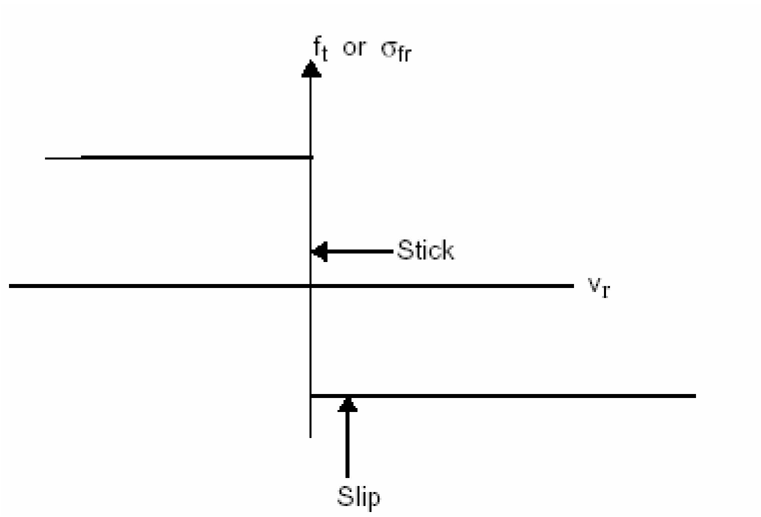


**Figure A.1** Coulomb friction model [48]

During contact, frictional stresses may result in instabilities because of change in direction of frictional forces around neutral lines. On one side of the neutral line material flows in one direction and on the other side material flows in the opposite direction. In order to improve stability, the frictional stress term given by Eqn. (A.1) is improved as in Eqn. (A.2).

$$d\vec{f}_{Friction} = -\mu \cdot \sigma_{normal} \cdot dA \cdot \frac{2}{\pi} \cdot \arctan(\frac{|\Delta\vec{v}|}{C}) \cdot \frac{\Delta\vec{v}}{|\Delta\vec{v}|} \tag{A.2}$$

Physically, the value of C is the value of relative sliding velocity when sliding occurs. The modification in Eqn. (A.2) makes it easier to handle the problem numerically by removing the instability.

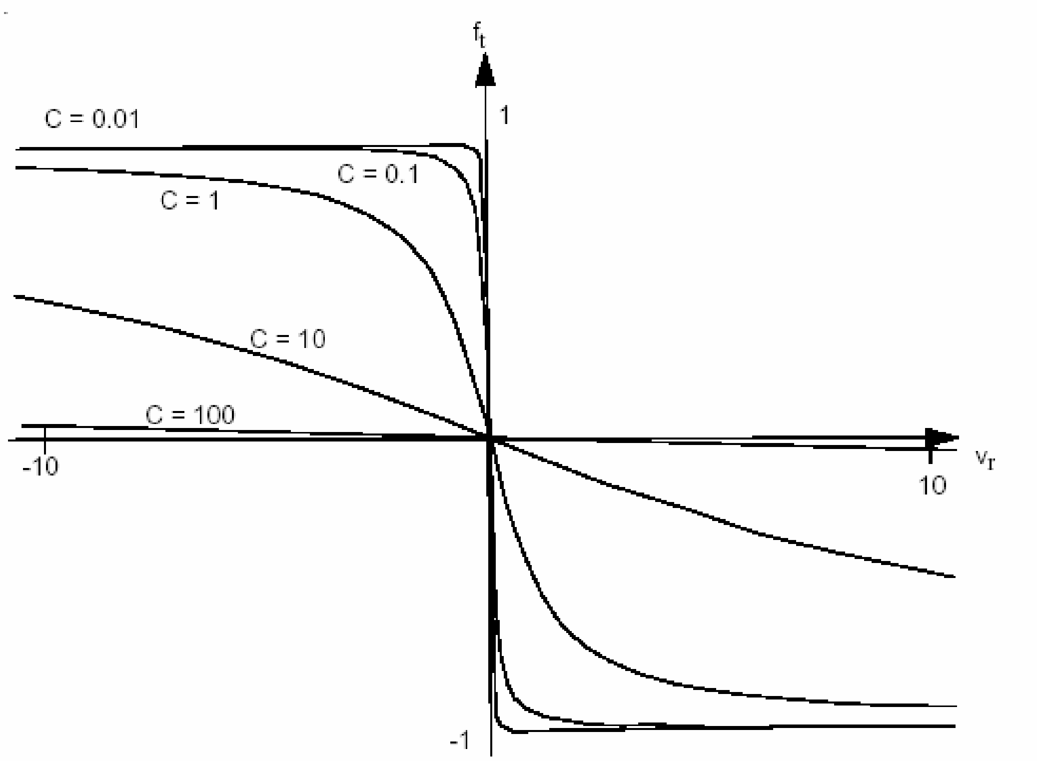


**Figure A.2** Effect of change of C [48]

With this fact in hand, it was a question during friction analyses that if the default value used for this parameter was close enough to the real case. For cases where the $\Delta\vec{v}$ value is very small, the effect of C is more. In order to identify how close the analysis results to the real case different parameters are to be tried.

The commercial finite element program MSC.SuperForm takes this parameter C as follows [48] when not input by the user.

$$C = \begin{cases} 0.01 \cdot |\Delta\vec{v}| & \mathit{for}\ |\Delta\vec{v}| \geq 0.01 \\ 0.0001 & \mathit{for}\ |\Delta\vec{v}| < 0.01 \end{cases} \tag{A.3}$$

where $|\Delta\vec{v}|$ is the calculated local relative sliding velocity.

# APPENDIX B

# MATERIAL PROPERTIES USED IN FINITE ELEMENT ANALYSES

Three types of material CuZn30, AlMgSi1 and C15 are used in the finite element analyses. Only material properties of C15 are read from the material database of MSC.SuperForm, and for CuZn30 and AlMgSi1 material flow data, Young's modulus and Poisson's ratio are assigned. Table B.1 shows elastic properties of brass and aluminum alloy taken from [49].

**Table B.1** Elastic material properties for CuZn30 and AlMgSi1 [49]

| Material | Young's modulus (GPa) | Poisson's ratio |
|---|---|---|
| CuZn30 | 106 | 0.324 |
| AlMgSi1 | 80 | 0.334 |

Flow curves are assigned in MSC.SuperForm in piecewise linear format using tables. The plastic flow curves are obtained from Ludwik's expression $\sigma_f = C \cdot \varepsilon^n$ the material constants of which are taken from [50] are seen in Table B.2. In this formulation, *C* is named as the strength constant and *n* is the strain hardening exponent.

**Table B.2** Cold flow curves for CuZn30 and AlMgSi1

| Material | $\sigma_{fo}$ (MPa) | *C*(MPa) | *n* |
|---|---|---|---|
| CuZn30 | 250 | 880 | 0.433 |
| AlMgSi1 | 130 | 260 | 0.197 |

For all three materials, the flow curves are given in Figure B.1.

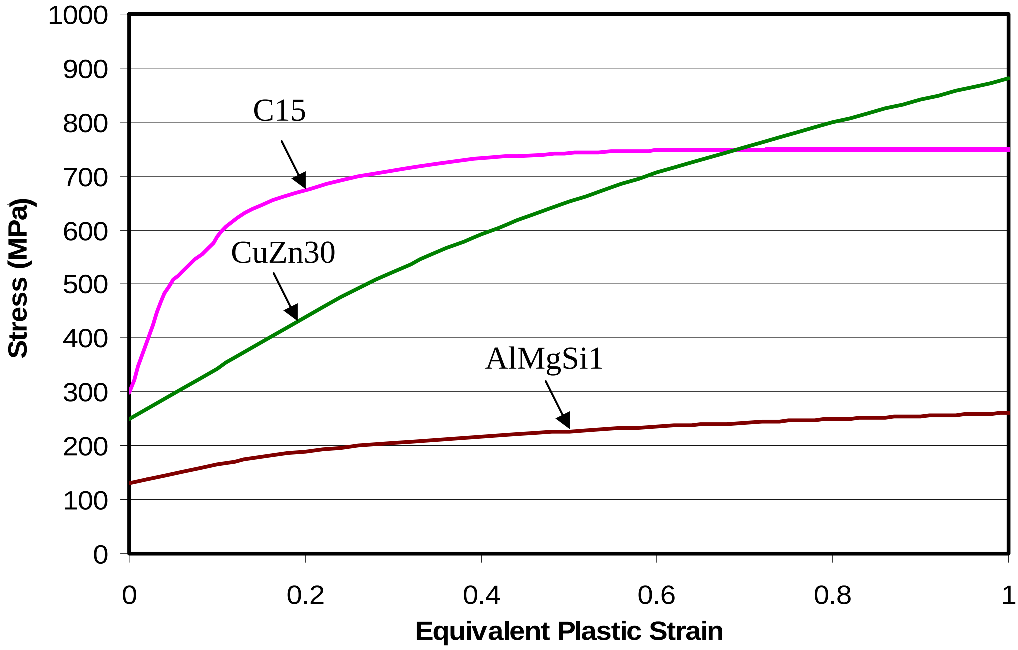


**Figure B.1** Cold flow curves of materials used in finite element analyses

# APPENDIX C

## FEM MESH TOPOLOGIES USED FOR MULTIPLE INDENTATION ANALYSES

This chapter includes mesh topologies used for multiple indentation analyses modeled symmetrically with several values of distances between indentations.

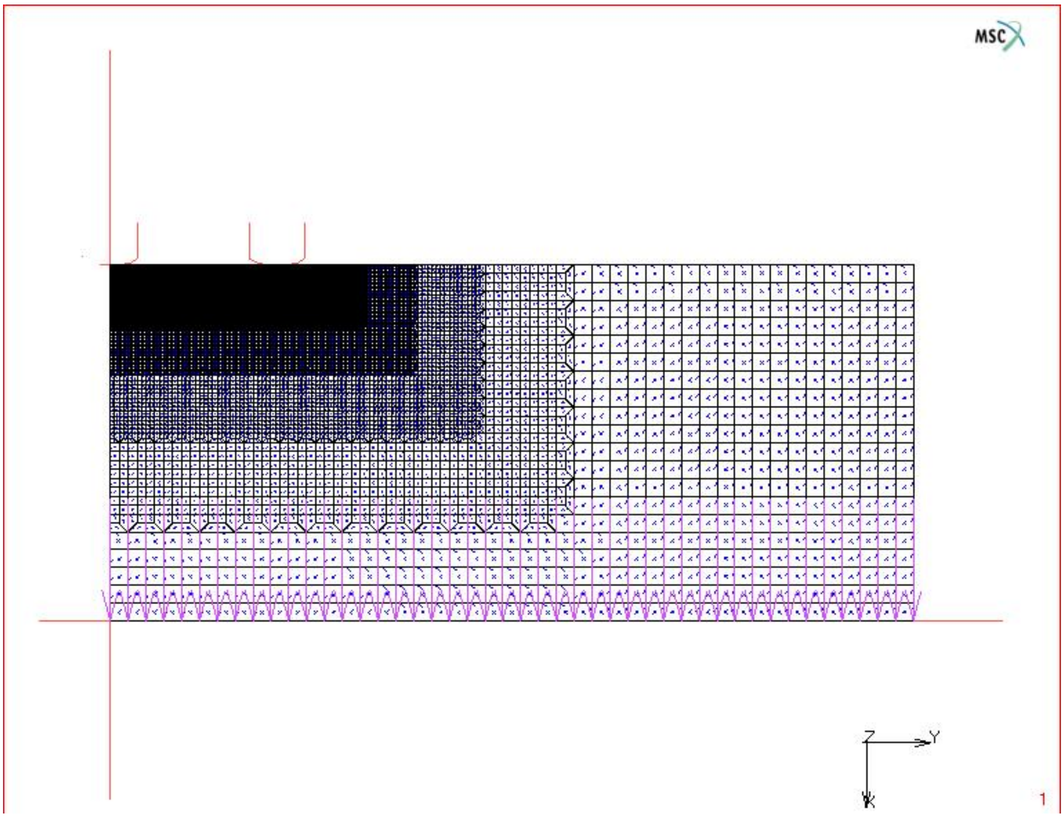


**Figure C.1** Mesh topology for $d/c$ = 2, 19425 elements

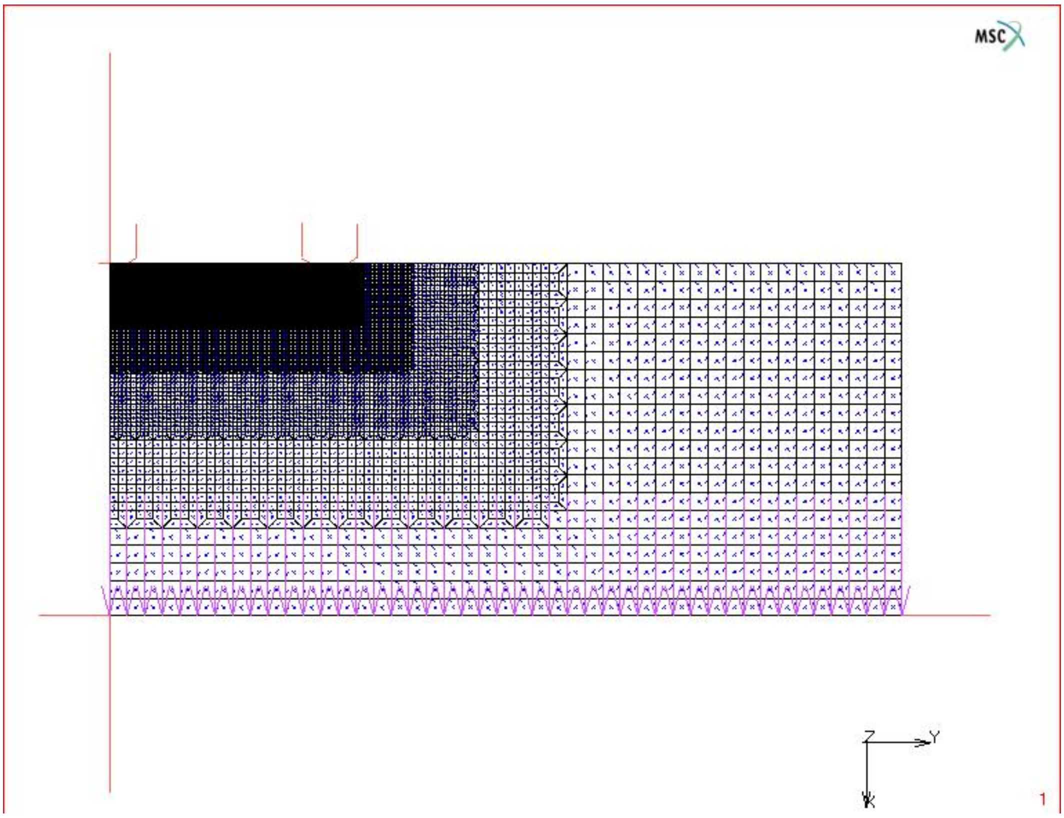

**Figure C.2** Mesh topology for $d/c$ = 3, 19425 elements

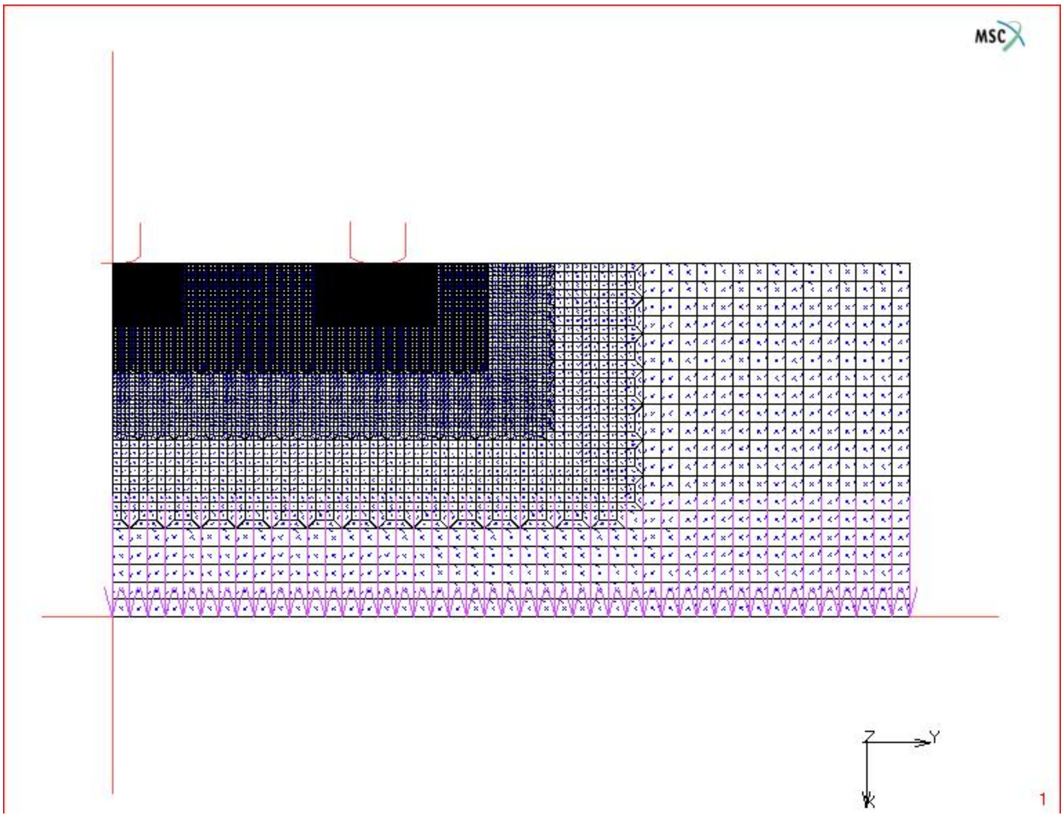

**Figure C.3** Mesh topology for $d/c$ = 4, 18793 elements

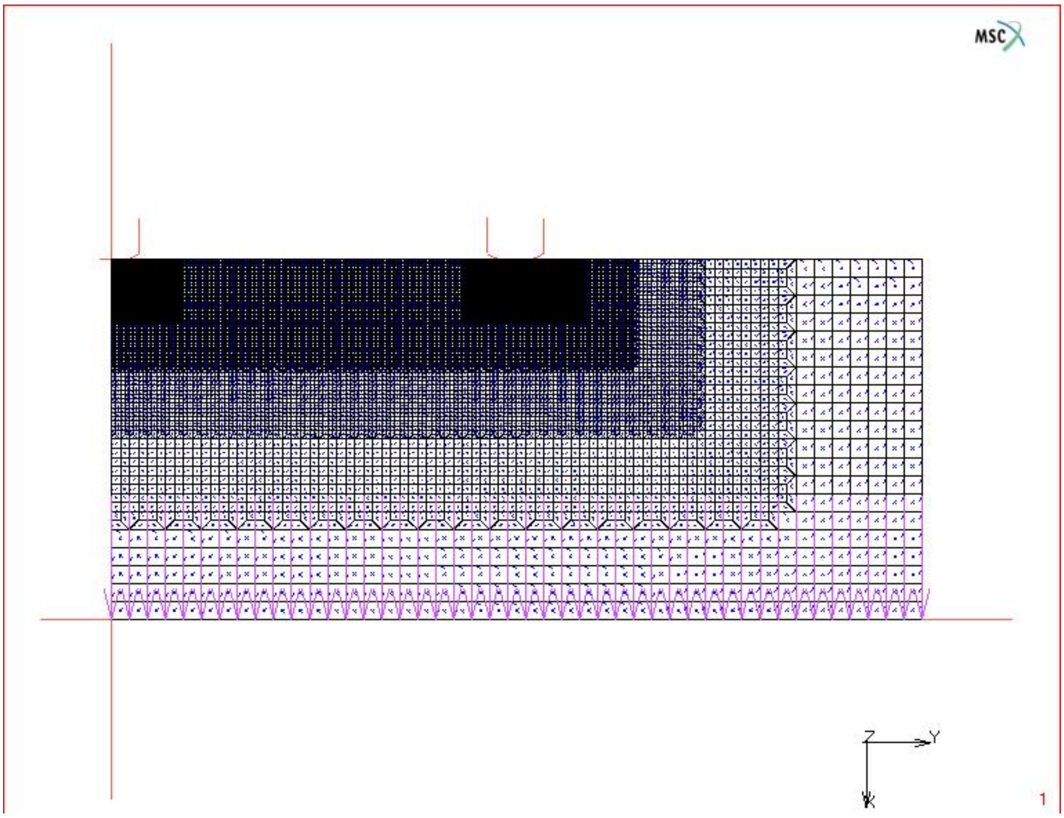


**Figure C.4** Mesh topology for $d/c$ = 6, 22457 elements

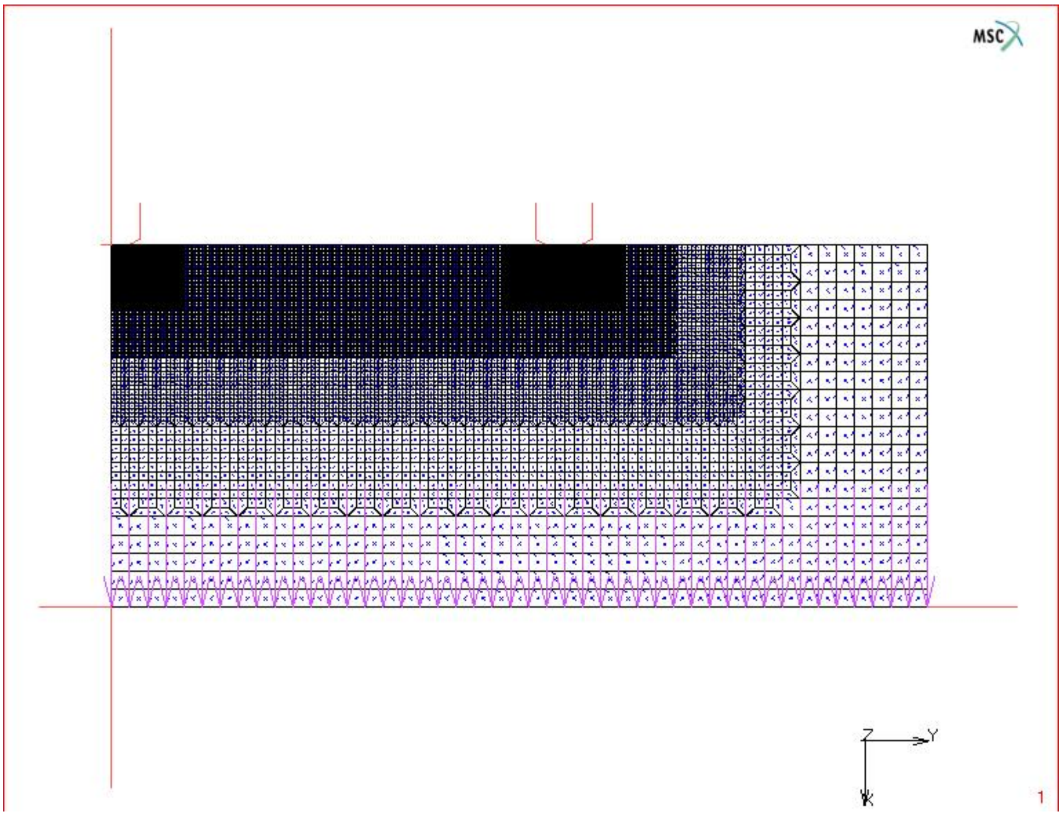


**Figure C.5** Mesh topology for $d/c$ = 7, 23285 elements

# APPENDIX D

# INDENTATION SPECIMEN PROPERTIES

In this chapter, it is aimed to identify the specimen properties in tabulated form. In Chapter 6 the experimental results have been given. During experimental studies three types of material have been used. The specimen label given in the first column in Table D.1 includes the material name. The number written after the material is to indicate in which direction with respect to rolling the indentation is done. “1” is used for indentation in rolling direction, “2” is used for indentation in transverse to rolling direction. The last number in the label is the specimen number.

The second column gives surface property of the specimen. The specimen surfaces are either in the form bought from the supplier which is called original in the table or ground.

The third column gives information about the direction of indentation, “RD” means longitudinal axis of indenter is in the same direction with rolling and “TRD” means longitudinal axis of indenter is perpendicular to direction of rolling.

Finally the width, length and thickness of the specimens are given in millimeters.

**Table D.1** Indentation specimen properties

| Specimen Label | Surface property | Direction | *w* (mm) | *h* (mm) | *l* (mm) |
|---|---|---|---|---|---|
| St37-1-11 | ground | RD | 20.52 | 18.04 | 45.02 |
| St37-1-12 | ground | RD | 20.32 | 18.04 | 45.02 |
| St37-1-13 | ground | RD | 20.58 | 18.04 | 45.02 |
| St37-1-14 | ground | RD | 20.54 | 18.04 | 45.00 |
| St37-1-15 | ground | RD | 20.50 | 18.04 | 45.08 |
| St37-1-31 | ground | RD | 20.50 | 18.04 | 45.08 |
| St37-1-32 | ground | RD | 20.52 | 18.05 | 45.02 |
| St37-1-33 | ground | RD | 20.58 | 18.03 | 45.06 |
| St37-1-34 | ground | RD | 20.54 | 18.04 | 45.04 |
| St37-1-35 | ground | RD | 20.53 | 18.06 | 45.03 |
| Al2014-1-1 | original | RD | 20.44 | 16.10 | 45.08 |
| Al2014-1-2 | original | RD | 20.68 | 16.10 | 45.14 |
| Al2014-1-3 | original | RD | 20.32 | 16.10 | 45.56 |
| Al2014-1-9 | ground | RD | 19.52 | 15.98 | 44.82 |
| Al2014-1-10 | ground | RD | 20.32 | 15.68 | 44.64 |
| Al2014-1-11 | ground | RD | 19.12 | 15.94 | 44.78 |
| Al5086-2-6 | original | TRD | 19.61 | 3.22 | 45.40 |
| Al5086-2-7 | original | TRD | 20.10 | 3.20 | 45.20 |
| Al5086-2-8 | original | TRD | 20.10 | 3.24 | 46.00 |
| Al5086-1-11 | original | RD | 19.46 | 3.22 | 45.94 |
| Al5086-1-12 | original | RD | 19.62 | 3.22 | 45.48 |
| Al5086-1-13 | original | RD | 20.10 | 3.22 | 45.34 |
| Al5086-1-14 | original | RD | 20.08 | 3.22 | 45.10 |
| Al5086-1-15 | original | RD | 20.12 | 3.22 | 45.34 |
| Al5086-2-16 | original | TRD | 20.14 | 3.22 | 45.18 |
| Al5086-2-17 | original | TRD | 20.00 | 3.22 | 45.36 |
| Al5086-2-18 | original | TRD | 20.22 | 3.22 | 45.38 |
| Al5086-2-19 | original | TRD | 20.72 | 3.22 | 45.14 |
| Al5086-2-20 | original | TRD | 21.28 | 3.22 | 44.86 |
| Al5086-2-21 | original | TRD | 19.98 | 3.22 | 44.92 |